輔仁學誌—理工類

中華民國九十四年十二月　　第三十九期

目　錄

頁次

一系列苯基酸 6-（4-烷苯基）尼古丁酯液晶化合物的合成及熱向性研究
....賈文隆　夏忠平　林宏洲 1

使用單一四端主動電流傳輸器合成電流式帶拒與全通濾波器 ....鄞永昌 11

PAPM: 一個新的擬真與非擬真混合成像演算法 ....王宗銘　李孟燦 23

指數韋伯串聯系統故障函數之估計 ....陳思勉　戴淯珍 47

應用預測－修正法則求解非線性微分方程式初始值問題
....蔡　龍　劉宏毅　簡光甫 63

電子槍蒸鍍製成的鈦鋁氧化物與鈦矽氧化物薄膜的表面型態與光學性質的研究
..............................林更青　楊忠如　吳坤東　姚永德 83

空時碼多載波分碼多工存取系統之研究 ....余金郎　林致群 93

創新密舖平面圖案系統之研究 ....呂克明 111

93 學年度理工學院專任教師對外發表之論文摘要 141

FU JEN STUDIES

SCIENCE AND ENGINEERING

NO. 39, dec. 2005

CONTENTS

Page

Synthesis and Thermotropic Studies of a Series of Phenyl 6-(4-Alkylphenyl) Nicotinates Liquid Crystalline Compounds .... *by Win-Long Chia, Chung-Ping Hsia and Hong-Cheu Lin* 1

Realization of Current-Mode Notch and All-pass Filters using Single CFCCII .... *by Yung-Chang Yin* 11

PAPM: A Novel Algorithm for Photorealistic and Non-Photorealistic Hybrid Rendering .... *by Chung-Ming Wang and Meng-Tan Lee* 23

Hazard Function Estimation for Series System with Exponentiated Weibull Components .... *by Sy-Mien Chen and Yu-Zen Dai* 47

A New Predictor-Corrector Method for Solving Initial-Value Problems of Nonlinear Ordinary Differential Equations . *by L. Tsai and H.Y. Liou and G. F. Jiang* 63

Morphological and Optical Properties of the TiO_2/Al_2O_3 and TiO_2/SiO_2 Films by Electron Beam Evaporation .... *by K.C. Lin and C.R. Yang and K.T. Wu and Y.D. Yao* 83

Studies on Multi-Carrier CDMA Systems with Space-Time Block Codes .... *by Jung-Lang Yu and Chih-Chan Lin* 93

A Study of Innovative Plane Tessellation Patterns Systems.................... *by Keh-Ming Lu* 111

Abstracts of Papers by Faculty Members of the College of Science and Engineering that Appeared in the 2004~2005 Academic Year.................................... 141

SYNTHESIS AND THERMOTROPIC STUDIES OF A SERIES OF PHENYL 6-(4-ALKYLPHENYL) NICOTINATES LIQUID CRYSTALLINE COMPOUNDS

WIN-LONG CHIA*, CHUNG-PING HSIA

Department of Chemistry, Fu Jen Catholic University, Taipei, Taiwan, Republic of China 242

HONG-CHEU LIN

Department of Material Science and Engineering, Chiao Tung University, Hsinchu, Taiwan, Republic of China 300

Abstract

We have synthesized a new series of pyridine-containing liquid crystalline compounds, phenyl 6-(4-alkylphenyl) nicotinates (**CnPNP**, n=4-8). The synthesis consists of the Grignard reaction on phenyl *N*-phenyloxycarbonylnicotinium chloride with an 4-alkylphenylmagnesium bromide and oxidizing the resulting 1,2-dihydropyridine intermediates by *o*-chloranil to afford the desired phenyl 6-(4-alkylphenyl)nicotinates. Excellent yields (66-93%) and high α-regioselectivity on the pyridine ring were observed in all cases. Thermotropic studies of this series of phenyl 6-(4-alkylphenyl)nicotinates were done by differential scanning calorimetry (DSC) and polarized microscopy. Smectic A phase was mainly the only mesophase in this series of compounds.

Key words: Pyridine-containing compounds, synthesis, thermal analysis.

---

*Corresponding author. Tel: +886-2-29053567; Fax:+886-2-29023209
E-mail:chem1008@mails.fju.edu.tw

1. Introduction

Interest in liquid crystal (LC) technology is increasing rapidly because it is a leading candidate for full colour, monochrome and black and white displays in computers, aircraft and other vehicle cockpits and for the large next-generation television market. Although some pyridine-containing liquid crystalline compounds have been synthesized before [1-4], there is a large demand for new liquid crystalline materials for more advanced displays. Recently, certain pyridine-containing liquid crystalline compounds have shown enhanced properties in display application [5].

Regioselective addition of an organometallic reagent to 1-acylpyridinium salts [6] has provided us a route to synthesize pyridine-containing liquid crystalline compounds in a convergent manner, in short steps and in excellent yield [7]. Previously, we have prepared various 2- or 4-substituted pyridines and alkaloids by this method [8]. Recently, we have successfully applied this methodology to prepare liquid crystalline 5-substituted 2-(4-alkylphenyl)pyridines [7]. In this paper, we report a facile and efficient synthesis (**Scheme 1**) of a series of liquid crystalline phenyl 6-(4-alkylphenyl)nicotinates 4 (**CnPNP**, n=4-8), their phase transitions and mesomorphism studies using DSC and polarized microscopy.

2. Experimental

2.1 Synthesis

Phenyl 6-(4-alkylphenyl)nicotinates (**CnPNP**, n=4-8) were synthesized using the Grignard reaction of 4-alkylphenylmagnesium bromide to react with phenyl *N*-phenyloxycarbonylnicotinium chloride. The resulting 1,2-dihydropyridine intermediates were oxidized with *o*-chloranil to afford the desired products (**Scheme** 1). A representative syntheses of compounds **CnPNP** (n=7) is described below.

For **3d**: To a solution of 1-bromo-4-heptylbenzene (10 mmol) in 20 ml THF was added freshly dried magnesium granules (11 mmol) under an inert atmosphere. The Grignard solution **1** was then slowly added by syringe into a preformed solution of nicotinium chloride **2** (10 mmol phenyl chloroformate, 10 mmol phenyl nicotinate, 20 ml dry THF at -20℃, 0.5 h) at

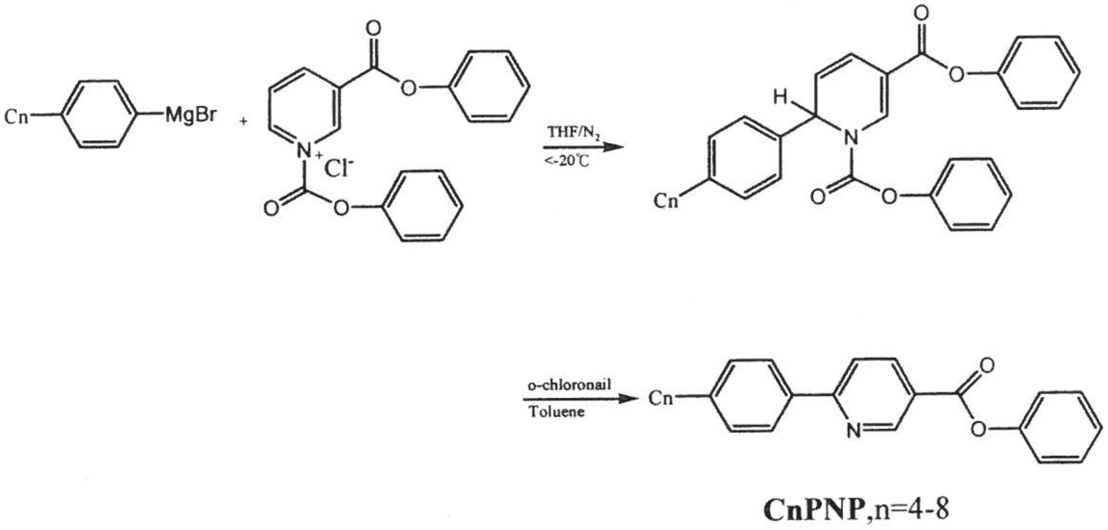

CnPNP,n=4-8

Scheme 1. Synthesis of phenyl 6-(4-alkylphenyl)nicotinates 4 (CnPNP, n = 4-8).

-20℃. The resulting solution was warmed slowly to room temperature and stirred for another 8 h. After evaporation of the THF, the residue was extracted with ether. The crude 3d was obtained by washing twice with 10% HCl solution and brine and by drying with magnesium sulfate. For **4d** (**CnPNP**, n=7): To a solution of 20 ml dry toluene and crude **3d** was added about 1.5eq. o-chloranil. The reaction mixture was heated to reflux for a number of hours under inert atmosphere and then quenched by adding 25 ml 1N NaOH solution and 25 ml ethyl ether and filtered through celite. Normal aqueous work up and isolation with column chromatography (SiO2, 1:1 methylene chloride: hexane) affords the product **4d** (85%). The analytically pure **4d** (**CnPNP**, n=7) white crystals were obtained after several re-crystallizations from methylene chloride : methanol (1:5): for example, for the **4d** (**CnPNP,** n=7), ^{1}H NMR (300MHz, $CDCl_3$): 9.43 (d, 1H, J=2.1 Hz), 8.47 (dd, 1H, J_1 = 8.1 Hz, J_2=2.1 Hz), 8.02 (d, 2H, J=8.4 Hz), 7.86 (d, 1H, J=8.4 Hz), 7.5-7.43 (m, 2H), 7.36-7.2 (m, 5H), 2.68 (t, 2H, J=8.1 Hz), 1.72-1.62 (m, 2H), 1.37-1.27 (m, 8H), 0.89 (t, 3H, J = 6.6 Hz). ^{13}C NMR (300MHz, $CDCl_3$): 164.168, 161.647, 151.540, 150.752, 145.624, 138.390, 135.649, 129.656, 129.162, 127.455, 126.213, 123.454, 121.726, 119.690, 35.889, 31.899, 31.402, 29.336, 29.255, 22.745, 14.175. FTIR (KBr): 2922, 1738, 1591, 1489, 1198, 775.

The other homologues of series **CnPNP**, n=4-8 were synthesized and their purities confirmed by methods similar to those above. All had satisfactory ^{1}H NMR, ^{13}C NMR and IR spectra.

Table 1. Synthesis of phenyl 6-(4-alkylphenyl)nicotinates 4a-4e (CnPNP, n = 4-8).

Entry	n	Yielda(%)
4a	4	89
4b	5	93
4c	6	69
4d	7	85
4e	8	66

[a]Isolated yield by column chromatography (methylene chloride/hexane=1:1) on silica gel.

2.2 Analytical techniques and instruments

The ^{1}H NMR and ^{13}C NMR spectra were measured using $CDCl_3$ solutions with an internal standard of TMS using a Brucker Avance-300 spectrometer. Thermal data were recorded on a differential scanning calorimeter (Perkin Elmer DSC7) at a heating/cooling rate of 5 K min^{-1} over a temperature range from 300 K to above the clearing point. The textures of the liquid crystalline phases were observed with a polarizing microscope, Olympus BH-2, equipped with a Mettler FP82HT hot stage, at a heating/cooling rate of 5 K min-1. Crossed polarizers were used. The IR spectra were measured using KBr disks and a Perkin Elmer 1600 Series FTIR spectrometer.

3. Results and Discussion

3.1 Synthesis of phenyl 6-(4-alkylphenyl)nicotinates

In studying the effect of molecular structure on liquid crystalline properties, it is often profitable to examine the effects of making relatively small changes in the molecular structure of one particular type of liquid crystalline compound, i.e., retaining the greater part of the molecular skeleton unaltered [9]. Therefore, a series of phenyl 6- (4-alkylphenyl)nicotinates **4** (**CnPNP**, n=4-8) were efficiently synthesized by using the Grignard reaction of 4-alkylphenylmagnesium bromide **1** to react with phenyl *N*-phenyloxycarbonylnicotinium chloride **2**, and the resulting 1,2-dihydropyridine intermediate **3** was then oxidized by o-chloranil (Scheme 1). Contrast to the previous method we used [7], phenyl choloroformate was used in this experiment to prepare the electrophile phenyl *N*-phenyloxycarbonylnicotinium chloride **2**. Yields of phenyl 6-(4-alkylphenyl)nicotinates **4** were found to be excellent in a range of 66-93% (**Table** 1). High α-regioselectivity on the pyridine ring were observed in all cases.

3.2 Thermotropic behaviour of phenyl 6-(4-alkylphenyl)nicotinates

Thermotropic behaviours of phenyl 6-(4-alkylphenyl)nicotinates (**CnPNP**, n=4-8) were observed by a polarized optical microscope. **4b**, **4d** and **4e** (**CnPNP**, n=5, 7, 8) of the phenyl 6-(4-alkylphenyl)nicotinates were found to be enantiotropic, whereas **4a** (n=4) and **4c** (n=6) monotropic. Except a short range, unknown and unidentified semectic X phase observed in 4e (n=7) when cooling, smectic A phase (**Figure 1**) was mainly the only liquid crystalline phase observed in all these (**CnPNP**, n=4-8) compounds. One crystal-to-crystal transition and two melting-point transitions were observed in **4d** (n=7) when heating at 5℃/min under a polarized optical microscope. A sharp transition (within a 1K range) was observed for all these compounds in all phase transitions. As Gray pointed out in 1976 that many of the esters could exist in several crystal forms and melt over a very wide temperature range [10].

The benzene analogs, phenyl 4'-alkyl[1,1'-biphenyl]-4-carboxylate [10-11], are usually present in nematic phases. We were curious why smectic A phase was the main liquid crystalline phase observed. However, it is well known that [9] in the smectic layer, dipole moments acting across the long axes of the molecules will reinforce one another and be of importance in enhancing lateral attraction which retain the smectic order. Perhaps it is the dipoles of both pyridine and ester functional groups opposed to each other within the molecule which cause the enhanced lateral attraction and preferably form the smectic A phase.

Figure 1. Focal conic fan texture of the mesophase of CnPNP, n=7 arises from isotropic phase on cooling to 82℃. Polarized optical micrographs with magnification of ×400.

The phase transitions and mesomorphic transition enthalpies of phenyl 6-(4-alkylphenyl) nicotinates (**CnPNP**, n=4-8) were also investigated by DSC. From **Table 2**, a general decreasing of melting points was observed when heating at 5℃/min as the series is ascended. High melting temperatures of **4a** (n=4) and **4c** (n=6) results in their having no smectic phases while heating. Generally, odd numbers of alkyl chains provide higher isotropic-to-smectic transition temperatures and wider mesomorphic ranges than those even-number homologues. The average value of the melting enthalpies of phenyl 6-(4-alkylphenyl)nicotinates (**CnPNP**, n=4-8) is 65.84 Jg^{-1}. The smectic A-to-isotropic transition enthalpies are around 5 Jg^{-1}.

Table 2. Transition temperatures （℃） and enthalpies （Jg^{-1}） by DSC for compounds 4a-4e (CnPNP, n = 4-8).

Entry	n	Phase transitions/℃(corresponding enthalpy changes/ Jg-1)
4a	4	Cr 116.4(77.14)I 89.7(-8.30) S_A 70.9(-47.11)Cr
4b	5	Cr 106.3(67.06)S_A 111(8.21)I 106.7(-11.41) S_A 74.5(-53.92)Cr
4c	6	Cr 104.74(67.23)I 92.9(-6.61)S_A 66.8(-50.25)Cr
4d	7	Cr 70.9(12.45)Cr' 95.1[b](42.43)S_A 110.6(5.08)I 101.8(-10.76)S_A 66.4 (-26.79)S_X 64(-12.49)Cr
4e	8	Cr 96.3(62.89)S_A 110.7(4.87) I 101.1(-6.87) S_A 73.3(-62.5)Cr

aCr = crystal, S_A = semectic A phase, S_X = semectic X phase, I = isotropic phase.

[b]Two melting-point transitions were observed for this compound.

In conclusion, we have synthesized a homologous series of pyridine-containing liquid crystalline compounds, phenyl 6-(4-alkylphenyl)nicotinates (**CnPNP**, n=4-8), and investigated their phase transition behaviours. **4b**, **4d** and **4e** (**CnPNP**, n=5, 7, 8) of the phenyl 6-(4-alkylphenyl)nicotinates were found to be enantiotropic, whereas **4a** (n=4) and **4c** (n=6) monotropic. Except a short range, unknown and unidentified semectic X phase observed in **4e** (n=7) when cooling, smectic A phase was the only liquid crystalline phase observed in all these (**CnPNP**, n=4-8) compounds. The pyridine ring in the rigid core should give a dipole moment preferentially in the lateral direction relative to the molecular axis, so increasing intermolecular lateral interactions. This may be related to the generation of soly the smectic A phase. By contrast, for example: the benzene analogs, phenyl 4'-alkyl[1,1'-biphenyl]-4-carboxylate, are usually present in nematic phases.

4. Acknowledgement

The authors gratefully acknowledge the financial support of the SVD section and the cross cultural centre of Fu Jen Catholic University. Grant 328-1-2001-1-218.

References

(1) Nash, J. A., Gray, G. W., 1974, *Mol. Cryst. Liq. Cryst.*, 25, 299-321.

(2) Pavelyuchenko, A. I., Smirnova, N. I., Mikhailova, T. A., Kovshev, E. I., Titov, V. V., 1986, *Zh. Org. Khim.*, 22(5), 1061-1065.

(3) Burrow, M. P., Gray, G. W., Lacey, D., Toyne, K. J., 1988, *Liquid Crystals*, 3, 1643-1653.

(4) (a) Reiffenrath, V., Bremer, M., 1994, *Angew. Chem. Int. Ed. Engl.*, 33, 1386-1389. (b) Asano, T., Uenoyama, M., Moriya, K., Yano, S., Takatani, S., Kagabu, S., 1997, *Liquid Crystals*, 23, 365-369. (c) Moriya, K., Harada, F., Yana, S., Kagabu, S., 1988, *Liquid Crystals*, 27, 1643-1653.

(5) Poetsch, E., Meyer, V., Hittich, R., Plach, H., Kraus, J., Kompter, H-M., Coates, D., Smith, G. European Patent Appl. EP 0519370 A2 19920615 (1992), 1993, Chem. Abst., 118, 191554w. (b) Nigorikawa, K., Ichihashi, M. Jpn. Kokai Tokkyo Koho JP 04,213,386 [92,213,386], 04 Aug 1992, 1992, *Chem. Abst.*, 118, 136379t.

(6) (a) Comins, D. L., Abdullah, A.H., 1982, J. *Org. Chem.*, 47, 4315-4319. (b) Comins, D. L., Stroud, E. D., Herric, J. J., 1984, *Heterocycles*, 22, 151-157. (c) Yamaguchi, R., Nakazono, Y., Kawanisi, M., 1983, *Tetrahedron Lett.*, 24, 1801-1804. (d) Akiba, K., Iseki, Y., Wada, M., 1982, *Tetrahedron Lett.*, 23, 429-432.

(7) Chia, W-L., Shen, S-W., Lin, H.-C., 2001, *Tetrahedron Lett.*, 42, 2177-2179.

(8) (a) Chia, W-L., Shiao, M-J., 1991, *Tetrahedron Lett.*, 32, 2033-2034. (b) Shing, T-L., Chia, W-L., Shiao, M-J., Chau, T-Y., 1991, *Synthesis*, 849-850. (c) Shiao, M-J., Chia, W-L., Peng, C-L.: Shen, C-C., 1993, J. *Org. Chem.*, 58, 3162-3164. (d) Shiao, M-J., Shih, L-H., Chia, W-L., Chau, T-Y., 1991, *Heterocycles*, 32, 2111-2118.

(9) Gray, G. W., 1966, Mol. *Cryst. Liq. Cryst.*, 1, 333-349.

(10)Coates, D., Gray, G. W., 1976, *Mol. Cryst. Liq. Cryst.*, 37, 249-262.

(11)(a) Coates, D., Gray, G. W., 1975, *Mol. Cryst. Liq. Cryst.*, 31, 275-283. (b) Sadashiva, B. K., 1979, Mol. Cryst. Liq. Cryst., 55, 135-142.

received October 27, 2005
accepted November 19, 2005

一系列苯基酸 6-(4-烷苯基)尼古丁酯液晶化合物的合成及熱向性研究

賈文隆　夏忠平
輔仁大學化學系

林宏洲
交通大學材料科學與工程系

摘　要

我們已合成一系列含比碇液晶化合物 苯基酸 6-(4-烷苯基)尼古丁酯。其合成是利用 4-烷基溴化苯 製成的格里納試劑 與 苯基酸 N-苯氧醯基 氯化尼古丁酯 進行的格里納反應得一 1,2-二氫化比碇中間物，再經由氧化劑氧化便可得所期望的 苯基酸 6- (4-烷苯基)尼古丁酯。實驗結果顯示所有的例子均具有極佳的產率和極高的α區域位置選擇性。這一系列化合物 苯基 6- (4-烷苯基)尼古丁酸酯 的熱分析研究已由熱式差掃瞄卡計及偏光光學顯微鏡來完成。層列型 A 相是其唯一的介相。

關鍵字：含比碇液晶化合物，合成，熱分析研究

Realization of Current-Mode Notch and All-pass Filters using Single CFCCII

Yung-Chang Yin
Department of Electronic Engineering
Fu Jen Catholic University
Taipei, Taiwan 242, R.O.C.

ABSTRACT

A new circuit configuration for the current-mode first order and biquadratic filters using a single four-terminal active current conveyor (CFCCII) is presented. The circuit configuration can be used to synthesize notch and all-pass functions. The all-pass circuit uses three resistors and only one capacitor. The active and passive sensitivities of the notch filter have been calculated. Moreover, the quality factor ϑ and the central frequency ω_0 of the notch filter are insensitive to the current tracking error of the CFCCII. Finally, three experimental results are included to verify the theoretical prediction.

Key words: four-terminal active current conveyors, sensitivity

I. INTRODUCTION

Some recent literature has mentioned that the circuits based on current-mode amplifier will operate at high signal bandwidth, with greater linearity and with a larger dynamic range than their voltage-mode counterpart[1][2]. In addition to the above advantages, the current-mode approach can easily cascade the current-mode filters without additional matching circuits. Hence, the current-mode circuits have been receiving significant attention in the field of

---

* Corresponding author. Tel:+886-2-29053801
E-mail: yin@ee.fin.edu.tw

analogue signal processing[3]-[10]. The four-terminal active current conveyor (CFCCII) can circumvent the finite gain-bandwidth limitation of the conventional operational amplifier and offer both a constant bandwidth and a high slew rate (i.e. 2000 V/us) [3][4]. Therefore, applications in the realization of various filter functions using some CFCCIIs have been published [11]-[15]. In 1996, Gunes and Anday presented a multifunction biquadratic filter using three CFCCIIs [12]. In 1998, Chang and Tu proposed two universal active filters with current gain using four CFCCIIs [13]. In 2003, the author used two CFCCIIs to synthesize biquadratic filters [14]. In 2004, the author used single CFCCII to synthesize highpass, lowpass and bandpass filters [15]. However, the current-mode notch and all-pass filters using only one CFCCII have never been synthesized. For this reason, the objective in this paper is to apply a single CFCCII to synthesis the circuit configuration for current-mode notch and all-pass filters. These proposed current-mode filters have high output impedance, so they can be cascaded without additional buffers. The all-pass circuits have minimum passive elements. Furthermore, the quality factor ϑ and the central frequency ω_o of the notch filter are insensitive to the current tracking errors of a CFCCII. Finally, three experimental results are given to confirm the afore mentioned theoretical analysis.

II.CIRCUIT DESCRIPTION

The circuit symbol for a CFCCII is shown in Fig.1. The port relations of a CFCCII can be characterized as $i_z = - i_x$, $v_x = v_y$, $i_y = 0$, and $i_0 = i_x$. The proposed circuit using a single CFCCII is shown in Fig.2 and the transfer function can be expressed as:

$$\frac{I_o}{I_{in}} = \frac{Y_2 Y_3 - Y_1 Y_4}{Y_2 Y_3 + Y_1 Y_2} \tag{1}$$

where Y_1 - Y_4 are the admittances. The notch and all-pass filters can be described as below:

1.The current-mode notch filter:

If the admittances are chosen as $Y_1 = G_1$, $Y_2 = SC_2 + G_2$, $Y_3 = SC_3 + G_3$ and $Y_4 = SC_4$, equation (1) will be

$$\frac{I_o}{I_{in}} = \frac{S_2 C_2 C_3 + S(C_2 G_3 + C_3 G_2 - C_4 G_1) + G_2 G_3}{S^2 C_2 C_3 S(C_2 G_3 + C_3 G_2 + C_2 G_1) + G_2 G_3 + G_1 G_2} \tag{2}$$

hence, if $C_2G_3 + C_3G_2 = C_4G_1$, a second-order notch filter, shown in Fig.3, can be constructed. The central frequency ω_o and the quality factor ϑ are given by

$$\text{the central frequency: } \omega_o = \left(\frac{G_1G_2+G_2G_3}{C_2C_3}\right)^{1/2} \tag{3}$$

$$\text{the quality factor: } \vartheta = \left\{\frac{[C_2C_3(G_2G_3+G_1G_2)]}{C_2G_3+C_3G_2+C_2G_1}\right\}^{1/2} \tag{4}$$

The quality factor ϑ and the central frequency ω_o of the proposed filters are derived.

2.The current-mode allpass filter:

If the admittances are chosen as $Y_1 = SC_1$, $Y_2 = Y_4 = G$, $Y_3 = G_3$ and $Y_1 = G_1$, $Y_2 = Y_4 = G$, $Y_3 = SC_3$, thus two first order current-mode all-pass circuits are constructed. The all-pass filter, shown in Fig.4(a) and Fig.4(b), are given by the following equations, respectively:

$$\frac{I_o}{I_{in}} = \frac{-S+[G_3/C_1]}{S+[G_3/G_1]} \tag{5}$$

$$\frac{I_o}{I_{in}} = \frac{S-[G_1/C_3]}{S+[G_1/G_3]} \tag{6}$$

Thus, the circuits yield a phase from *0°* to *-180°* and from *180°* to *0°* without constant loss in an all-pass characteristic, respectively. Clearly, notch and all-pass filters using single CFCCII have been realized. Meanwhile, the central frequency ω_o and the quality factor ϑ of the notch filter are also derived.

III.SENSITIVITY ANALYSIS AND

Taking into consideration the non-idealities of CFCCII, namely $V_x = \alpha V_y$, $\alpha = 1-\varepsilon_1$, $/\varepsilon_1/ \ll 1$, denotes the voltage tracking error and $I_o = \beta I_x$, $\beta = 1-\varepsilon_2$, $/\varepsilon_2/ \ll 1$, denotes the output current tracking error, the transfer function (1) becomes

$$\frac{I_o}{I_{in}} = \frac{\beta[(1-\alpha)Y_1Y_3+Y_2Y_3-\alpha Y_1Y_4]}{(1-\alpha)Y_1Y_3+Y_1Y_2+Y_2Y_3} \tag{7}$$

By relating a sensitivity parameter F to the element of variation X_i by

$$S_F^{X_1}=\frac{X_1}{F}\,\frac{dF}{dX_i}$$

it is easy to show that the active and passive sensitivities of the parameters ω_o and ϑ can be expressed as:

1. The passive sensitivities of the parameters ω_o and ϑ

$$S_{G_2}^{\omega o}=\frac{1}{2}\,,\ S_{C_2}^{\omega o}=S_{C_3}^{\omega o}=-\frac{1}{2}\,,\ S_{G_1}^{\omega o}=\frac{G_1G_2}{2\Delta_1}\,,\ S_{G_3}^{\omega o}=\frac{G_2G_3}{2\Delta_1}$$

$$S_{C_2}^{\vartheta}=\frac{G_2[(G_1+G_3)(G_2C_3-G_1C_2-G_3C_2)]}{2\Delta_1\Delta_2}$$

$$S_{C_3}^{\vartheta}=\frac{G_2[(G_1+G_3)(C_2G_3+C_2G_1-C_3G_2)]}{2\Delta_1\Delta_2}$$

$$S_{G_1}^{\vartheta}=S_{G_3}^{\vartheta}=\frac{G_1G_2(G_2C_3-G_3C_2-G_1C_2)}{2\Delta_1\Delta_2}$$

$$S_{G_2}^{\vartheta}=\frac{G_2(G_1+G_3)(C_2G_3+C_2G_1-C_3G_2)}{2\Delta_1\Delta_2}$$

2. The active sensitivities of the parameters ω_o and ϑ

$$S_{\alpha}^{\omega_o}=S_{\beta}^{\omega_o}=S_{\alpha}^{\vartheta}=S_{\beta}^{\vartheta}=0$$

where $\triangle_1=G_1G_2+G_2G_3$ and $\triangle_2=C_2G_3+C_3G_2+C_2G_1$

The passive and active sensitivities of notch have been derived. Clearly, the passive sensitivities of the proposed filter are very low. Moreover, the natural frequency ω_o and the quality factor ϑ of the proposed current-mode filters are insensitive to the current tracking error of a CFCCII.

IV. EXPERIMENTAL RESULTS

To verify the theoretical prediction of the proposed circuit, three filter prototypes have been constructed with discrete components. The AD844 can be used to construct as a CFCCII. All the experiments of the three mentioned filters are described below:

a) A biquadratic notch filter, shown in Fig.3, was constructed with $G_1=G_2=G_3=10^{-3}\ \Omega^{-1}$, $C_2=C_3=1uF$, and $C_4=2uF$. The experimental results for the gain and phase responses are shown in Fig.5(a)(b).

b) Two allpass filters, shown in Fig. 4(a)(b), was constructed with $G_2= G_4=G=10^{-3}$, $G_3= 10^{-3}\ \Omega^{1}$, $C_1=1uF$ and $G_1=10\text{-}3\ \Omega^{1}$, $G_2= G_4=G =10^{-3}\ \Omega^{1}$, $C_3=1uF$, respectively. The experimental results for the phase responses of Fig. 4(a) are shown in Fig.5(c) varying from 0° to -180° and Fig. 4(b) are shown in Fig.5 (d) varying from 180° to 0° .

The theoretical analysis correlated with the measured results with few errors which due to the errors of the use of passive elements. However, the experimental results confirm the results of the theoretical analysis.

V.CONCLUSION

A new configuration circuit of notch and all-pass filters using single a CFCCII has been presented. These filters can be achieved from the same configuration. The proposed current-mode single-CFCCII filter can be easily cascaded with matching circuits. The central frequency ω_o and the quality factor ϑ of the notch filter are insensitive to the current tracking error of a CFCCII. Finally, three experimental results confirmed the theoretical analysis.

VI.ACKNOWLEDGMENT

The author wishes to express his thanks for the financial support of the Office of Research and Development Fu Jen Catholic University.

REFERENCES

(1) B.Wilson, "Recent Developments in Current Conveyors and Current-Mode Circuits", *IEE Proc-G*, vol. 137, no. 2, pp.63-77, 1990.

(2) G.W.Rober and A.S.Sedra, "All Current-Mode Frequency Selective Circuits", *Electron. Lett.*, Vol.25, pp.759-761, 1989.

(3) C.Toumazou and E.J.Lidgey, "Universal active filter using current conveyous", *Electron. Lett.*,vol. 22, pp.662-664, 1986.

(4) Y.Sun and J.K.Fidler, "Versatile active biquad based on second-generation current conveyors", *Int. J Electron.*, vol. 76, pp91-98 , 1994.

(5) V.K.Singh and R.Senani, "New multifunction active configuration employing current conveyors", *Electron. Lett.*, vol. 26, pp.1814-1816, 1990.

(6) G.W.Robert and A.S.Sedra, "A general class of current amplifier-based biquadratic filter circuits", *IEEE Transactions on Circuits and Systems.*, vol. 39, pp.257-263 , 1992.

(7) C.M.Chang, "Universal active current filters using single second-generation current conveyors", *Electron. Lett.*, vol. 27, no.18, pp.1614-1617 , 1991

(8) C.M.Chang and P.C.Chen, "Universal active current filter with three inputs and one output using current conveyors", *Int. J Electron.*, vol. 71, no.5, pp.817-819 , 1991.

(9) R. Senani, "New current-mode biquad filter", *Int. J Electron.*, vol. 73, no. 4, pp.735-742 , 1992.

(10) Y.C. Yin, "A Current-mode Biquad filter with multi-output using CCIIs", *Journal of the Chinese Institute of Electrical Engineering.*, vol. 3, no. 4, pp.367-370 ,1996.

(11) C.L. Hou and J.S. Wu, "Universal cascadable current-mode biquad using only four four CCIIs", *Int. J Electron.*, vol. 82, no.2, pp.125-129 , 1997.

(12) E.O.Gues and F. Anday, "Realization of current-mode universal filter using CFCCIIps ", *Electron. Lett.*, vol. 32, pp.1081-1082 , 1996.

(13) C.M. Chang and S.H. Tu, "Universal current-mode filters employing CFCCIIps", *Int. J Electron.*, vol. 85, no.6, pp.749-754 , 1998.

(14) Y.C. Yin, "Current-Mode Biquad Using Two CFCCIIps ", *Fu Jen Studies.*, vol. 3, no. 4, pp.367-370 , 2003.

(15) Y.C.Yin and Y.C. Liou "Realization of Current-Mode Highpass Lowpass and Bandpass Biquad Filters using Single CFCCIIp", *Fu Jen Studies*, No.38, 2004, pp.89-99

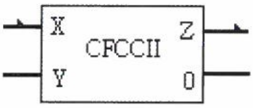

Fig.1. A CFCCII symbol

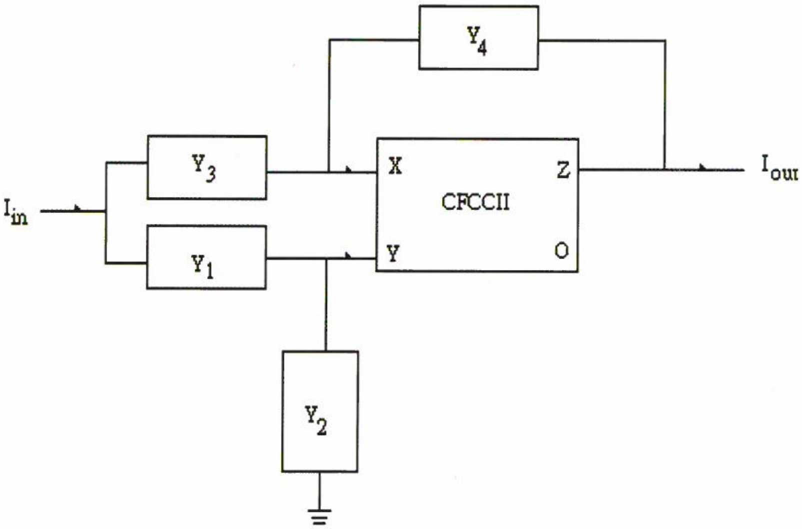

Fig.2. The proposed circuit using a single CFCCII

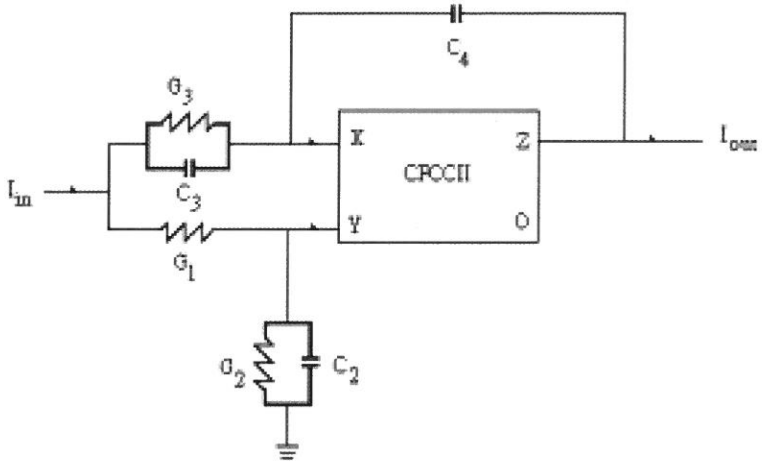

Fig.3. Second order notch filter using a single CFCCII

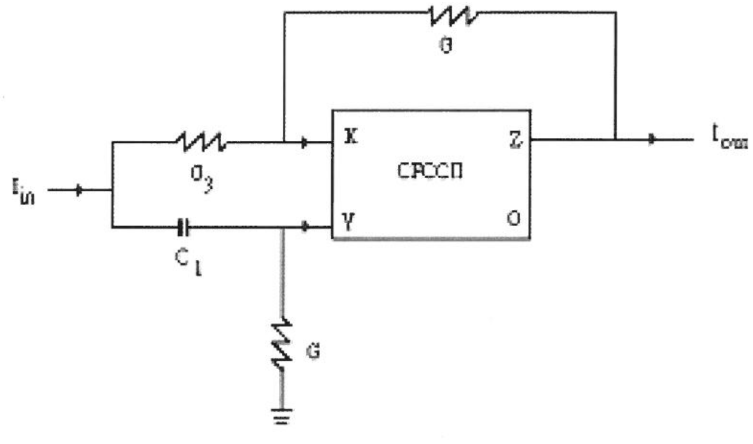

Fig.4 (a): The current-mode allpass filter from 0° to -180°

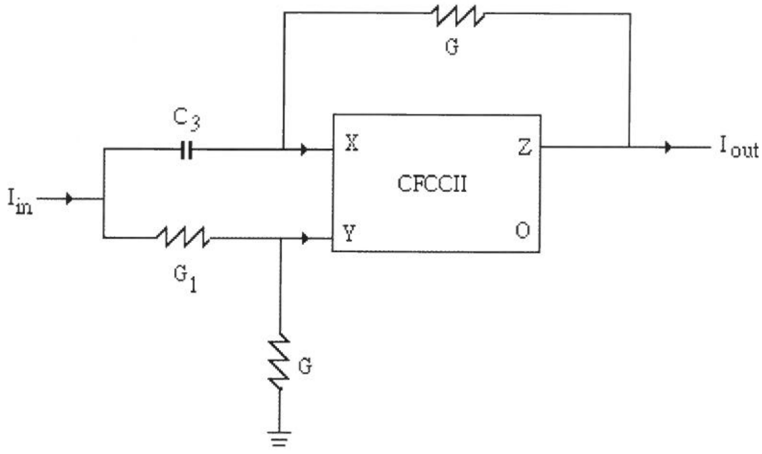

Fig.4 (b): The current-mode allpass filter from 180° to 0°

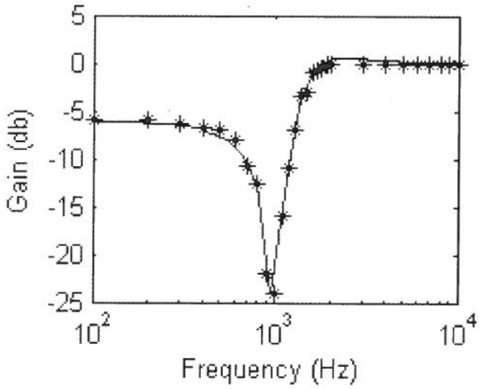

Fig.5 (a): Notch filter gain response

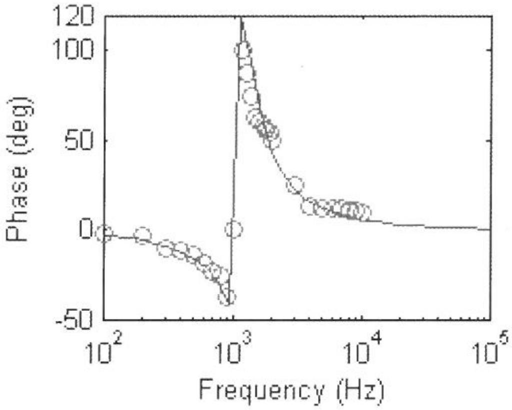

Fig.5 (b): Notch filter phase response

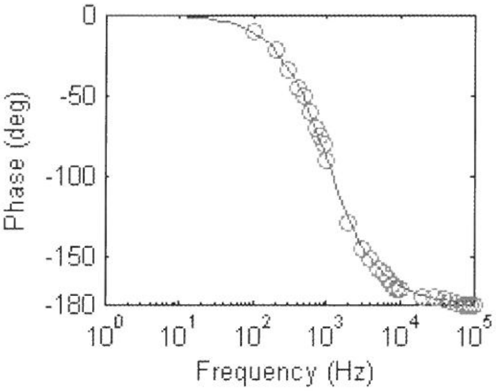

Fig.5 (c): Allpass filter phase response from 0° to -180°

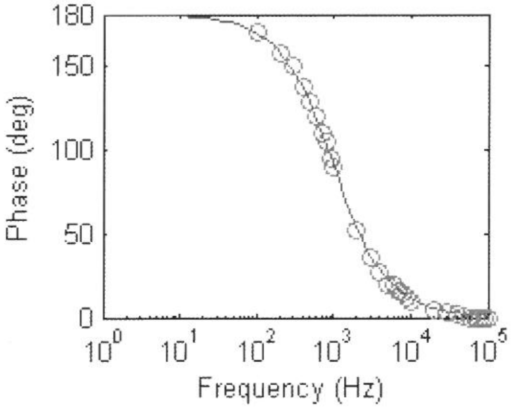

Fig.5 (d): Allpass filter phase response from 180° to 0°

Fig.5. (a) : Notch filter gain response

(b) : Notch filter phase response

(c) : Allpass filter phase response from 0° to -180°

(d) : Allpass filter phase response from 180° to 0°

***: experimental result for gain**

o: experimental result for phase

received October 27, 2005
revised November 14, 2005
accepted November 25, 2005

使用單一四端主動電流傳輸器合成電流式帶拒與全通濾波器

鄞永昌

輔仁大學大學電子工程學系

摘　要

本文提出使用單一四端主動電流傳輸器合成新結構一階與二階式電流形態濾波器，此單一四端主動電流傳輸器合成之濾波器可合成二階式帶拒和一階全通二種功能。全通濾波器僅僅使用三個電阻與一個電容的被動元件；而帶拒濾波器之主動和被動靈敏度在文中也被推導出，其且品質因素與中心頻率沒有電流之軌跡誤差問題。最後以三個實驗驗證本文之理論預測。

關鍵詞：四端主動電流傳輸器，靈敏度

PAPM: 一個新的擬真與非擬真混合成像演算法

王宗銘* 李孟燦**

國立中興大學資訊科學系
台中市 402 南區國光路 250 號

摘 要

本文提出一個新的擬真與非擬真混合成像演算法。這個演算法簡稱 PAPM 演算法，能夠同時產生出類似照片般真實的擬真影像與具有手繪風格的非擬真影像。就我們所知，PAPM 爲首創的擬真與非擬真混合演算法，目前文獻上尚未有類似之演算法。

PAPM 演算法以光子映像技巧(Jensen,2002)爲基礎，爲一個兩階段(2-pass)的成像演算法；包含與視點無關的「光線路徑(light pass)計算」及與視點相關的「視線路徑(eyes pass計算)」。在光線路徑計算中，我們由光源處灑下光子。這些光子根據 3D 場景物體的物理特性，做反射或折射的彈跳後，靜止於物體的表面上。我們隨即將這些光子記錄在多維度二元搜尋樹中(KD-tree)，以利第二階段的快速搜尋。第二階段爲視線路徑(eyes pass)計算，此階段首先以視點爲起始點，逐一對視平面的每個像素點發出射線(rays)，此射線與物體做交點測試，得知交點之位置與物件的分類屬性。其次，若物件之分類屬性爲擬真物件，則以該交點爲中心，搜尋適量的光子個數，從而計算出該像素的擬真影像照度。反之，若爲非擬真物件，則搜尋光子與物體的 3D 資訊，進行筆觸成像演算法(SBR)，來計算出該像素點的手繪風格的非擬真影像照度。據此，透過此兩階段的計算，我們就可同時產生具有擬真與非擬真效果的圖像。

---

* Corresponding author. Tel: +886-4-22840497 ext 915
E-mail: cmwang@cs.nchu.edu.tw

** E-mail: holylight@cs.nchu.edu.tw

我們實現 PAPM 演算法，並實作一套成圖系統。我們以個人電腦爲平台進行測試，結果顯示 PAPM 演算法的確可以達成預期產生擬真與非擬真混合式風格的影像。總結本文，我們提出文獻上首創的混合成像演算法(PAPM)。此演算法具有三個優點：(1) 擬真與非擬真混合：可產生兼具擬真與非擬真效果的靜態影像；(2) 優異的非擬真圖像品質：我們提出 3 個技巧，可以提高筆觸成像演算法的結果；(3) 有效的計算：PAPM 使用兩階段計算，故若有視點改變時，我們僅需重新執行與視點相關的視線路徑(eyes pass)計算即可。因此 PAPM 演算法可以使用於視點相依各種應用，例如動畫製作等。[1]

關鍵詞：擬真成像，非擬真成像，全域照度，光子映像演算法，筆觸成像演算法。

一、前　言

在電腦圖像領域，針對擬真與非擬真成圖 (photorealistic rendering and non-photorealistic rendering) 通常使用不同的演算法。擬真成像的領域之中，通常使用全域照度演算法 (Global Illumination Algorithms)用來模擬出具有類似真實世界的自然光、影現象的擬似照片般真實的圖像。

全域照度演算法的原理是考慮光線與物體材質之間的交互作用，並且遵循已知的物理法則，包括折射，反射，聚光，陰影，以及空間中若有介質(participating media)所產生的煙霧等。均可以透過以物理法則爲基礎 (physical based) 的成像演算法進行計算與模擬。這些自然界的物理現象可以透過全域照度演算法來達成。

全域照度演算法全部是考慮於３D模型。考慮 3D模型的好處在於一旦移動視點，可以重新計算便可以得到不同角度的結果以得到新的影像。並且不需要事先準備影像來當成演算法的輸入。在這些演算法之中，由於光子映像(Jensen,2002)是兩階段成像演算法，所以我們認爲較適合當成 PAPM 的基礎。

非擬真成像演算法的領域非常廣泛，包括點畫(Lu,2003)，鋼筆畫(Deussen,2000)，以及素描(Praun,2001)(Lake,2000)等等。其中一項探討的重要議題，在於如何模擬畫家的手法與筆觸(Stoke based painterly rendering, SBR)。其目的是產生如同畫家手繪的影

像。相對於 PR 演算法，SBR 演算法較多都是應用在 2D 影像(Hertzmann,1998)(Hertzmann,2002)(Haeberli,1990)(Hausner,2001)(Hertzmann,2001)上。在 3D 模型的 SBR 演算法(Meier,1996)(Winkenbach,1994)並不多見。Barbara J. Meier 提出的 Painterly Rendering for Animation 有不錯的結果，但是該論文仍是僅能產生非擬真效果，不能同時產生具有擬真與非擬真效果之圖像。

繪畫的風格雖然依照畫家的手法有這不同的型態，不過大致上也可以分成寫實與抽象兩種類型。寫實的風格比較偏向擬真的概念，而抽象的風格則是偏向非擬真的概念。因此，將 PR 與 NPR 的效果呈現在同一場景之中，是較有彈性與多元的作法。如此一來不但具備手繪風格可以突顯強調主題風格，並有自然界的現象搭配在主題周圍。

直到目前爲止，文獻上尚未有研究學者發表過可以在場景中同時呈現擬真與非擬真R兩種不同風格影像的演算法。因此，我們嘗試著把這兩大議題的優點擷取出來並做合併。我們希望在不藉助後製作的前提之下能夠針對 3D 場景，在單一場景中，同時模擬出擬真(PR)與非擬真(NPR)兩種不同風格的影像。

據此，我們提出PAPM 演算法來達到這個目標。本篇論文的 3D 場景物件可以是任意的物體(arbitrary object)，並不侷限多邊型模型(polygon model)。PAPM 演算法的原理是使用兩階段來處理，分別爲光線路徑計算與視線路徑計算。在第一階段中，我們由光源中灑出光子，使其在場景中彈跳，並以有效的資料結構記錄這些光子靜止於物體表面後之最後位置。第二階段中，我們發射光線與 3D 場景做交點測試，並利用這些交點得知 3D 模型物體之屬性。我們再利用已建好的資料結構，做有效的搜尋，以提供必要之光子資訊。此資訊也可提供了擬真成像時所需要的照度資訊，及非擬真成像時所需要的筆觸(strokes)大小，顏色，方向等資訊。有了這些資訊，我們就可以對非擬真屬性的物體進行筆觸成像演算法(SBR)。我們實作PAPM 演算法，並發展出一個成圖系統(rendering system)。此系統所產生的影像如圖 1 所示，同時具備擬真的透明球體光影效果與非擬真的狐狸筆觸效果。

本文架構如下：第二節回顧光子映像(Photon Mapping)演算法與３D 的 SBR 演算法之相關研究；第三節介紹 PAPM 演算法之流程；第四節展示 PAPM 的執行結果，系統所輸出的影像顯示的確可以同時模擬 PR 與 NPR 的風格；最後，我們總結本文並建議未來工作。

圖 1　我們實做 **PAOM** 演算法之成像。場景之中，同時具備擬真的透明球體光影現象以及非擬真狐狸筆觸手繪風格。

二、相關工作

2.1　光子映像(**Photon Mapping**)演算法

擬真成像可以透過全域照度演算法模擬。全域照度(global illumination)基本上有分成兩種不同的技術，第一、point sampling (光線追蹤法(ray tracing) (Ward,1992)(Shirley, 1990)(Arvo,1986)。第二、有限單元輻射法(finite elements radiosity) (Myszkowski,1997) (Volevich,1999)。當然還有其他混合這兩種技術的其他演算法。光線追蹤法與有限單元輻射法最大的差異有下列兩點 ：第一、模型不需要切割(no tessellation necessary)。第二、模擬反射(specular reflections)非常容易。

理論上真實世界的物體所產生的形狀與顏色。均透過光線的直射或反射至人的眼睛進而成像。但是實作上如果以這種方式，在 3D 場景之中。藉由光源，經由數次反射，然後射向視點。勢必花費相當多的時間。原因是因爲會有許多的射線，沒有射向視點而

形成無效的路徑。所以為了解決這個問題，光線追蹤法(ray tracing) 反其道而行。利用光的可逆性質。由視點發射視線路徑，計算光源與週遭環境對視線貢獻的照度。

但是這種方式雖然可以加快成像。不過，造成焦散現象 (caustic，如圖 2) 的效果並不明顯。要使得焦散現象明顯，我們必須使用光線路徑來產生焦散現象的效果。

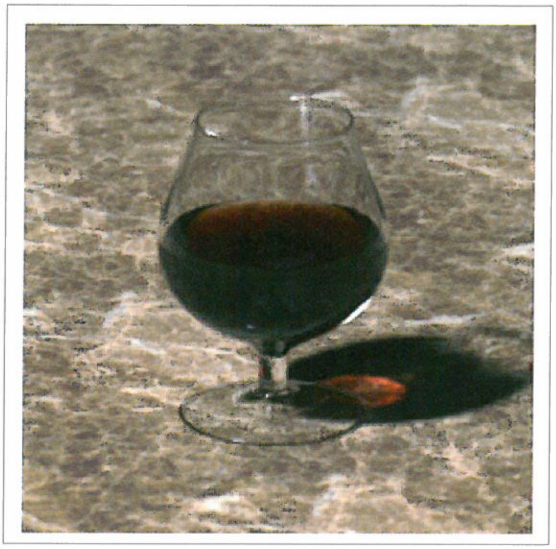

圖 **2** 有散焦現象**(caustic)**的酒杯

因此為了兼顧時間與效果，Henrik Wann Jensen 提出了光子映像(Photon Mapping)演算法(Jensen,2002)。該演算法是屬於光線追蹤法的一種。光子映像演算法採取兩種方式並行，即使用兩階段性的成像。第一階段(光線路徑)先將光子(photons)由光源均勻灑下，並且依照光的物理性質，遵循物體表面的材質特性，來決定光子是折射反射或是吸收。然後紀錄光子在空間中的位置，並存於kd-tree(Bentley,1975)之中(圖 3)以利第二階段的查詢使用。而在第二階段(視線路徑)，由視點位置與視平面(view plane)決定發射視線路徑的數量。這些視線路徑跟場景之中的物體作交點測試，決定可視點之後。依照可視點的位置，搜尋 kd-tree 裡面的光子。經由適當的光子數，估計出正確的照度(圖 4)，其演算法流程圖如圖 5 所示。

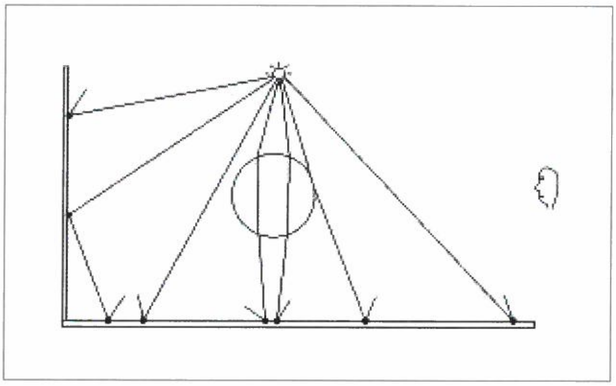

圖 **3** 第一階段 光子在模型中彈跳

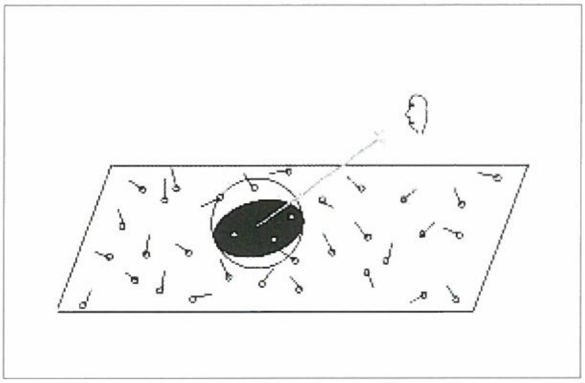

圖 **4**　第二階段 收及光子的資訊來計算照度

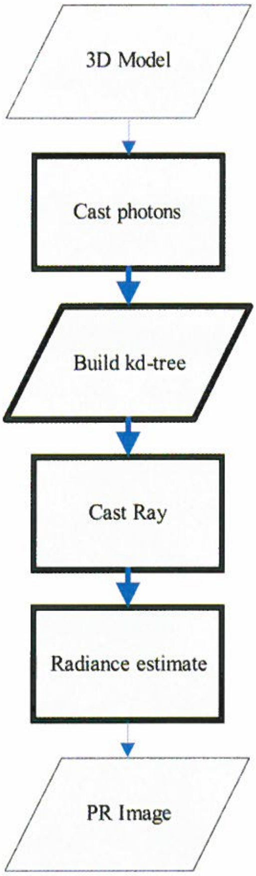

圖 **5**　**photon mapping** 演算法的流程圖

光子映像有四個特點：第一、所有的全域照度的效果都可以模擬(all global illumination effects can be simulated)。第二、可使用任意幾何形狀的物件(arbitrary geometry， no meshing)。第三、使用少量的記憶體(low memory consumption)。第四、結果正確(result is correct)。

光子映像演算法的屬於兩階段的成像演算法。兩階段的演算法有兩個好處。除了上述的可以有效的模擬出焦散現象之外。因為第一階段的光線路徑是與視點無關，也就是說視點改變並不影響這個部分的結果。所以一旦視點改變之後，只需要計算第二個階段的視線路徑即可。因此，我們針對光子映像做出了修正，讓第一階段可以提供資訊給擬真與非擬真成像使用。並在第二階段修正成可以判斷應該做擬真或非擬真成像。如此一來就可以在同一場景之中，產生兩種不同效果的影像。因此，我們認為Photon Mapping 比較適合用來發展 PAPM 演算法。

2.2 三度空間的筆觸成像演算法(SBR)

人們不僅僅只對真實的影像有興趣，對於非擬真成像(non -photorealistic rendering)的研究也非常廣泛。非擬真成像主要的目的是利用電腦進行演算，來產生如 ：素描，水彩畫，和油畫等等效果的影像。而在非擬真成像的眾多演算法之中，其中有一部分是在探討筆觸成像演算法(Litwinowicz,1997)(SBR)。所謂的筆觸成像就是藉由模擬畫家手法，以不同筆觸繪製一幅圖畫。利用線條與顏色來描製場景，使用深淺來營造畫面的層次感。這樣一來便可以透過鮮明簡單的線條可以更強烈的突顯出主題與畫家的風格。

針對 3D 模型所發表的 SBR 演算法(Meier,1996)(Winkenbach,1994)(Chi,2005)為數不多。最重要的 3D 模型筆觸成像(3D Stroke-based Rendering)演算法首推 Meier 發表的 Painterly Rendering for Animation (Meier,1996)一文。其流程如圖 6 所示。首先，是先將幾何物體(geometry object)三角化並在上面取粒子(Particles)，記錄這些粒子的空間位置， 這些粒子必須再做視平面投影(camera transfer)。讓筆觸的方向會隨著視點不同而改變，保持合理的一致性。另外將幾何物體透過成像系統產生參考圖片(reference pictures)，包括顏色，方向和大小，這三種資訊經過視平面投影，並配合事先準備好的筆觸形狀，將所有粒子依照距離視點的遠近做排序。所有的點與方向都投影到視平面。一個粒子表示一個筆觸(stroke)，所有的筆觸都必須依照遠近的順序畫於視平面上。當然可以配合著距離調整筆觸的大小。一般而言，近距離的我們使用小的筆觸，遠距離的使用大的筆觸。若是視點改變之後，必須重新排序所有的粒子。然後再重複上面的步驟來計算

出 3D 模擬畫家筆觸的成像。

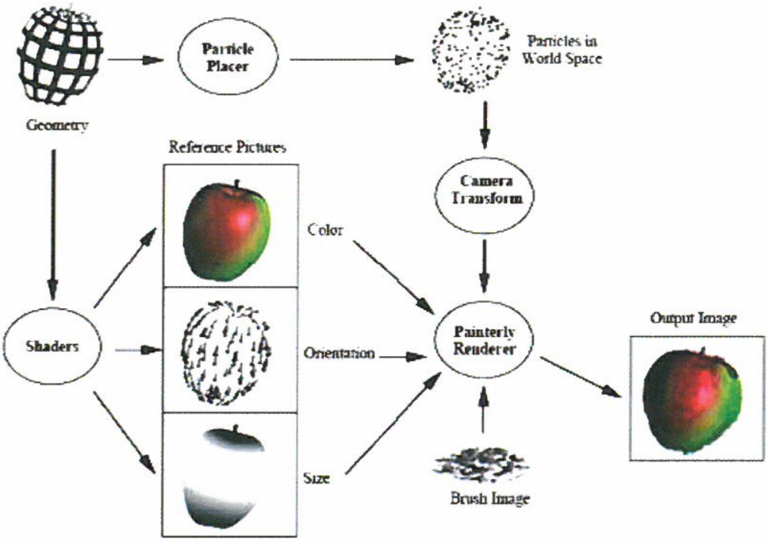

圖 6　**Painterly Rendering for Animation** ：在個三角形中產生粒子，然後依照輸入的方向大小與顏色來描繪 **SBR**。

但是 Meier 演算法只能產生非擬真成像。與我們所要的結果不同，我們需要的是在同一場景可以達到兩種風格的影像。因此 Meier 的演算法我們並不採用。而是自己依據 PAPM 的特性，來設計出自己的非擬真成像演算法。

三、PAPM 演算法

在本篇論文，我們提供一個全新的演算法(Painterly Rendering Photon Mapping, PAPM)可以同時呈現擬真與非擬真的成像效果。

3.1　PAPM 針對擬真成像所做的修正

爲了可以繪製 3D 的 SBR，我們必須修改光子映像演算法。讓該演算法可以提供繪製 SBR 的資訊。(如圖 7 所示)

總言之，因爲 Painterly rendering for Animation 使用的多邊形成像系統(polygon shader)。即使要模擬真實場景，也無法達至真正擬真的效果。此外，Painterly rendering for Animation 與兩階段的成像不同，該演算法是使用視點相依的成像。在視點改變之後，要模擬真實場景，所有資訊必須全部重新計算。因此，PAPM 可以模擬 Painterly rendering for Animation 無法產生的效果。

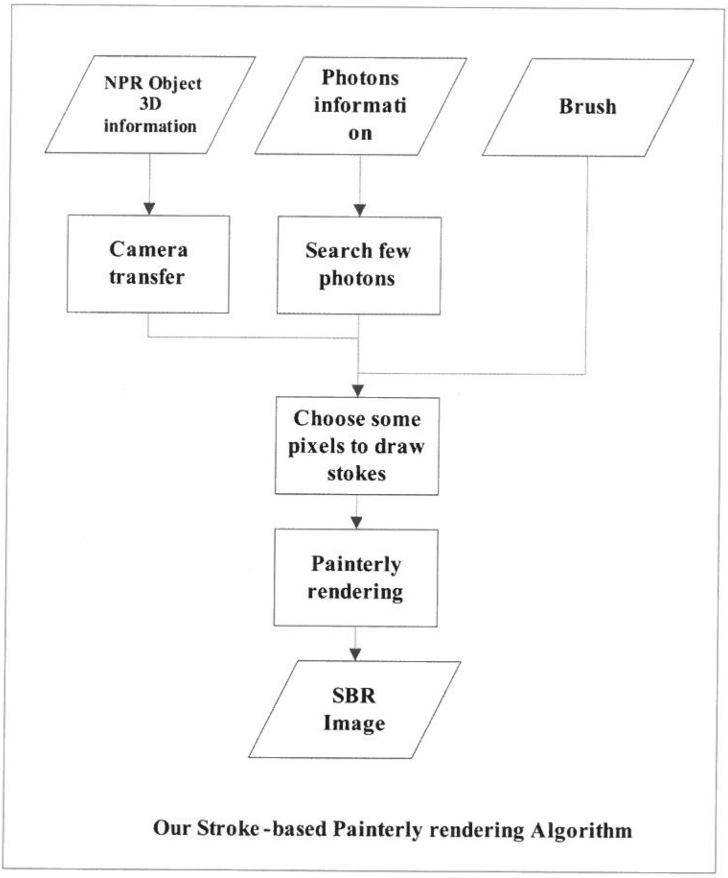

圖 **9**　我們的演算法其中的 **SBR** 部分。

3.3　PAPM 演算法之流程

我們選擇在光線路徑這個階段儲存資訊，並在視線路徑將擬真成像和非擬真成像做整合。(演算法流程圖如圖 10 所示)。利用視線路徑與場景的交點測試傳回可視點以及

物體的資訊，來判斷要進行擬真成像的演算法或是非擬真成像的演算法（Cast Ray Stage）。如果判定是擬真成像則進行照度計算(Estimate Radiance)，若否則進行 3D SBR 的演算法。依據這種作法，除了可以保持擬真成像與非擬真成像不同的風格之外。如果視點移動之後，由於第一階段的光線路徑與第二階段的視線路徑已經完全切割開，所以對於光線路徑不需要重新計算。所有擬真成像與非擬真成像所需要的資訊皆可以重複利用。

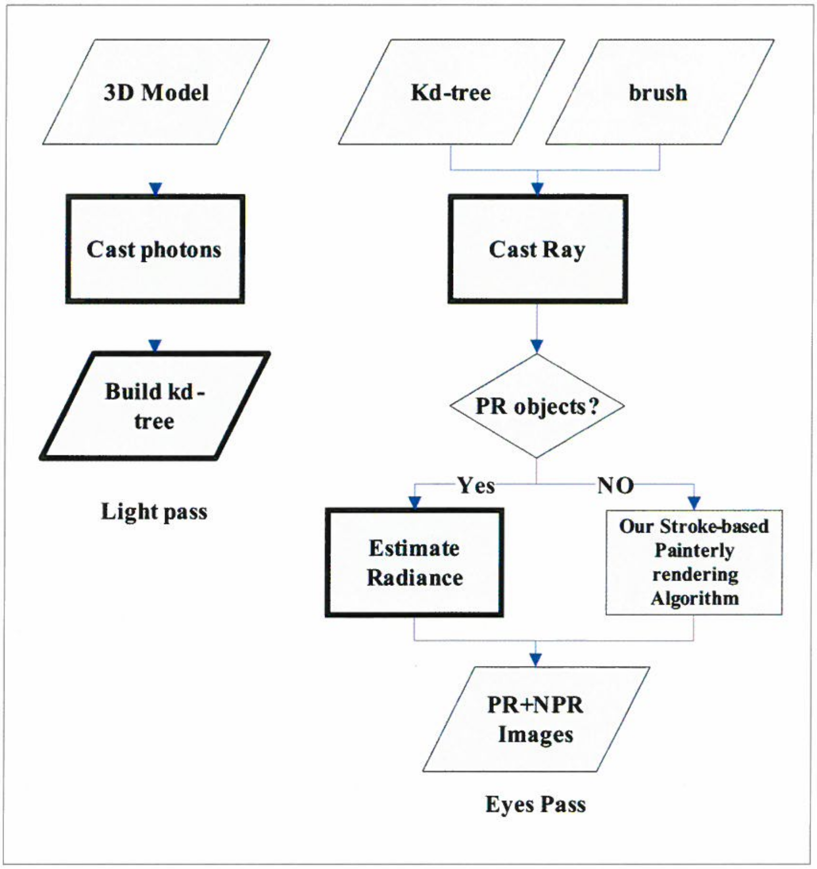

圖 **10** **PAPM** 演算法流程圖(粗線對應 **photon mapping**)

我們對於可視位置作 kd-tree 的搜尋。找出適當的光子或筆觸資訊。由於在蒙地卡羅光線追蹤法(Monte Carlo Ray Tracing)的架構基礎之下，場景必須進行交點測試。所以不論是光子映像或是 PAPM 演算法均得進行交點測試計算。但由於已經做了這些的交

點測試，所以我們將交點測試的結果再次利用，選定適合的點充當筆觸位置。這樣的好處是無須把所有的筆觸，都由遠至近全部畫一次。只需要畫出觀察者可以看到場景的部分。這樣可以節省很多不必要的時間。

PAPM 演算法與光子映像演算法的比較 (圖 11 與圖 12)：我們藉由兩種不同的成像演算法，所產生的結果。來比較一下不同之處。我們保留了擬真成像所產生的光影現象。來模擬真實的效果，但是一方面，我們讓強調的主題以非擬真成像的方式呈現(表現出 NPR 風格)。讓整個場景看起來更多樣化。

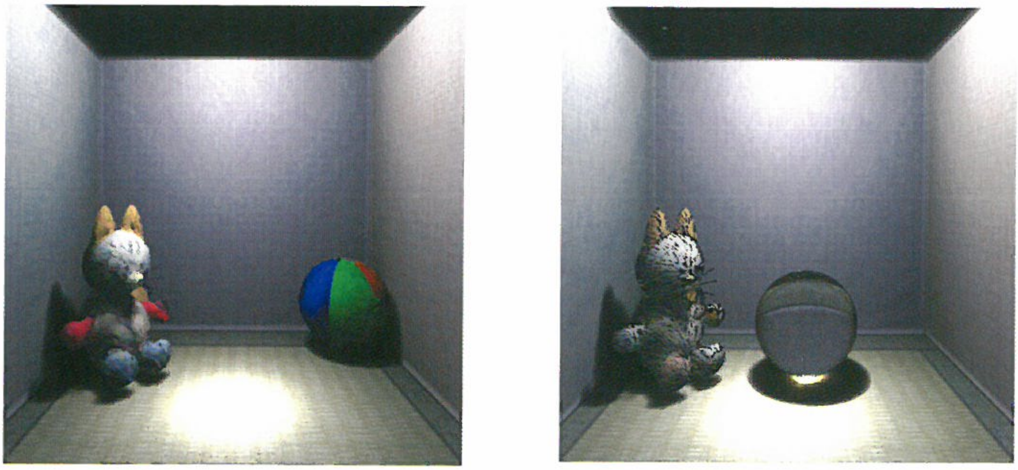

圖 **11**　**hybrid** ： 保留光影效果，並使狐狸玩偶以非擬真成像效果呈現出來

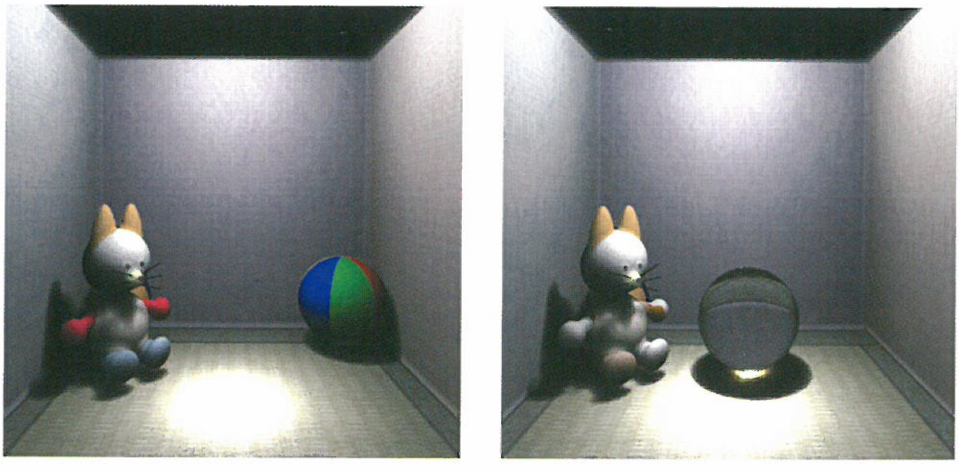

圖 **12**　擬真成像： 光藉由場景中的玻璃球產生聚光的現象。

四、執行結果

4.1 兩個場景的測試

我們使用 Pentium 4 2.8GHz 的 CPU，256MB 的記憶體作爲程式測試的環境，使用 Borland C++ Builder 開發程式，並準備了兩個場景，初始影像大小爲 512x512。模型 1 複雜度爲 5622polygon 與 1 個 sphere，模型 2 模型複雜度爲 12762 個 polygon。場景的光源位置設在天花板中央(3D 場景正上方)，光源型態是點光源。

爲了顯示 3D 模型的特性，我們任意在場景中移動視角與視點位置。如圖 13 所示，我們先從場景的正前方正視場景。由於光子疏密不一分布於場景中，所以即使是點光源，可以讓物體的陰影依然柔和(soft shadow)。場景接近光源的部份很明顯比角落明亮。符合光線照度會與距離成反比的特性。玻璃球也產生聚光的現象。

圖 13 左圖爲模型 **1**，右圖爲模型 **2**。視點在正前方，點光源在模型中央置頂。

接著，我們把視點分別轉向左右(如圖 14 所示)。利用改變筆觸的疏密，大小，方向與顏色，搭配視點的轉移。可以運算出不同的手繪風格。

圖 **14**　左圖爲模型 **1**，右圖爲模型 **2**。視點在正前方，上圖視角－ **45°**、下圖視角**+45°**。

最後，我們將圖 14 中兩個模型各別朝著視角方向將視點拉近至NPR物件附近，貼近觀察該物體(如圖 15 所示)。再次搭配改變筆觸的疏密，大小，方向與顏色。由於貼近觀察，可以清楚察覺細部的變化。包括光線的明暗，物體的陰影。可以觀察筆觸因應了光子照度的大小，來調整顏色的深淺。以營造出光線對物體造成的層次感與立體感。

圖 **15**　左圖爲模型 **1**，右圖爲模型 **2**。視點在正前方，上圖視角－**45°**、下圖視角**+45°**。視點貼近 **NPR** 物件。

4.2 細節的討論

有了筆觸的位置、大小、顏色與方向，我們雖然可以繪製非擬真成像的部份。但是有些細節可以加強成像的效果。接下來我們就要探討在3D模型之下，繪製非擬真成像所需注意的四個議題 ：

(1)筆觸長度的變異性
(2)筆觸方向的一致性
(3)筆觸大小的調整
(4)直接照度與全域照度的差異

(1)筆觸長度的變異性

在非擬真成像繪製過程之中，應該避免不同顏色的區塊，在筆觸延伸過長中造成影像模糊。在筆觸移動的過程之中，我們應該觀察光子能量的變化程度，來決定適合的筆觸長度。當筆觸延伸至照度變化量過大的時候，我們就該停止筆觸的延伸，如此，可以避免筆觸過長，導致影像模糊。圖16所示，A點爲筆觸的出發點。筆觸在往兩端移動的過程中，隨時收集光子的資訊以偵測能量的變化。移動的過程中收集的資訊將與A點比較，一旦發現彼此差異過大，如B、C兩點，便停止筆觸的移動。

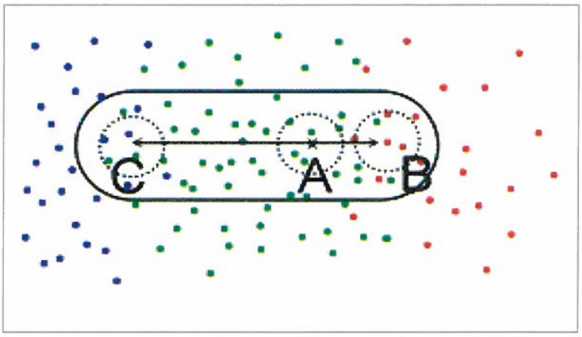

圖16 **B**、**C**兩處收集的光子與筆觸**A**差距過大即停止筆觸的延伸。

圖17與圖18這兩張圖片是調整不同界限値的兩種極端結果。我們建議筆觸的長度應該隨著光子的照度之間的變化來做適度的調整。我們的建議是可以預設一個照度差異的門檻値爲8%~10%，一旦大於這個門檻値便停止筆觸的延伸。由圖17、16我們去做筆觸長度的統計。預設筆觸長度最長爲40個 Pixel，筆觸總數爲183。藉由表2、表3

可以發現，若不依據光子照度變化產生的筆觸如表 2 所示，筆觸長度 40 的共有 144 個，十分接近全圖總數 183。而依據光子照度變化產生的筆觸如表 3 所示，筆觸長度 40 的只有 36 個，其餘筆觸均落於不同範圍的長度。而由肉眼觀察也可以發現，圖 17 造成邊界模糊不清，在圖 18 沒有這個現象的產生。

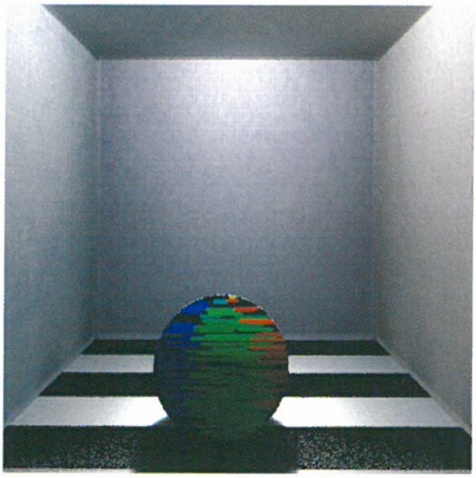

圖 **17** 筆觸移動的過程不參考能量變化。

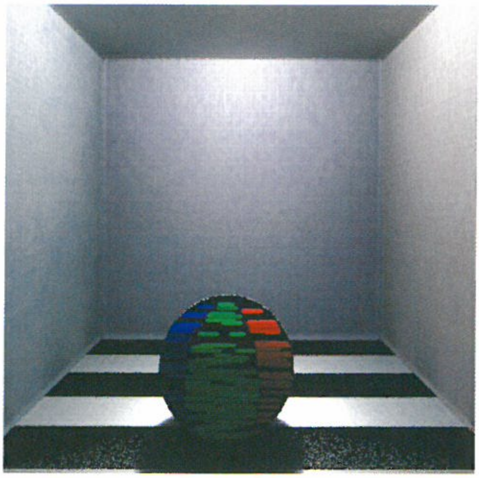

圖 **18** 筆觸移動的過程容許較小的能量變化(門檻值爲 **8%**)。

表 **2** 爲圖 **17** 的筆觸長度統計

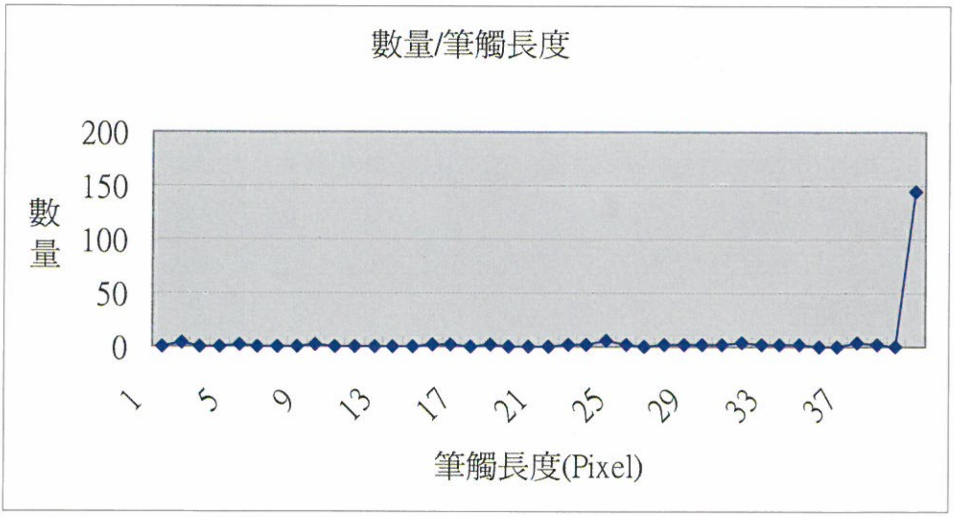

表 **3**　爲圖 **18** 的筆觸長度統計

(2)筆觸方向的一致性

在 3D 場景之中，表達手繪風格需要考慮到一致性(coherence)的問題。也就是筆觸的方向，應該與視點的移動，保持前後一致的合理方向。其作法是紀錄視點移動前，物體法向量與筆觸的關係。則一旦視點轉變之後，仍須藉此保持的筆觸方向。如圖 19~21 所示，其中 19 是原本的影像，圖 20 是視角改變之後，正確的筆畫方向，而圖 21 是錯誤的結果。因此筆觸必須考慮到物體的幾何性質以及觀察者的視點方向。我們透過光子的照度當成筆觸的顏色，視點與物體的交點與距離，代表筆觸位置與筆觸大小。搭配這不同筆觸的形狀，就可以呈現不同的畫風。如此一來當我們想要在視點有所改變的時候，便可以輕易得到另一張不同的影像。當然動畫就不會有影格與影格與之間不協調的狀況發生。

(3)筆觸大小的調整

圖 22 說明在 3D 場景之中，任何一個位置都可以運算出與視點的距離。爲了展現出遠近的效果，我們可以配合著物體與視點的距離來調整筆觸的大小。

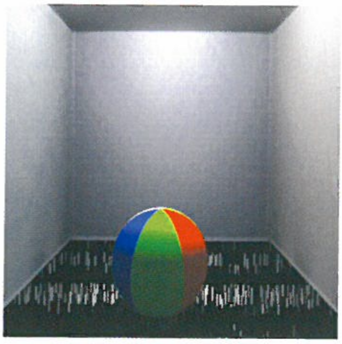

圖 19　地板底下的筆觸方向朝向房間的南方

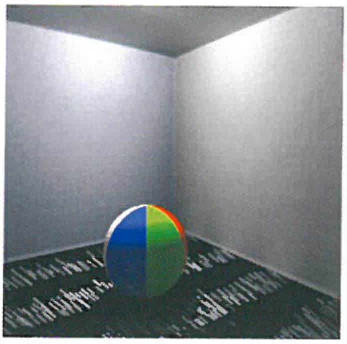

圖 20　視點移動過後，地板底下的筆觸方向依舊朝向房間的南方

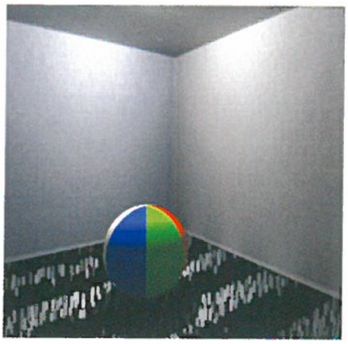

圖 21　視點移動過後，地板底下的筆觸方向與原本筆觸方向不一致

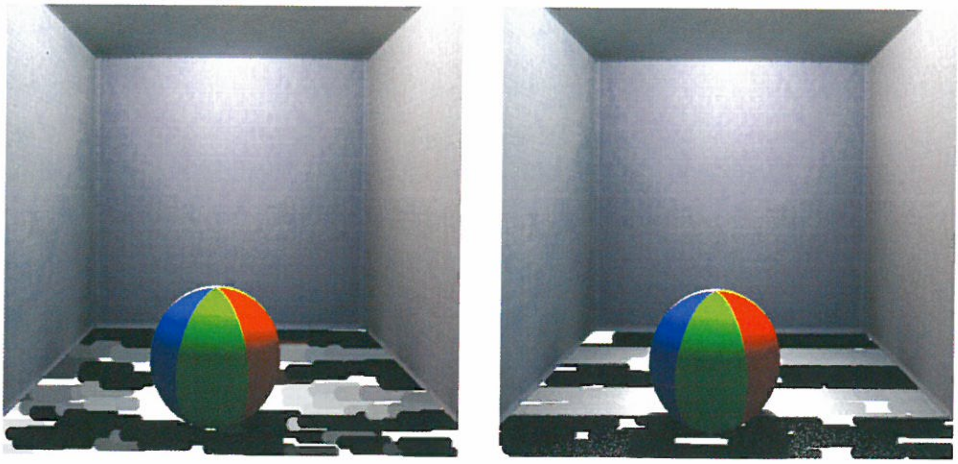

圖 22　隨著距離適度調整筆觸大小

(4)直接照度與全域照度對非擬真成像所造成的影響

所謂的直接照度就是只考慮光源直射於物體上面的能量，而全域照度不僅考慮直接照度的部份，同時也考慮物體和物體之間光線能量的交互影響。擬真成像在計算直接照度與全域照度成像所需的時間差距是很大的，所以我們想了解到底有沒有必要花很多時間來做全域照度演算法以求達到更好的成像效果？這個答案可以由圖 23 的影像得到答

案。因爲物體沒有受到直接照度的部份以至於沒有光子的資訊，所以無法提供充足的資訊以做非擬真成像物件的描繪。這樣會照成某些部份無法產生筆觸。有鑑於此，我們認爲進行全域照度的演算法才能完整呈現非擬真成像的風貌。

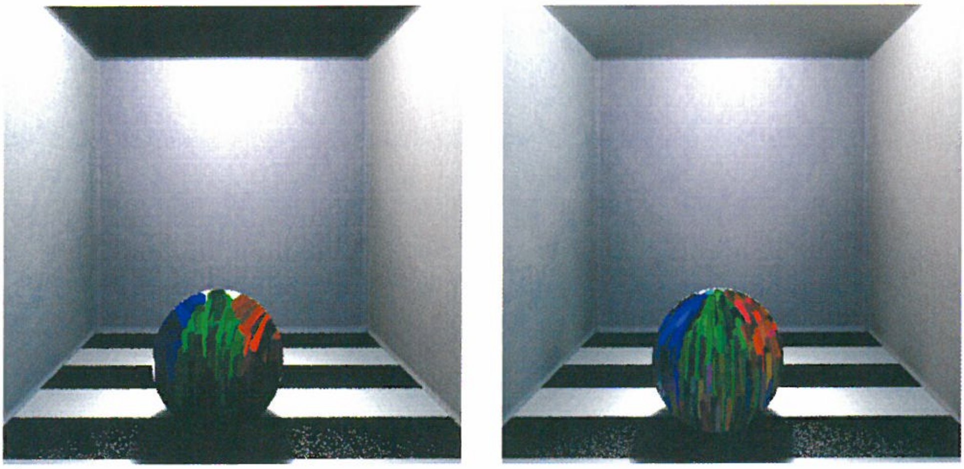

圖 **23** 左圖爲直接照度，無法提供球底部產生描繪非擬真成像所需的資訊。右圖爲全域照度，球部底端有資訊可提供描繪非擬真成像做運算。

五、結 論

在 3D 場景中同時呈現擬真與非擬真的圖像是一個新的問題。據此，我們提出一個嶄新的擬真與非擬真混合成像演算法，簡稱 PAPM 演算法。我們也在個人電腦平台上實作出一套成像系統。我們測試發現 PAPM 演算法可以有效的同時產生一張具有擬真與非擬真效果的圖像。就我們所知，文獻上尚未發現有其他演算法可以解決擬真與非擬真的圖像同時成圖的問題。

PAPM 也使用一些技巧，來在細部中加強成像的品質。這些技巧包括：利用 3D 模型中的各種資訊，使得筆觸的長度可以作彈性調整，此可避免不同顏色的筆觸互相干擾造成邊界模糊的現象。因爲 3D 模型可以移動視點， 所以繪製在 NPR 的筆觸方向必須一致。讓筆觸隨著視點的移動作合理的變化。筆觸的大小也可以隨著物件與觀察者距離不同而改變。

PAPM 演算法的優點是不需要藉助任何前製作或是後製作。就可以具備 PR 與 NPR

兩種不同風格的影像。而且實作簡單，不會增加太多的時間即可達成目的。因爲PAPM光線路徑階段屬於與視點無關(View independent)的演算法。所以在視點改變之後，可以重複利用，僅需重新計算視線路徑階段即可。

PAPM演算法的瓶頸是繼承了PR的特性，需要長時間來做光線與物體的交點測試，導致成圖時間過長。因此，未來工作可以注重在效能的改進。此外，我們可以更注重不同的繪製方法以及使用多層式(multi-layer)的筆觸，以增加細膩的程度。

六、參考文獻

(1) Henrik Wann Jensen, "A Practical Guide to Global Illumination using Photon Mapping," SIGGRAPH'2002 Course 43, San Antonio, July 2002.

(2) B. J. Meier, "Painterly Rendering for Animation," in Proceedings of SIGGRAPH '96, pp. 477-484, 1996.

(3) G. Ward and P. Heckbert, "Irradiance gradients," Third Eurographics Workshop on Rendering, pp. 85-98, Eurographics, 1992.

(4) P. Shirley, "A Ray Tracing Method for Illumination Calculation in Diffuse-Specular Scenes," Proceedings of Graphics Interface '90, pp. 205-212, 1990.

(5) J. Arvo, "Backward ray Tracing," Developments in ray tracing, SIGGRAPH 96 seminar notes. ACM, August 1986.

(6) J.L. Bentley, "Multidimensional Binary Search Trees Used for Associative Searching," Communication of ACM 18(9), pp. 509-517(1975).

(7) P. Litwinowicz, "Processing Images and Video for an Impressionist Effect," Proc. Siggraph 97, ACM Press, pp. 407-414, 1997.

(8) B.W. Silverman. Density Estimation for Data Analysis, Chapman & Hail, 1986.

(9) A. Hertzmann, "Painterly Rendering with Curved Brush Strokes of Multiple Sizes," Proc. Siggraph 98, ACM Press, pp. 453-460, 1998.

(10) A. Hertzmann, "Fast Paint Texture," Proc. 2nd Ann. Symp. Non-Photorealistic Animation and Rendering (NPAR 2002), ACM Press, pp. 91-96, 161, 2002.

(11) P.E. Haeberli, "Paint by Numbers: Abstract Image Representations," Computer Graphics (Proc. Siggraph 90), vol.24, ACM Press, pp. 207-214, 1990.

(12) A. Hausner, "Simulating Decorative Mosaic," Proc. Siggraph 2001, ACM Press, pp.

573-578, 2001.

(13) A. Hertzmann, "Paint by Relaxation," Computer Graphics Int'l 2001, IEEE CS Press, pp. 47-54, 2001.

(14) G. Winkenbach and D.H. Salesin, "Computer-Generated Pen-And-Ink Illustration," Proc. Siggraph 94, ACM Press, pp. 91-100, 1994.

(15) K. Myszkowski, "Lighting Reconstruction Using Fast and Adaptive Density Estimation Techniques," Rendering Techniques '97, pp. 321-326. Springer Verlag, 1997.

(16) V. Volevich, "Perceptually- Informed Progressive Global Illumination Solution," Technical Report 99-1-002, University of Aizu, Japan, 1999.

(17) A. Lu, C. J. Morris, J. Taylor, D. S. Ebert, C. Hansen, P. Rheingans, and M. Hartner, "Illustrative interactive stipple rendering," IEEE Transactions on Visualization and Computer Graphics, vol. 9, no.2, pp. 127-138, 2003.

(18) O. Deussen and T. Strothotte, "Computer-generated pen-and-ink illustration of trees," in SIGGRAPH '00. ACM Press/Addison-Wesley Publishing Co., pp. 13-18, 2000

(19) E. Praun, H. Hoppe, M. Webb, and A. Finkelstein, "Real-time hatching," in SIGGRAPH '01. ACM Press, p. 581. 2001,

(20) A. Lake, C. Marshall, M. Harris, and M. Blackstein, "Stylized rendering techniques for scalable real-time 3d animation," in NPAR '00. ACM Press, pp. 13-20, 2000

(21) Ming-Te Chi, Tong-Yee Lee, "Stylized and Abstract Painterly Rendering System Using a Multi-Scale Segmented Sphere Hierarchy", IEEE Transactions on Visualization and Computer Graphics, 2005

received October 31, 2005
revised November 14, 2005
accepted November 28, 2005

PAPM: A Novel Algorithm for Photorealistic and Non-Photorealistic Hybrid Rendering

Chung-Ming Wang*　Meng-Tan Lee**
Department of Computer Science,
National Chung Hsing University,
Taichung 402, Taiwan, R.O.C

ABSTRACT

In this paper, we proposed a novel hybrid algorithm which includes Photorealistic Rendering and Non-Photorealistic Rendering simultaneously. We named this algorithm PAPM. As we known, there has no similar algorithm like PAPM to simulate Photorealistic Rendering (PR) and Non-Photorealistic Rendering (NPR) at the same three-dimensional scene. We adopt Photon Mapping (Jensen, 2002) as a foundation to develop PAPM, which is a two-pass Algorithm. It's including view-dependent pass (light pass) and view-independent pass (eyes pass). In light pass, we cast photons from light source. Those photons according as material of three-dimensional objects, to decide that photons be reflection or refraction. And those photons will stop on diffuse surfaces. We record those photons in multi-dimension binary search tree (KD-tree) for efficient search during eyes pass. First, in eyes pass, we cast several rays to view-plane from view point. Those rays and three-dimensional objects do point intersections. By the result of intersections, we can get the visible point and the property of this object. Secondary, if the properties of objects belong to PR, we search some photons near those visible points to estimate correct illumination. On the other hand, if the properties of objects belong to NPR, we use photons and three-dimensional information of those NPR objects to do stroke-base rendering (SBR) algorithm. According to our two-pass algorithm, we can show PR and NPR style in three-dimensional scene simultaneously.

We implement a rendering system by PAPM algorithm. And we use the PC to test. By those experimental results, that show the PAPM algorithm can really be reached our expected images which hybrid PR and NPR. Summarizing our paper, we propose a novel algorithm PAPM which no ones have presented on any scientific or technical literature. PAPM has three advantages: (1) Hybrid PR and NPR Rendering: It can produce a static image which includes both PR and NPR style in three-dimensional scene; (2) Nice NPR quality: We propose 3 skills, that can improve NPR quality in PAPM; (3) effective calculation: PAPM used two-pass rendering, so when view point change, we only need to calculate eyes pass because eyes pass is view-dependent. So our PAPM algorithm can be used in various kinds of view-dependent application, such as animation, etc.

Key words: photorealistic rendering, non -photorealistic rendering, global rendering, Photon mapping, stroke-based rendering.

Hazard Function Estimation for Series System with Exponentiated Weibull Components

Sy-Mien Chen*
Department of Mathematics
Graduate Institute of Applied Science and Engineering
Fu Jen Catholic University, Taipei, Taiwan, R.O.C.

Yu-Zen Dai
Department of Mathematics
Fu Jen Catholic University, Taipei, Taiwan, R.O.C.

Abstract

A three-parameter Exponentiated Weibull distribution $EW(\sigma, \alpha, \theta)$ has a bathtub shape hazard function if $\alpha > 1$ and $\alpha\theta < 1$. In this article, we propose a direct estimator and an indirect estimator of the (cumulative) hazard function of a series system by assuming that the independent components of the system are from such type of Exponentiated Weibull distributions. It is shown that the direct estimator is better than the indirect estimator in the sense of sample relative mean square error.

Key words：Cumulative Hazard Function; Maximum Likelihood Estimator.

1. INTRODUCTION

Hazard function is an important measure of quality in reliability studies. Fail to identify

---

*Corresponding author. Tel: +886-2-29052451
E-mail: srnchen@math.fju.edu.tw

high hazard function products or components could lead to a great loss. Diverse existing shapes of hazard function well describe the reliabilities of all kinds of products and provide solid grounds for decision making. See Lawless (1982), Lee and Max (1991), Meeker and Escobar (1998) and references therein for more details about hazard function.

It is interesting to note that the hazard function of an assembly product can be estimated by observations from the product directly or from the components indirectly. A practical question is which method of the two is better, and that will mainly our goal for this research. We consider a series system product which is composed by two independent components from exponentiated Weibull families. In section two, we did a brief review of such family. Then we propose a direct and an indirect estimator of the (cumulative) hazard function. In section 3, a simulation study is conducted to give an idea about the performances for both direct and indirect estimators. In section 4 we give some conclusions and suggestions.

2. Exponentiated Weibull Family

Mudholkar et. al. (1995) proposed the exponentiated Weibull distribtution to re-analyze the bus data which was discussed in Davis (1952). After comparing the performances of exponential distribution, Weibull distribution and exponentiated Weibull distribution, they found out that the exponentiated Weibull distribution can fit the data best. In practice, D.J. de Waal(1996) applied Exponentiated Weibull distribution on lifetime data. Per Botolf Maurseth(2001) did a similar study on copy right protection problem.

Let T be a random variable with probability density function

$$f(t;\sigma,\alpha,\theta)=\frac{\alpha\theta}{\sigma}\left[1-\exp\left(-\left(\frac{t}{\sigma}\right)^{\alpha}\right)\right]^{\theta-1}\exp\left(-\left(\frac{t}{\sigma}\right)^{\alpha}\right)\left(\frac{t}{\sigma}\right)^{\alpha-1},\ 0<t<\infty$$

where the scale parameter $\sigma>0$, shape parameters $\alpha>0$, $\theta>0$, then we say T follows an exponentiated Weibull distribution, which will be denoted by $EW(\sigma,\alpha,\theta)$. For $t>0$, the distribution function of T is $F_T(t;\alpha,\sigma,\theta)=1-\exp\left(-\left(\frac{t}{\sigma}\right)^{\alpha}\right)^{\theta}$, and the hazard function of T at time t is

$$h_T(t;\sigma,\alpha,\theta)=\frac{f_T(t)}{1-F_T(t)}=\frac{\alpha\theta\left[1-\exp\left(-\left(\frac{t}{\sigma}\right)^{\alpha}\right)\right]^{\theta-1}\exp\left(-\left(\frac{t}{\sigma}\right)^{\alpha}\right)\left(\frac{t}{\sigma}\right)^{\alpha-1}}{\sigma\left[1-\left(1-\exp\left(-\left(\frac{t}{\sigma}\right)^{\alpha}\right)\right)^{\theta}\right]}$$

. The shape of $h_T(t)$ can be classified as strictly increasing, strictly decreasing, bathtub, unimodel and constant by the boundary line $\alpha=1$ and curve $\alpha\theta=1$, see Mudholkar *et. a*l. (1995). The cumulative hazard function is

$$H_T(t;\sigma,\alpha,\theta)=\int_0^t h_T(u)du=-\ln(1-F_T(t))=-\ln\left\{1-\left(1-\exp\left(-\left(\frac{t}{\sigma}\right)^{\alpha}\right)\right)^{\theta}\right\}.$$

To abuse the notation, let X and Y be both the independent components and the life time of such two independent components from $EW(\sigma_1,\alpha_1,\theta_1)$ and $EW(\sigma_2,\alpha_2,\theta_2)$, respectively. Similarly, let Z denote both the system and the life time of the series system which is composed by X and Y, then $Z=\min\{X,Y\}$. Let $\pi=(\sigma_1,\alpha_1,\theta_1,\sigma_2,\alpha_2,\theta_2)$, $\pi_1=(\sigma_1,\alpha_1,\theta_1)$, $\pi_2=(\sigma_2,\alpha_2,\theta_2)$. Then for $t>0$, the density function and the cumulative distribution function of Z are $f_Z(t;\pi)=f_X(t;\pi_1)(1-F_Y(t;\pi_2))+f_Y(t;\pi_2)(1-F_X(t;\pi_1))$, and $F_Z(t;\pi)=F_X(t;\pi_1)\ +\ F_Y(t;\pi)=F_X(t;\pi_2)(1-F_X(t;\pi_1))$ respectively. The hazard function of Z is $h_Z(t;\pi)=h_X(t;\pi_1)+\ h_Y(t;\pi_2)=\frac{f_X(t;\pi_1)}{1-F_Y(t;\pi_2)}+\frac{f_Y(t;\pi_2)}{1-F_X(t;\pi_1)}$. The cumulative hazard function is $H_Z(t;\pi)=H_X(t;\pi_1)+\ H_Y(t;\pi_2)$.

In general, h_Z and H_Z are unknown, and it is interesting to note that both the hazard function and the cumulative hazard function of an assembly product can be estimated by observations from the product directly or from the components indirectly. A practical question is which method is better. Let

$$\hat{h}_Z^D(t;\tilde{\pi}) = \frac{\tilde{\alpha}_1\tilde{\theta}_1\left[1-e^{\left(-\left(\frac{t}{\tilde{\sigma}_1}\right)^{\tilde{\alpha}_1}\right)}\right]^{\tilde{\theta}_1-1} e^{\left(-\left(\frac{t}{\tilde{\sigma}_1}\right)^{\tilde{\alpha}_1}\right)}\left(\frac{t}{\tilde{\sigma}_1}\right)^{\tilde{\alpha}_1-1}}{\tilde{\sigma}_1\left[1-\left[1-e^{\left(-\left(\frac{t}{\tilde{\sigma}_1}\right)^{\tilde{\alpha}_1}\right)}\right]^{\tilde{\theta}_1}\right]} + \frac{\tilde{\alpha}_2\tilde{\theta}_2\left[1-e^{\left(-\left(\frac{t}{\tilde{\sigma}_2}\right)^{\tilde{\alpha}_2}\right)}\right]^{\tilde{\theta}_2-1} e^{\left(-\left(\frac{t}{\tilde{\sigma}_2}\right)^{\tilde{\alpha}_2}\right)}\left(\frac{t}{\tilde{\sigma}_2}\right)^{\tilde{\alpha}_2-1}}{\tilde{\sigma}_2\left[1-\left[1-e^{\left(-\left(\frac{t}{\tilde{\sigma}_2}\right)^{\tilde{\alpha}_2}\right)}\right]^{\tilde{\theta}_2}\right]},$$

$$\hat{H}_Z^D(t;\tilde{\pi}) = -Ln\left(1-\left(1-e^{-\left(\frac{t}{\tilde{\sigma}_1}\right)^{\tilde{\alpha}_1}}\right)^{\tilde{\theta}_1} - \left(1-e^{-\left(\frac{t}{\tilde{\sigma}_2}\right)^{\tilde{\alpha}_2}}\right)^{\tilde{\theta}_2}\left(1-\left(1-e^{-\left(\frac{t}{\tilde{\sigma}_1}\right)^{\tilde{\alpha}_1}}\right)^{\tilde{\theta}_1}\right)\right),$$

where $\tilde{\pi}=(\tilde{\sigma}_1,\tilde{\alpha}_1,\tilde{\theta}_1,\tilde{\sigma}_2,\tilde{\alpha}_2,\tilde{\theta}_2)$ is the maximum likelihood estimator of $\pi=(\sigma_1,\alpha_1,\theta_1,\sigma_2,\alpha_2,\theta_2)$ which is derived directly from the system life Z. Then $\hat{h}_Z^D(t;\tilde{\pi})$ and $\hat{H}_Z^D(t;\tilde{\pi})$ are the direct estimator of $h_Z(t;\pi)$ and $H_Z(t;\pi)$, respectively. Let

$$\hat{h}_Z^I(t;\hat{\pi}) = \frac{\hat{\alpha}_1\hat{\theta}_1\left[1-e^{\left(-\left(\frac{t}{\hat{\sigma}_1}\right)^{\hat{\alpha}_1}\right)}\right]^{\hat{\theta}_1-1} e^{\left(-\left(\frac{t}{\hat{\sigma}_1}\right)^{\hat{\alpha}_1}\right)}\left(\frac{t}{\hat{\sigma}_1}\right)^{\hat{\alpha}_1-1}}{\hat{\sigma}_1\left[1-\left[1-e^{\left(-\left(\frac{t}{\hat{\sigma}_1}\right)^{\hat{\alpha}_1}\right)}\right]^{\hat{\theta}_1}\right]} + \frac{\hat{\alpha}_2\hat{\theta}_2\left[1-e^{\left(-\left(\frac{t}{\hat{\sigma}_2}\right)^{\hat{\alpha}_2}\right)}\right]^{\hat{\theta}_2-1} e^{\left(-\left(\frac{t}{\hat{\sigma}_2}\right)^{\hat{\alpha}_2}\right)}\left(\frac{t}{\hat{\sigma}_2}\right)^{\hat{\alpha}_2-1}}{\hat{\sigma}_2\left[1-\left[1-e^{\left(-\left(\frac{t}{\hat{\sigma}_2}\right)^{\hat{\alpha}_2}\right)}\right]^{\hat{\theta}_2}\right]},$$

$$\hat{H}^{I}_{Z}(t;\hat{\pi}) = -Ln\left(1-\left(1-e^{-\left(\frac{t}{\hat{\sigma}_1}\right)^{\hat{\alpha}_1}}\right)^{\hat{\theta}_1}\right) - Ln\left(1-\left(1-e^{-\left(\frac{t}{\hat{\sigma}_2}\right)^{\hat{\alpha}_2}}\right)^{\hat{\theta}_2}\right) = \hat{H}^{I}_{X}(t;\hat{\pi}_1) + \hat{H}^{I}_{Y}(t;\hat{\pi}_2),$$

where $\hat{\pi}_i = (\hat{\sigma}_i, \hat{\alpha}_i, \hat{\theta}_1)$ be the estimator of $\pi_i = (\sigma_i, \alpha_i, \theta_i)$, $i=1, 2$, which can is derived from the two components lives X and Y respectively. Then $\hat{h}^{I}_{Z}(t;\hat{\pi})$ and $\hat{H}^{I}_{Z}(t;\hat{\pi})$ are the indirect estimator of $h_Z(t;\pi)$ and $H_Z(t;\pi)$ respectively. By the invariance property of maximum likelihood estimator, both $\hat{h}^{I}_{Z}(t;\hat{\pi})$ and $\hat{h}^{D}_{Z}(t;\hat{\pi})$ are maximum likelihood estimators of $h_Z(t;\pi)$, $\hat{H}^{I}_{Z}(t;\hat{\pi})$ and $\hat{H}^{D}_{Z}(t;\hat{\pi})$ are maximum likelihood estimators of$hH_Z(t;\pi)$, and they are all asymptotically unbiased normally distributed for the corresponding parameter. (See [4])

3. Simulation Study

3.1 Parameter Setting

Mathematica ,Visual Fortran and Microsoft Excel are the tools we use. In this simulation, we consider two types of sampling, call them type I and type II sampling, see Fig I(a)(b) for definition. The sample size we use are 100, 200, 300, 400, 500, 600 due to the large sample property of maximum likelihood estimator. For simplicity, in this research we consider the case when $\sigma=1$. i.e. Let X and Y be the lifetime of the two independent components from $EW(1, \alpha_1, \theta_1)$ and $EW(1, \alpha_2, \theta_2)$, respectively. Also, we redefine the following notations: $\pi = (\alpha_1, \theta_1, \alpha_2, \theta_2)$, $\pi_1 = (\alpha_1, \theta_1)$, and $\pi_2 = (\alpha_2, \theta_2)$. There are 19 models, i.e. 19 combinations of parameters, we considered, see Table I.

parameter model	α_1	θ_1	α_2	θ_2
1	1.5	0.3	1.4	0.4
2	1.8	0.2	1.7	0.4
3	2	0.2	2	0.2
4			3	0.2
5			3	0.3
6		0.3	2	0.3
7			3	0.2
8			3	0.3
9			4	0.2
10		0.4	2	0.4
11			3	0.2
12			3	0.3
13			4	0.2
14	3	0.2	3	0.2
15			3	0.3
16			4	0,.2
17		0.3	3	0.3
18			4	0.2
19	4	0.2	4	0.2

Table I: Models considered in the simulation study

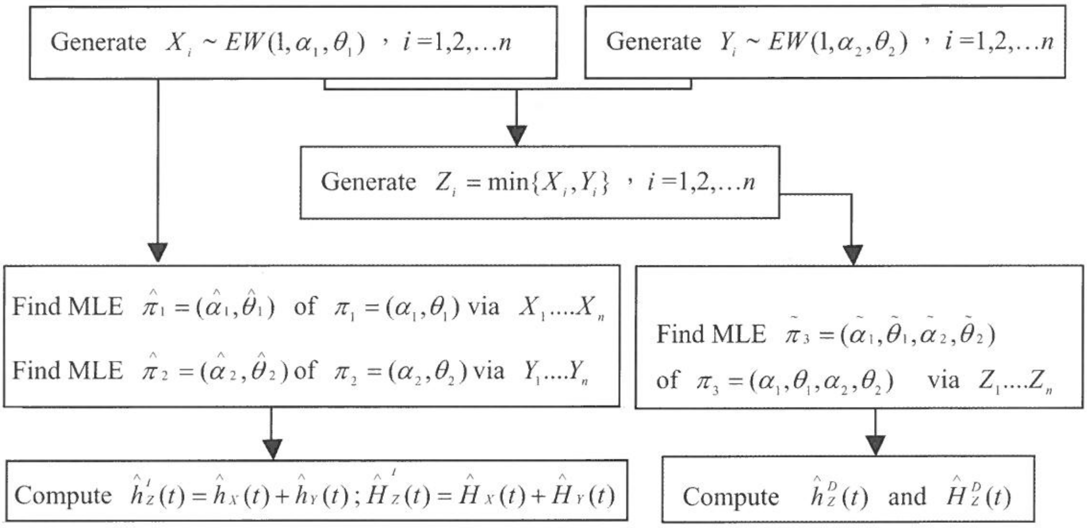

Fig 1(a): Type I sampling

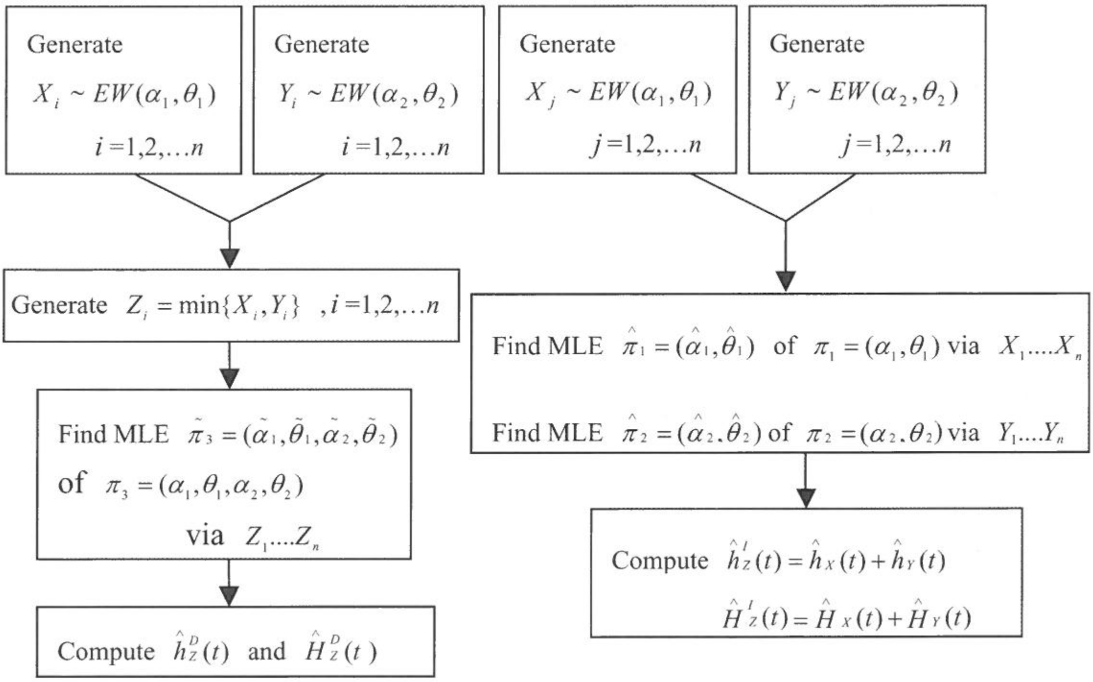

Fig 1(b): Type II sampling

For iteration i, we get an estimator of the hazard function and cumulative hazard function, namely $\hat{h}_i^D, \hat{H}_i^D, \hat{h}_i^I, \hat{H}_i^I$. We use the Sample Relatively Mean Square Error (SRMSE) for the comparison between the performance of direct estimator and the indirect estimator, where

$$SRMSE\ (\ \hat{h}_Z^I(t;\hat{\pi})\ ) = \frac{\sum_{i=1}^{m}[\hat{h}_i^I(t;\hat{\pi}) - h(t;\pi)]^2 \ / \ m}{h(t;\pi)},$$

$$SRMSE\ (\ \hat{h}_Z^D(t;\pi)\ ) = \frac{\sum_{i=1}^{m}[\hat{h}_i^D(t;\tilde{\pi}) - h(t;\pi)]^2 \ / \ m}{h(t;\pi)}$$

$$SRMSE\ (\ \hat{H}_Z^I(t;\hat{\pi})\ ) = \frac{\sum_{i=1}^{m}[\hat{H}_i^I(t;\hat{\pi}) - H(t;\hat{\pi})]^2 \ / \ m}{H(t;\pi)},$$

$$SRMSE\ (\ \hat{H}_Z^D(t;\tilde{\pi})\ ) = \frac{\sum_{i=1}^{m}[\hat{H}_i^D(t;\tilde{\pi}) - H(t;\pi)]^2 \ / \ m}{H(t;\pi)},$$

m is the number of iteration, $t>0$.

3.2 Simulation Results

SRMSE $(\hat{H}_Z^I(t;\hat{\pi}))$ and *SRMSE* $(\hat{H}_Z^D(t;\tilde{\pi}))$ for all the 19 models given in Table I are all less than 1 when the sample size is within 600. Among those, seven of them, model 1, 2, 3, 4, 6, 7, 10, have *SRMSE* $(\hat{h}_Z^I(t;\hat{\pi})) \leq 1$ under both sampling type I and II.

Fig 2 is the hazard functions for model 1, 2, 3, 4, 6, 7, 10. As we can see that there are four different categories. Curves which lie in the same category almost overlapped. But for models in different category the curves are quite different, which indicates that the parameter α does control the speed of increasing.

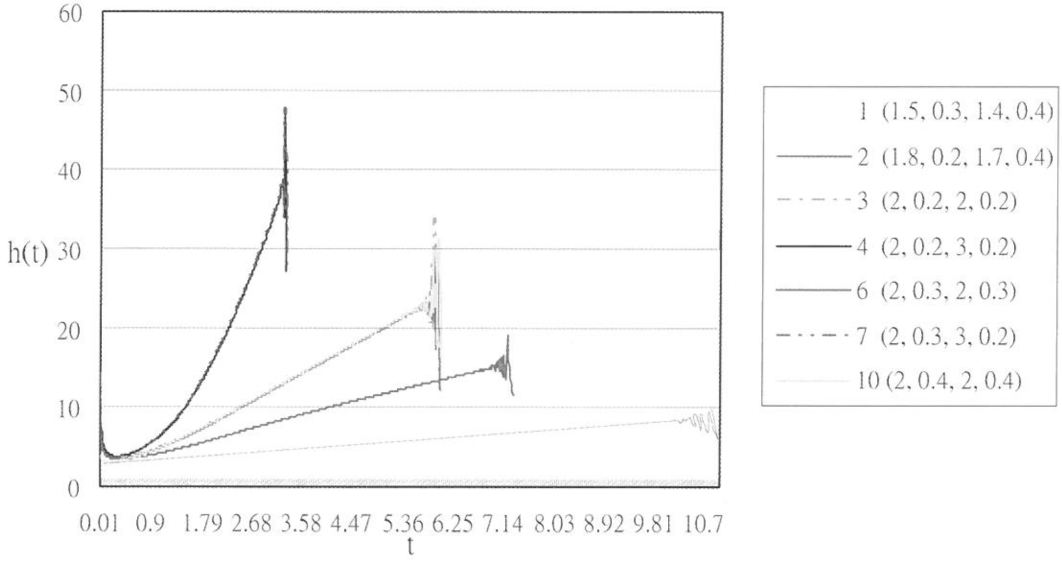

Fig 2: curves of the hazard functions of 7 models.

Table II(a)-(d) lists the value SRMSE of the direct and indirect estimators for hazard function and cumulative hazard function under type I and type II sampling. The values of t used are those stopping points indicate in Fig II. From the Table, the value $SRMSE\ (\hat{h}_Z^D(t))$ of model 2 (i.e. when $(\alpha_1, \theta_1, \alpha_2, \theta_2) = (1.8, 0.2, 1.7, 0.4)$) is larger than $SRMSE\ (\hat{h}_Z^D(t))$ of other models. One reason may be because of the value $\alpha_1\theta_1$ in this model is smaller than the $\alpha_1\theta_1$ in other models, and the difference between $\alpha_1\theta_1$ and $\alpha_2\theta_2$ are large. The same result is shown in model 5 also, see Table III.

model	$(\alpha_1, \theta_1, \alpha_2, \theta_2)$	Sample size	$SRMSE\ (\hat{h}_Z^I(t))$	$SRMSE\ (\hat{h}_Z^D(t))$
1	(1.5, 0.3, 1.4, 0.4)	200	0.589711	0.024811
2	(1.8, 0.2, 1.7, 0.4)	200	0.506467	0.079317
3	(2, 0.2, 2, 0.2)	200	0.868775	0.008249
4	(2, 0.2, 3, 0.3)	600	0.819698	0.046327
6	(2, 0.3, 2, 0.3)	400	0.813838	0.005561
7	(2, 0.3, 3, 0.2)	600	0.780864	0.005145
10	(2, 0.4, 2, 0.4)	400	0.678564	0.012732

Table II(a)： SRMSE of estimators for hazard function under type I sampling.

model	$(\alpha_1, \theta_1, \alpha_2, \theta_2)$	Sample size	$SRMSE\ (\hat{h}^{I}_{Z}(t))$	$SRMSE\ (\hat{h}^{D}_{Z}(t))$
1	(1.5, 0.3, 1.4, 0.4)	200	0.827301	0.030151
2	(1.8, 0.2, 1.7, 0.4)	200	0.588074	0.103164
3	(2, 0.2, 2, 0.2)	200	0.827794	0.004189
4	(2, 0.2, 3, 0.3)	100	0.887583	0.025727
6	(2, 0.3, 2, 0.3)	200	0.779973	0.002324
7	(2, 0.3, 3, 0.2)	300	0.973605	0.001726
10	(2, 0.4, 2, 0.4)	200	0.930155	0.014694

Table II(b)： SRMSE of estimators for cumulative hazard function under type I sampling.

model	$(\alpha_1, \theta_1, \alpha_2, \theta_2)$	Sample size	$SRMSE\ (\hat{h}^{I}_{Z}(t))$	$SRMSE\ (\hat{h}^{D}_{Z}(t))$
1	(1.5, 0.3, 1.4, 0.4)	200	0.519868	0.152430
2	(1.8, 0.2, 1.7, 0.4)	200	0.708247	0.14243
3	(2, 0.2, 2, 0.2)	200	0.901402	0.005126
4	(2, 0.2, 3, 0.3)	500	0.853446	0.020443
6	(2, 0.3, 2, 0.3)	400	0.947583	0.005918
7	(2, 0.3, 3, 0.2)	500	0.789127	0.002202
10	(2, 0.4, 2, 0.4)	400	0.783692	0.013447

Table II(c)： SRMSE of estimators for hazard function under type II sampling.

model	$(\alpha_1, \theta_1, \alpha_2, \theta_2)$	Sample size	$SRMSE\ (\hat{h}^{I}_{Z}(t))$	$SRMSE\ (\hat{h}^{D}_{Z}(t))$
1	(1.5, 0.3, 1.4, 0.4)	100	0.9478836	0.028014
2	(1.8, 0.2, 1.7, 0.4)	200	0.940906	0.193674
3	(2, 0.2, 2, 0.2)	100	0.965047	0.00174
4	(2, 0.2, 3, 0.3)	100	0.613368	0.044576
6	(2, 0.3, 2, 0.3)	400	0.818241	0.003863
7	(2, 0.3, 3, 0.2)	200	0.718457	0.000609
10	(2, 0.4, 2, 0.4)	200	0.864922	0.016406

Table II(d)： SRMSE of estimators for cumulative hazard function under type II sampling.

Fig 3 is the hazard functions for model 9、13、16、18、19 and model 5、8、11、12、14、15、17. As we can see that there are two different categories. Curves which lie in the same category almost overlapped. But for models in different catalogue the curves are quite different which indicates that the parameter α does control the speed of increasing.

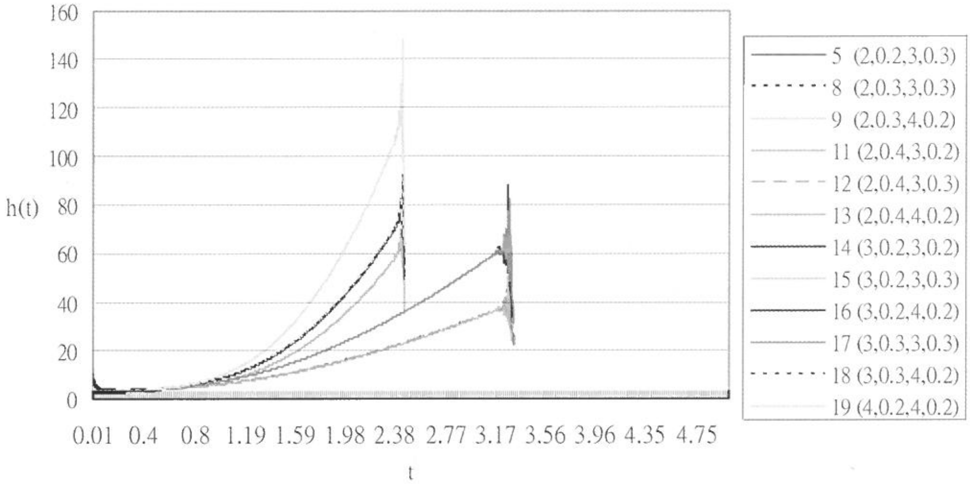

Fig 3: urves of the hazard functions of 12 models.

model	$(\alpha_1, \theta_1, \alpha_2, \theta_2)$	Sample size	$SRMSE\ (\hat{h}_Z^I(t))$	$SRMSE\ (\hat{h}_Z^D(t))$
5	(2, 0.2, 3, 0.3)	600	1.042445	0.496156
8	(2, 0.3, 3, 0.3)	600	1.304742	0.010855
9	(2, 0.3, 4, 0.2)	600	1.601661	0.017871
11	(2, 0.4, 3, 0.2)	500	1.113977	0.003249
12	(2, 0.4, 3, 0.3)	600	1.35691	0.008137
13	(2, 0.4, 4, 0.2)	600	1.670947	0.007133
14	(3, 0.2, 3, 0.2)	600	1.124335	0.011689
15	(3, 0.2, 3, 0.3)	600	1.088046	0.029585
16	(3, 0.2, 4, 0.2)	600	1.288572	0.024488
17	(3, 0.3, 3, 0.3)	600	1.546624	0.009105
18	(3, 0.3, 4, 0.2)	600	1.308411	0.003252
19	(4, 0.2, 4, 0.2)	600	1.912836	0.010710

Table III(a)： SRMSE of estimators of hazard function under type I sampling

model	$(\alpha_1, \theta_1, \alpha_2, \theta_2)$	Sample size	$SRMSE\ (\hat{h}_Z^I(t))$	$SRMSE\ (\hat{h}_Z^D(t))$
5	(2, 0.2, 3, 0.3)	100	0.8133	0.321525
8	(2, 0.3, 3, 0.3)	400	0.759456	0.006723
9	(2, 0.3, 4, 0.2)	100	0.682675	0.12883
11	(2, 0.4, 3, 0.2)	100	0.838708	0.002128
12	(2, 0.4, 3, 0.3)	100	0.838708	0.002128
13	(2, 0.4, 4, 0.2)	200	0.850519	0.007381
14	(3, 0.2, 3, 0.2)	200	0.784646	0.001263
15	(3, 0.2, 3, 0.3)	100	0.880792	0.028796
16	(3, 0.2, 4, 0.2)	100	0.580439	0.004162
17	(3, 0.3, 3, 0.3)	200	0.937803	0.002103
18	(3, 0.3, 4, 0.2)	200	0.753415	0.000318
19	(4, 0.2, 4, 0.2)	300	0.650613	0.000662

Table III (b)： SRMSE of estimators of cumulative hazard function under type I sampling

model	$(\alpha_1, \theta_1, \alpha_2, \theta_2)$	Sample size	$SRMSE\ (\hat{h}_Z^I(t))$	$SRMSE\ (\hat{h}_Z^D(t))$
5	(2, 0.2, 3, 0.3)	600	1.26047	1.149829
8	(2, 0.3, 3, 0.3)	600	1.46148	0.025552
9	(2, 0.3, 4, 0.2)	600	1.78924	0.012578
11	(2, 0.4, 3, 0.2)	600	0.94537	0.002345
12	(2, 0.4, 3, 0.3)	600	1.33613	0.006775
13	(2, 0.4, 4, 0.2)	600	1.74031	0.002909
14	(3, 0.2, 3, 0.2)	500	0.950136	0.001954
15	(3, 0.2, 3, 0.3)	600	1.00602	0.012435
16	(3, 0.2, 4, 0.2)	600	1.3859	0.005548
17	(3, 0.3, 3, 0.3)	600	2.008522	0.006284
18	(3, 0.3, 4, 0.2)	600	1.46812	0.002032
19	(4, 0.2, 4, 0.2)	600	1.677422	0.002589

Table III(c)： SRMSE of estimators of hazard function under type II sampling

model	$(\alpha_1, \theta_1, \alpha_2, \theta_2)$	Sample size	$SRMSE\ (\hat{h}_Z^I(t))$	$SRMSE\ (\hat{h}_Z^D(t))$
5	(2, 0.2, 3, 0.3)	100	0.8071	0.400269
8	(2, 0.3, 3, 0.3)	300	0.75127	0.015076
9	(2, 0.3, 4, 0.2)	100	0.91426	0.034165
11	(2, 0.4, 3, 0.2)	300	0.72258	0.000879
12	(2, 0.4, 3, 0.3)	200	0.78352	0.003587
13	(2, 0.4, 4, 0.2)	200	0.79346	0.000609
14	(3, 0.2, 3, 0.2)	400	0.515299	0.000431
15	(3, 0.2, 3, 0.3)	300	0.83351	0.006047
16	(3, 0.2, 4, 0.2)	100	0.80000	0.027369
17	(3, 0.3, 3, 0.3)	400	0.845056	0.001879
18	(3, 0.3, 4, 0.2)	100	0.82973	0.003289
19	(4, 0.2, 4, 0.2)	500	0.624114	0.0004984

Table III(d)：SRMSE of estimators of cumulative hazard function under type II sampling

Table III lists the value SRMSE of the direct and the indirect estimators for hazard function and cumulative hazard function under type I and type II sampling. The values of t used are those stopping points indicate in Fig III. Table III (a)(b) indicates that under sampling type I, the direct estimators of both hazard and cumulative hazard function are superior than the corresponding indirect estimators. Same results are arrived for type II sampling, see Table III(c)(d).

For those who are interested in graphs of SRMSE of the 19 models for both type I and type II sampling can contact the first author via e mail; All the results show that the direct estimators perform better than the indirect estimators.

4. Conclusion

In this article, when the independent components of a series system are from Exponentiated Weibull distributions with scale parameter σ given, we consider the case when the shape of the curve of hazard function is bathtub. We propose a direct estimator and an indirect estimator of both hazard function and cumulative hazard function. Intuitively, indirect estimator is more informative. However, the results we got from the 19 models indicate that the direct estimator performs much better than the indirect estimator in both hazard function and cumulative hazard function estimation. This is different from what Chen & Chu (2004) got for the case when the shape parameter θ is known , which said that the indirect estimator performs better. Other results we have from this research are (1) the type of sampling does not affect the results. (2) the closer the value of $\alpha\theta$ to one, the worse the indirect estimator is. The results can be extended to the case when the number of components is more than 2.

References

(1) Sy-Mien Chen and Hou-Yan Chu (2004) , "On Cumulative Hazard Function Estimation for Series System from Weibull Family." *Fu Jen Studies* , Vol 38 , pp 73-87 .

(2) Chen S. M and Hsu Y. S. (2002), "Quality Estimations for Assembly Products." Technical report (339-1-2001-1-227) of the division of academic research office of research and development at Fu-Jen Catholic University.

(3) Davis D.J. (1952) , "An Analysis Of Some Failure Data ." *Journal of the American Statistical Association* , Vol 47 , pp 113-150 .

(4) Lawless, J. F. (1982), Statistical Models and Methods for Lifetime Data. Wiley.

(5) Te-Yuan Lee (2003), "Two constraints and one criterion to approach the maintenance policy for sodium-hypochlorate system of power plant." MS thesis of department of mechanical and automation engineering ,National Kaohsiung First University of Science ,Taiwan.

(6) Lee J.B. and Max E (1991), "Statistical Analysis of Reliability and Life Testing Models." 2nd Ed. Marcel Dekker, New York.

(7) Lehmann , E.L. and Casella, G. (1998), "Theory of Point Estimation. " Springer , 2nd Ed.

(8) Meeker, W. Q.and Escobar, L. A.(1998), "Statistical Methods for Reliability Data." Wiley.

(9) Per Botolf Maurseth (2001) , "The impact of patent citations on patent duration ." Norsk Utenrikspolitisk Institutt , NUPI.

(10) Mudholkar G. S. , Srivastava D. K., Freimer M. (1995) , "The Exponentiated Weibull Family: A Reanalysis of the Bus-Motor-Failure Data. " Technometrics , Vol 37, pp 436-445 .

(11) Schankerman, M. (1998) "How Valuable Is Patent Protection? Estimates by Technology Field", RAND Journal of Economics , 29(1), pp 77-107.

(12) D.J. de Waal (1996) , "Teaching Bayesian Statistics in Reliability and Survival Analysis with Illustrations .", University of the OFS, Bloemfontein.

Acknowledge

This research is partially supported by the National Science Council, R.O.C. research plan NSC 93-2118-M-030-006 of the first author.

received October 31, 2005
revised November 23, 2005
accepted December 11, 2005

指數韋伯串聯系統故障函數之估計

陳思勉
輔仁大學應用科學與工程研究所
戴涓珍
輔仁大學數學系

摘　要

一個三參數指數偉伯分佈 $EW(\sigma, \alpha, \theta)$ 在 $\alpha>1$ 且 $\alpha\theta<1$ 時具備澡缸型失效函數。本文將討論一個由來自指數偉伯分佈之獨立零件依串聯方式而得之系統的（累積）失效函數之直接與間接估計式，研究結果顯示在樣本相對均方差的比較準則之下直接估計式優於間接估計式。

A New Predictor-Corrector Method for Solving Initial-Value Problems of Nonlinear Ordinary Differential Equations

L. Tsai *, H.Y. Liou and G. F. Jiang

Dept. of Mechanical Engineering,
Ching-Yun University, Zhong-Li, Taiwan.

Abstract

An alternative approach to solving the initial-value problems for nonlinear differential equations is presented in this paper, in which focus is on the incorporation of GM(1,1) model in the grey prediction into PCM (Predictor-Corrector Method) in the numerical schemes. Special attention is paid to the so-called "improved Euler's and Adam's methods" to inspect the applicability of grey prediction merged into the solving process in place of the original "predictor" part of PCM. Besides, the "jumping technique" is adopted for smoothing the prediction base. Two examples are herein presented to verify the feasibility of the method stated above; one is the mathematical differential problem for the improved Euler's method, and the other two include the applications on the problems of the chain pulled upward by a constant force as well as the nonlinear model of the swing of a pendulum for Adam's PCM. From an engineering point of view, the revised method indeed yields satisfactory results. Therefore, such a similar method as presented in this paper can be, to some extent, generalized to the related issues in the numerical field.

Key words:GM(1,1) model, PCM, Improved Euler's method, Adam' method, Jumping technique.

---

* Corresponding author. Fax: +886-3-468-3301.
E-mail: johntsai@cyu.edu.tw

1. Introduction

A variety of applications subject to grey prediction theory have been fulfilled in areas associated with prospective estimations so far since it was pioneered by Professor Deng (Deng, 1982). The GM(1,1) model (Deng, 1987), serving as a powerful prediction tool based on only few past data, has exhibited its accessibility to the applications in distinct fields such as agriculture, commerce, military, industry, and so forth. However, among the studies above, the fruition of the numerical analysis aided with grey prediction seems fairly scarce. One among these was the application of the grey prediction to improving the gradient descent method in numerical schemes by Hong and Chen, who increased the searching speed of finding the global minimum point and successfully skipped the local minimum in compensation for the drawbacks of other regular gradient descent methods (Hong & Chen, 1999). Besides, Liang and Chang made a comparison between grey prediction and regression model in numerical scheme concerning the residual service lives of existing concrete bridges, and drew a conclusion that the results acquired from the former based on the same raw data were more reliable (Liang & Chang, 2002). Tong and Liang incorporated grey prediction technique into the issue of the neural network to predict the repairable system in vehicle industry with the past failure data (Tong & Liang, 2002). The authors of this paper, Tsai and Liou, also adopted the GM(1,1) model to the shooting method, which is essentially the application of the Runge-Kutta technique, for solving the boundary-value problems. An improved shooting technique, rather than a traditional shooting scheme, was successfully developed therein to achieve the effect of saving computer CPU running time (Liou et al., 2004). In the numerical field, the popularity of Runge-Kutta method lies in its accuracy of approximating solutions for initial-value problems. Nevertheless, a major drawback arises from the necessity of four-time evaluations at each time step while it is adopted, thus causing a lot of computer time expense during the whole process of simulation. The Adam's PCM scheme, as compared with the Runge-Kutta method, requires only one-new-function evaluation for each time step to the advantage of great time-saving but still remains the same error property.

Accordingly, in consideration of the initial-value problems for nonlinear differential equations, the authors attempt to proceed with the so-called "grey prediction-corrector" method to justify the feasibility of the GM(1,1) model applied to the numerical scheme. The essence of the present paper exists in the inclusion of grey prediction in the solving process to substitute for the original "predictor" part of PCM and the use of the "jumping technique" for trend smoothing. An important purpose is to inspirit other researchers to undertake a similar approach to the related issues, and to stretch the utilization of grey prediction theory out of the scope of the current studies.

2. Theory

2-1 Grey Prediction-Corrector Method

In this section, a brief review related to both improved Euler's and Adam's methods is made first, and then the incorporation of GM(1,1) model into each of them is undertaken so as to survey the capability of grey prediction in the process of computation.

2-1-1 GM(1,1) Model on Improved Euler's method (Zill, 2000)

Consider a first-order initial-value problem

$$y' = f(x, y), \ \ y(x_0) = y_0 . \tag{2-1}$$

The iterative equation adopted in Euler's method is given as:

$$y_{n+1} = y_n + h \cdot f(x_n, y_n) , \tag{2-2}$$

where f is the function demonstrated in eq. (2-1). The recursive use of eq. (2-2) for n=0, 1, 2, 3⋯ yields the corresponding y_1, y_2, y_3 ⋯, which are the points on successive "tangent lines" to the solution curve at x_1, x_2, x_3 ⋯, or say $x_n = x_0 + n \cdot h$, where h is a constant or step size between x_n and x_n+1. In fact, lots of engineers utilize the formula to approximate the solution due to its simplicity of programming, yet the disadvantage originates in the roughness of the computed results. Hence, the improved Euler's method is developed to overcome this drawback but still remain its simplicity. The iterative equation (2-2) is modified into two steps:

$$y_{n+1} = y_n + h \cdot \frac{f(x_n, y_n) + f(x_{n+1}, y^*_{n+1})}{2} \tag{2-3}$$

and $$y^{*}_{n+1}= y_n+h \cdot f(x_n, y_n), \tag{2-4}$$

where y^{*}_{n+1} is called a predictor and y_{n+1} a corrector.

The essence of this improved method is that a refined value y_{n+1} is reached as soon as an initial estimate y^{*}_{n+1} obtained from eq. (2-4) is plugged back into eq. (2-3).

In general, the value of y^{*}_{n+1} given by eq. (2-4) predicts a value of $y(x_{n+1})$, whereas y_{n+1} denoted in eq. (2-3) corrects its estimate. In this paper, in an attempt to skip eq. (2-4), the authors utilize the GM(1,1) model instead to predict y^{*}_{n+1} for obtaining the value of y_{n+1}. The idea of the GM(1,1) model is briefly stated as follows:

The grey discretized equation for GM(1,1) is

$$y^{(0)}(k)+az^{(1)}(k)= u , \tag{2-5}$$

where a and u are called the development coefficient and grey input, respectively.

The whiten response of (2-5) is

$$\hat{y}^{(1)}(k+1)=[y^{(0)}(1)-\frac{u}{a}]e^{-ak}+\frac{u}{a}, \tag{2-6}$$

The model parameters a and u are obtained by the least square method as below:

$$\begin{bmatrix} a \\ u \end{bmatrix}=(B^T B)^{-1}B^T Y, \tag{2-7}$$

$$\text{where } B=\begin{bmatrix} -0.5(y^{(0)}(1)+y^{(0)}(2) & 1 \\ -0.5(y^{(0)}(2)+y^{(0)}(3) & 1 \\ \vdots & \vdots \\ -0.5(y^{(0)}(n-1)+y^{(0)}(n) & 1 \end{bmatrix}, \quad Y=\begin{bmatrix} y^{(1)}(2) \\ y^{(1)}(3) \\ \vdots \\ y^{(1)}(n) \end{bmatrix}.$$

Finally, the model value of $\hat{y}^{(0)}$ at step k is obtained as:

$$\hat{y}^{(0)}(k)=\hat{y}^{(1)}(k)-\hat{y}^{(1)}(k-1), \tag{2-8}$$

where $\hat{y}^{(0)}(1)=y^{(0)}(1)$, and y^{*}_{n+1} is substituted by $\hat{y}^{(0)}(k)$ in this paper.

Based on the frame above, the so-called "four points rolling checking" method (updating elements of the prediction base) associated with grey prediction is adopted and therein its powerful merit is revealed. In order to build the prediction base, eqs. (2-3) and (2-4) are executed to create $y_1^{(0)}$, $y_2^{(0)}$, $y_3^{(0)}$, and $y_4^{(0)}$ with the same error property. The flow chart of the entire computational process is demonstrated in Fig. 1.

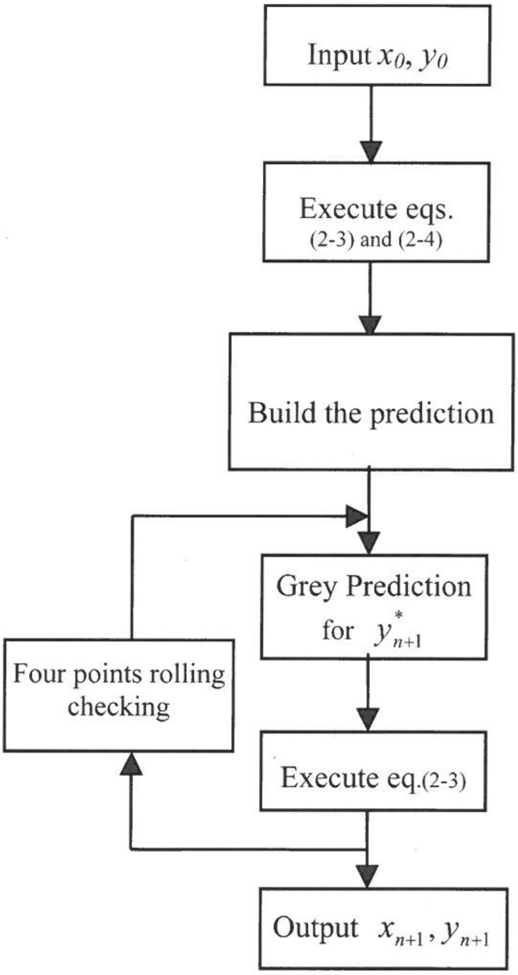

Fig. 1 Flow chart of grey prediction improved Euler's method

2-1-2 GM(1,1)Model on Adam's Method (Nakamura, 1995)

The GM(1,1) model merged in the Adam's PCM scheme is proceeded as follows : Firstly, primary concern is made for the predictor part in the Adam's numerical scheme, in which the Lagrange interpolation formula of order 3 is adopted here to fit y_n' , y_{n-1}' , y_{n-2}' and y_{n-3}' so as to attain an approximation of $y'=f(x,y)$, i.e.,

$$
\begin{aligned}
y' = {} & \frac{(x-x_n)(x-x_{n-1})(x-x_{n-2})}{(x_{n-3}-x_n)(x_{n-3}-x_{n-1})(x_{n-3}-x_{n-2})} y'_{n-3} + \frac{(x-x_n)(x-x_{n-1})(x-x_{n-3})}{(x_{n-2}-x_n)(x_{n-2}-x_{n-1})(x_{n-2}-x_{n-3})} y'_{n-2} \\
& + \frac{(x-x_n)(x-x_{n-2})(x-x_{n-3})}{(x_{n-1}-x_n)(x_{n-1}-x_{n-2})(x_{n-1}-x_{n-3})} y'_{n-1} + \frac{(x-x_{n-1})(x-x_{n-2})(x-x_{n-3})}{(x_n-x_{n-1})(x_n-x_{n-2})(x_n-x_{n-3})} y'_n .
\end{aligned}
\tag{2-9}
$$

If eq. (2-9) is in terms of the local coordinate, $z=x-x_n$, then it can be reformulated as:

$$
\begin{aligned}
y' = {} & \frac{(2h+z)(h+z)(z)}{(-h)(-2h)(-3h)} y'_{n-3} + \frac{(3h+z)(h+z)(z)}{(h)(-h)(-2h)} y'_{n-2} + \frac{(3h+z)(2h+z)(z)}{(2h)(h)(-h)} y'_{n-1} \\
& + \frac{(3h+z)(2h+z)(h+z)}{(3h)(2h)(h)} y'_n ,
\end{aligned}
\tag{2-10}
$$

where h is a constant or step size between x_n and x_{n+1}. In order to predict y_{n+1} at which $x_{n+1}=x_n+h$, it is necessary to integrate the following equation with the known value of y_n :

$$
y_{n+1} = y_n + \int_0^h y' \, \mathrm{d}z . \tag{2-11}
$$

When eq. (2-10) is plugged into eq. (2-11), is yielded as

$$
y^*_{n+1} = y_n + \frac{h}{24}(55y'_n - 59y'_{n-1} + 37y'_{n-2} - 9y'_{n-3}) , \tag{2-12}
$$

where y^*_{n+1} here is the predictor in Adam's method.

Equation (2-12) is used as an extrapolation, the accuracy of which is less than that for an interpolation. Hence, in order to refine the value of y_{n+1} , it is imperative now to derive a corrector formula based on the interpolation, i.e., the procedure of shifting y_n' , y_{n-1}' , y_{n-2}' and y_{n-3}' to $y_{n+1}'^{*}$

, y'_n, y'_{n-1} , y'_{n-2} , where $y'^{*}_{n+1}=f(y^{*}_{n+1},x_{n+1})$. With this idea kept in mind and the same procedures followed as described from eqs. (2-9) to (2-12), the corrector formula is established as:

$$y_{n+1}=y_n+\frac{h}{24}(9y'^{*}_{n+1}+19y'_n-5y'_{n-1}+y'_{n-2})\,. \tag{2-13}$$

Now, in place of eq. (2-12), the GM(1,1) model is induced to execute the "predicting" task and eq. (2-13) is then applied to refining the estimated value. The preceding revised method still remains the advantage over Runge-Kutta scheme.

In analogy to the procedure of Adam's PCM model, at least four known values, say $y_1^{(0)}$, $y_2^{(0)}$, $y_3^{(0)}$, and $y_4^{(0)}$, are needed to serve as the prediction base for the future prediction in GM(1,1) model, so the traditional Runge-Kutta method is utilized for three-time iterations for the above purpose. With these elements as the base, the value of can be predicted from eqs. (2-5) to (2-8). Besides, in accordance with grey theory, an increase in the smoothness of the orderly base data is beneficial to the creation of an unbiased predicted value. Therefore, with the aim of enhancing the accuracy of a predicted value, the "jumping technique", which was proposed by Chen (Chen, 2002), is applied in the present paper.

2-2 Jumping Technique

Suppose $y^{(0)}$ indicates a prediction base as expressed by eq. (2-5). The ratio of adjacent value is defined as:

$$\lambda(k)=\frac{y_{k-1}^{(0)}}{y_{(k)}^{(0)}}\ ,\ k=2,3,\ldots n, \tag{2-14}$$

and the ratio as a criterion for deciding the jump point is

$$\rho(k)=\left|\frac{\lambda(k)-\lambda(k-1)}{\lambda(k)}\right|\ ,\ k=2,3,\ldots n. \tag{2-15}$$

If $\rho(\tau)\geq\zeta$, then $y^{(0)}(\tau)$ can be declared as a jump point, and $\zeta\in(0\,,1)$ indicates how the value in the neighborhood of another value in the prediction base can be claimed as a jump point.

If a jump point is detected at -th point, the original prediction base can be divided into two subsections:

$$y^{(0)}=y_{\mathrm{I}}^{(0)}\cup y_{\mathrm{II}}^{(0)} \tag{2-16}$$

where $y_{\mathrm{I}}^{(0)}=(y^{(0)}(1),y^{(0)}(2)...y^{0}(\tau-1)$ and $y_{\mathrm{II}}^{(0)}=(y^{(0)}(\tau),y^{(0)}(\tau+1)...y^{0}(n))$.

In order to convert into a "smoother" series, a constant is multiplied to all elements of $y_{\mathrm{II}}{}^{(0)}$ as follows:

$$\Psi_{2}^{(0)}=\gamma y_{II}^{(0)}=(\gamma y^{0}(\tau+1)...\gamma y^{0}(n)), \tag{2-17}$$

where $\gamma=\dfrac{y^{(0)}(\tau-1)}{\lambda y^{(0)}(\tau)}, \lambda=\dfrac{y^{(0)}(\tau-2)}{\lambda y^{(0)}(\tau-1)}$.

After γ is determined, new elements in the prediction base are denoted as

$$\Psi^{(0)}=\Psi_{1}^{(0)}\cup\Psi_{2}^{(0)}, \tag{2-18}$$

where $\Psi_{1}^{(0)}=y_{\mathrm{I}}^{(0)}$.

The new elements in eq. (2-18) will be applied to GM(1,1) model as the prediction base for future prediction and the actual predicted value can be restored back as

$$y_{\mathrm{II}}^{(0)}(k)=\frac{\Psi_{2}^{(0)}(k)}{\gamma}, \tag{2-19}$$

where y_5^* as stated above represents the value of $y_{\mathrm{II}}{}^{(0)}(5)$ in the paper.

The flow chart of the entire computational process is demonstrated in Fig. 2.

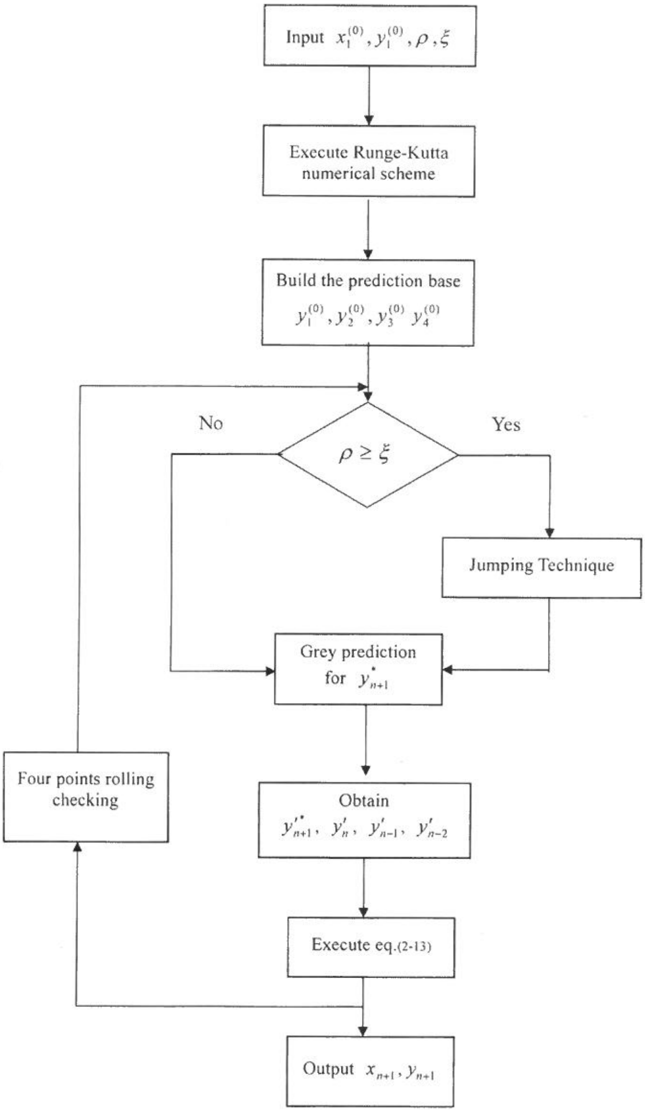

Fig. 2 Flow chart of grey prediction Adam's method

3. Applications

In this section, two examples, one the first-order differential equation and the other problem of the nonlinear model of the swing of a pendulum (Zill, 2000) are propounded to examine the capability of the grey prediction-corrector method described in the preceding section.

3-1 GM(1,1) Model on Improved Euler's Method

Example: A First-Order, Initial-Value Problem

Associated with the study in this sub-section, a first-order, initial-value problem is considered as follows:

$$y'=f(x,y)=-20y+7e^{-0.5x},\ y(0)=5\ , \tag{3-1}$$

of which the exact solution is $y=(5-\frac{7}{19.5})e^{-20x}+\frac{7}{19.5}e^{-0.5x}$. In the process of computation, the step size $\Delta x=h=0.01$ is assumed and the successive values of y are computed until $z_0=0+n\cdot h=1$ is met. For comparison, not only the main task according to the flow chart shown in Fig.1 for the incorporation of GM(1,1) model into the improved Euler's method, but also the relevant calculations on eq. (2-2) related to the Euler's method and eqs. (2-3) and (2-4) related to the improved Euler's method are executed, respectively. Fig. 3 shows the results by means of all three methods, from which we can hardly perceive the distinctions among them. In Fig. 4, the comparison of results from the three methods is made with the exact solution and the maximum absolute errors are tabulated in Table 1.

Table 1 Comparison of errors for three Euler's methods

Method	Improved Euler's method	Grey prediction improved Euler's method	Euler's method
Max. value of abs. errors	0.01327	0.01296	0.1856
Average value of abs. errors	0.00178	0.00169	0.02375

From the above, it shows that the outcome followed by the GM(1,1) model incorporated into the improved Euler's method has, to some extent, the advantage in the accuracy over those by the other two methods. Of course, the improvement of accuracy is expected to achieve with even smaller step size h within an acceptable tolerance of computer time consumption.

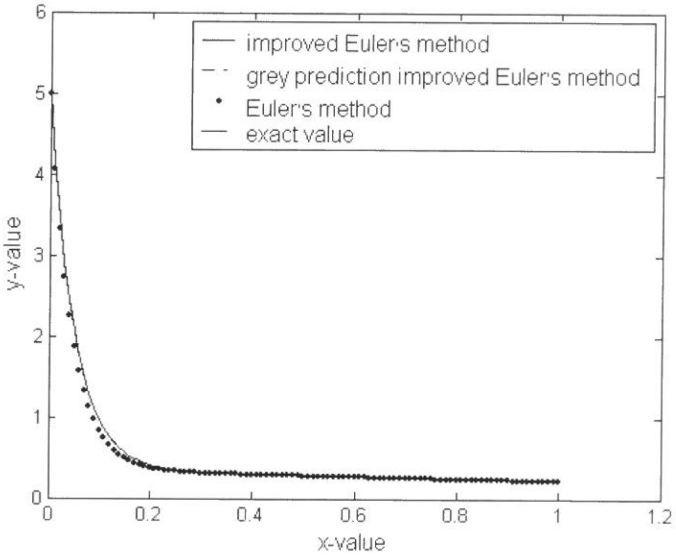

Fig. 3. Numerical results of three Euler's methods

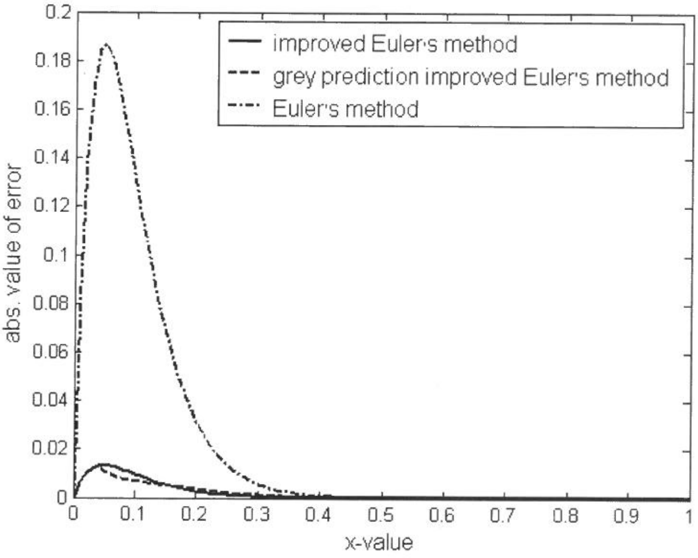

Fig. 4. Absolute values of error compared with exact solution

3-2 GM(1,1) Model on Adam's Method

Example: Nonlinear Model of the Swing of a Pendulum

The secondary example presented in this sub-section, as shown in Fig. 5, is a "simple pendulum" consisting of a bob of mass m attached to a rod of length l, which swivels in a vertical plane.

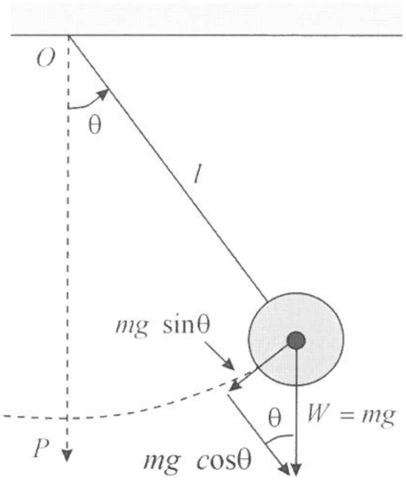

Fig. 5 A model of the swing of a pendulum

In describing its motion, assumptions are made that the mass of the rod is negligible and that the damping effect and the external force exerted on the rod are beyond our concern. According to these, the governing equation for describing the present physical model is as follows:

$$\frac{d^2\theta}{dt^2}+\frac{g}{l}\sin\theta=0,\quad \theta(0)=\frac{1}{2},\ \theta'(0)=2, \tag{3-2}$$

and the above equation can be divided into two first-order equations for computation:

$$\frac{d\theta}{dt}=z,\quad \frac{dz}{dt}+\frac{g}{l}\sin\theta=0 \tag{3-3}$$

Apparently, the above eq. (3-2) is a highly nonlinear differential equation; as is the usual case, simplification can be made by replacing the term sin by θ such that the linearization of eq. (3-2) is attained. However, aside from that, the authors attempt to deal with this problem by retaining the original nonlinear form. As a result of the difficulty in obtaining an analytical solution, the numerical methods will be applied and the computed results by the traditional Runge-Kutta method will serve as the criteria for comparisons. For the purpose of simplification, $\omega^2=\frac{g}{l}=1$ is assumed in the process of simulation. Meanwhile, the step size $\Delta t=h=0.001$ is assumed and the calculation of the successive values of θ is not terminated until $y_n=0+n\cdot h=15$ is reached. Figs. 6 and 7 show the results of angular displacement and velocity, respectively by three numerical schemes, in which, the curves overlap entirely and any further distinction among them can hardly be made. In Fig. 7 is exhibited the physical phenomenon that in the absence of damping, angular displacement increases indefinitely as time elapses, which is in contrast to the back-and-forth oscillation for the linearlized treatment of the model under consideration. From these two figures, jump points are apparently detected. In order to study the influence of jumping technique on the present case, the criterion of $\zeta=10^{-5}$ is set for jumping herein. Figs. 8 and 9 illustrate the absolute errors for the comparison of traditional Adam's PCM with Runge-Kutta schemes. The absolute errors for angular displacement as well as velocity are shown in Figs. 10 and 11, respectively for the comparisons of grey prediction-corrector method with/without jumping with Runge-Kutta method. As shown in these two figures, the grey prediction-corrector method aided with the jumping technique is obviously superior to the mere utilization of the former one. Though the values of absolute error associated with the present method seem higher than those with Adam's PCM model, the accuracy still reaches an order of 10^{-5} in magnitude for the present example. From an engineering point of view, it indeed yields satisfactory results.

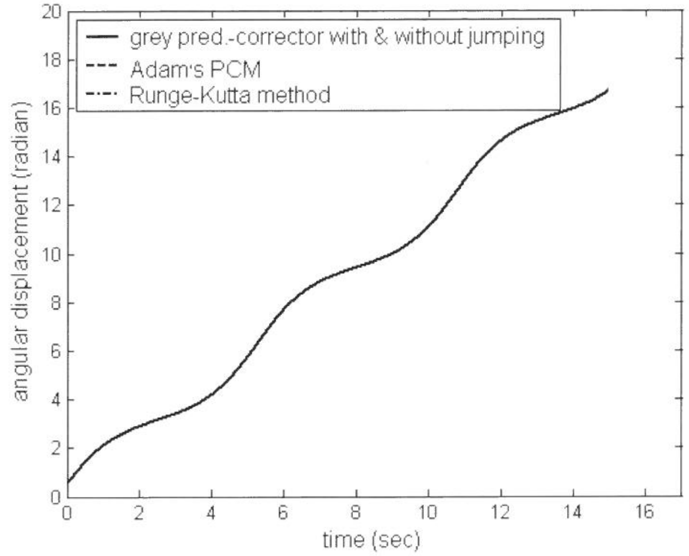

Fig. 6 Angular displacement by using three numerical schemes

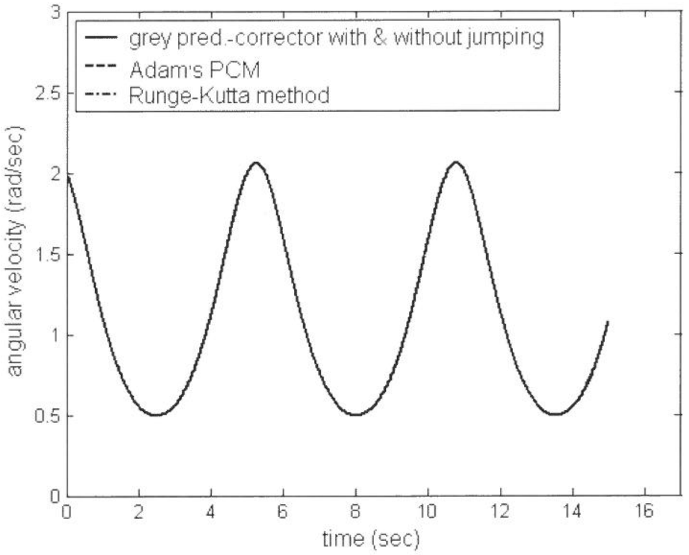

Fig. 7. Angular velocity by using three numerical schemes

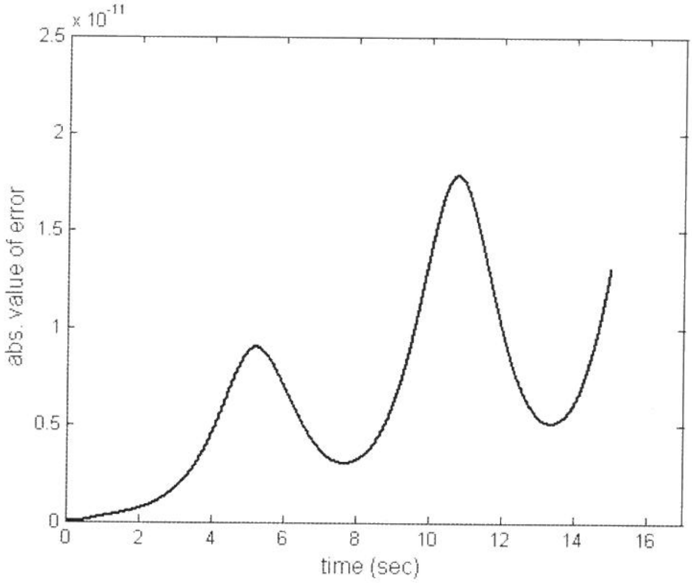

Fig. 8 Absolute errors for angular displacement between Adam's PCM and Runge-Kutta method

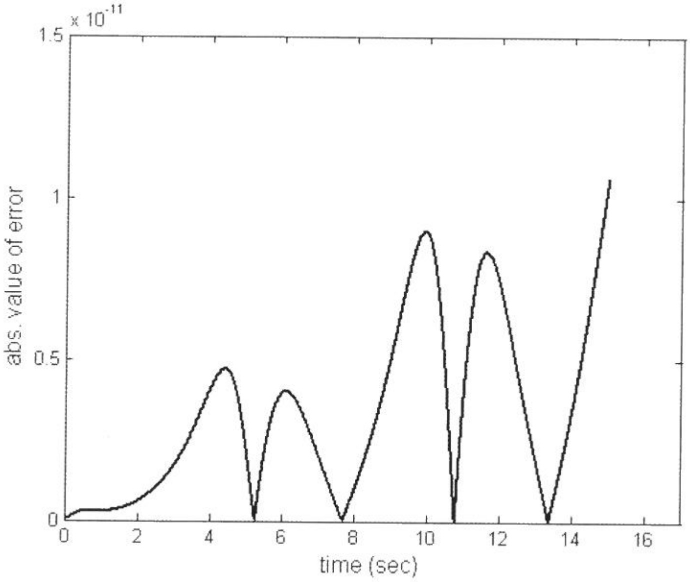

Fig. 9 Absolute errors for angular velocity between

Adam's PCM and Runge-Kutta method

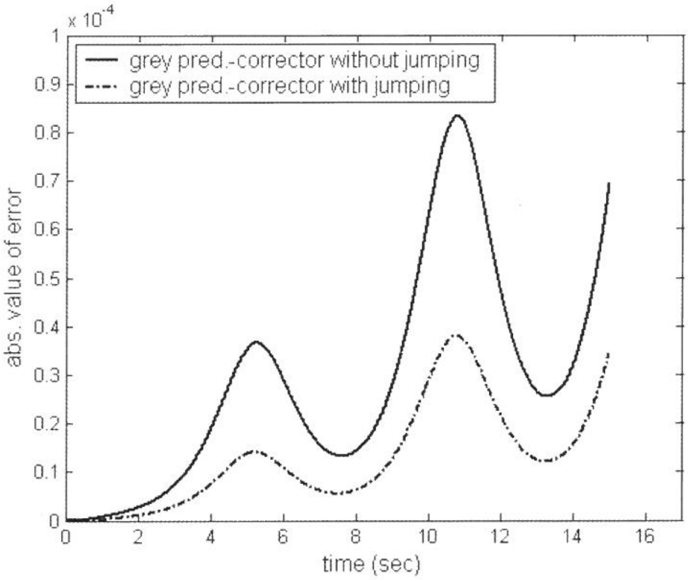

Fig. 10 Absolute errors of angular displacement by Grey Prediction-Corrector method with & without Jumping compared with Runge-Kutta method

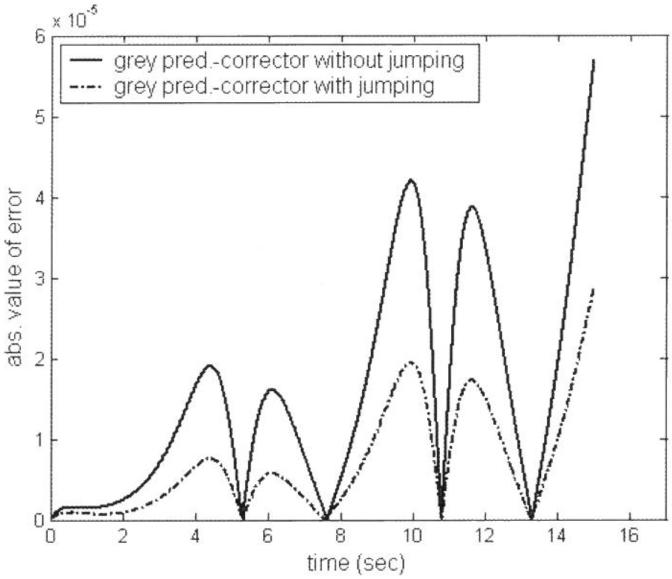

Fig. 11 Absolute errors of angular velocity by Grey Prediction-Corrector method with & without Jumping compared with Runge-Kutta method

4. Conclusions

The main purpose of this paper is to report on an alternative approach to solving initial-value problems for nonlinear differential equations by incorporating the GM(1,1) model in grey theory into the traditional predictor-corrector methods. In accordance with the preceding sections, the following conclusions are drawn:

(1) The grey prediction-corrector scheme presented in this paper is apparently superior to the improved Euler's method without losing its simplicity and easiness of programming.

(2) The results from the secondary example as shown in the preceding section reveal the ability of the present method used in the problems when jumping points are detected. Even though, with jumping technique, the output of absolute error is beneficial to the computed values, the outcomes from the present method without jumping technique are quite acceptable from an engineering point of view.

References

(1) Chen, C. H., "A New Method for Grey Modeling Jump Series," the Journal of Grey System, Vol.14, No.2, pp.123-132 (2002).

(2) Deng, J.L., "Control Problems of Grey System, *System and Control Letters*," Vol.1, No.5, pp.288-294 (1982).

(3) Deng, J.L., the Essential Methods of Grey Systems, Huazhong University of Science & Technology Press, Wuhan (1987).

(4) Hong, C. M. and Chen, C. M., "A New Gradient Serach Method Based on Grey Prediction Theory," the Journal of Grey System, Vol.11, No. 3, pp.191-208 (1999).

(5) Liang, M. T., and Chang, J. W., "Grey and Regression Methods Predicting the Remaining Service Life of Existing Reinforced Concrete Bridges," the Journal of Grey System, Vol. 14, No. 3, pp.291-310 (2002).

(6) Liou, H. Y., Tsai, L., and Lo, H. S., "The Application of Grey Prediction to Shooting Method for Nonlinear Second-Order Boundary- Value Problems," the Journal of Grey System, Vol.16, No. 4, pp.331-337 (2004).

(7) Nakamura, S., Applied Numerical Methods in C, Prentice-Hall (1995).

(8) Tong, L. I., and Liang, Y. H.,"Neutral Network and Grey Analysis and Forcast the Field Failure Data for Repairable System," the Journal of Grey System, Vol.14, No. 4, pp. 341-349 (2002).

(9) Zill, D. G., Cullen, M. R., Advanced Engineering Mathematics, Jones and Bartlett Publishers (2000).

received October 31, 2005
revised November 25, 2005
accepted December 13, 2005

應用預測－修正法則求解非線性微分方程式初始值問題

蔡　龍　劉宏毅　簡光甫
私立清雲科技大學
機械工程學系
桃園縣中壢市健行路 *229* 號

摘　要

本篇文章係應用灰預測之 GM(1,1) 模式融入數值運算 PCM (Predictor-Corrector Method)方法求解非線性微分方程式初始值問題。文中乃著眼於所謂之改良尤拉及亞當法 (improved Euler's and Adam's methods)以檢驗灰預測法取代改良式尤拉及亞當法中預測部分之可行性。此外，灰預測理論中「jumping」技巧亦被應用於預測基地之平滑化。在文中舉出二例以驗證上述改良方法之適用性，其一爲改良式尤拉法求解微分方程式初始值問題，其二爲亞當法求解擺錘非線性運動問題。從工程觀點而言，本文章所提出之改良法確實可達成令人滿意之結果。因此同樣類似之方法在某種程度上可推廣於數值領域中相關之議題。

關鍵詞：GM((1,1)模式；改良式尤拉法；改良式亞當法；jumping 技巧。

Morphological and Optical properties of the TiO_2/Al_2O_3 and TiO_2/SiO_2 Films by Electron Beam Evaporation

K.C. Lin[1]*, C.R. Yang[1], K.T. Wu[1], and Y.D. Yao[2]
[1]*Department of Physics, Fu Jen Catholic University,*
Chung Cheng Rd. 510, HsinChuang City, Taipei County 242, Taiwan, R.O.C
[2]*Institute of Physics, Academia Sinica,*
128 Sec. 2, Academia Rd., NanKang, Taipei 115, Taiwan, R.O.C

Abstract

Atomic force microscopy and transmission spectroscopy are utilized to study the morphological and optical properties of the TiO_2/Al_2O_3 and TiO_2/SiO_2 films grown by electron beam evaporation. The surface roughness of films with different composition ratio shows distinct changing trend between two formulas of TiO_2/Al_2O_3 and TiO_2/SiO_2. The cutoff wavelength that the transmission value drops below 20% of the transmission spectra of the prepared films is between 200 nm and 400 nm. Thickness and dopant effects on the cutoff wavelength are discussed.

Key words : oxide composites, surface morphology, transmission spectra, AFM

Introduction

Composite oxides are considered quite applicable materials in many aspects, such as electronics, photo-catalysts, and optical components with modified mechanical, electrical, and optical properties [1-3]. For example, TiO_2/Al_2O_3 can be used as the coating materials of liquid crystal display conducting electrodes for scratch protection and excellent transparency. The hy-

---

*Corresponding author. Tel:+886-2-29053754
E-mail: phys2017@mails.fju.edu.tw

brid of SiO_2/TiO_2 and organic composites is reported as materials for optical waveguides [4]. The deposition parameters and post-growth treatments of composite films will affect the properties tremendously. In this brief report, we study the properties of the binary oxides of TiO_2 /Al_2O_3 and TiO_2 /SiO_2 films at set sample preparation procedures. Although both Al_2O_3 and SiO_2 are glassy materials with lower refractive indices compared to TiO_2, some interesting variation of the mixing type between TiO_2 /Al_2O_3 and TiO_2 /SiO_2 is found from the optical result. Possible explanation might be the metal inter-percolating between TiO_2 and Al_2O_3 [5] that such effect might be missing in TiO_2 /SiO_2 composite.

Experimental

The samples are prepared in a high vacuum deposition chamber with a base pressure of 1.3×10^{-6} torr. The electron beam gun equipped is manufactured by ULVAC, model EGK-3M, with the power supply of HP-5100C. A quartz balance thickness monitor by Maxtek, model TM-350 is chosen to record the deposited film thickness. Various compositions of TiO_2 /Al_2O_3 and TiO_2 /SiO_2 powders are weighted, mixed, and placed inside the water cooled crucibles for e-beam bombardment. Composite films are grown on glass substrates, Corning Glass # 7059. The substrate temperature is held at 200 °C during the deposition for the films discussed in this paper. The growth rate is controlled at 1nm/sec. The atomic force microscopic measurement with NT-MDT P47H and the spectroscopic measurement with Varian Cary 5E, are done ex situ. All the sample preparation and experiments are completed at Department of Physics, FuJen Catholic University.

Result

(I) Structure and surface morphology

There is no obvious crystalline phase formed of TiO_2 /Al_2O_3 and SiO_2 /TiO_2 from X-ray diffraction measurement. The X-ray diffraction result of Al_2O_3 with various film thickness is shown in Figure 1. The composite film does show some activities of the photo-catalytic decomposition test that indicates possible anatase phase of TiO_2. However, we don't have direct evidence of this assumption. All the films in this report are considered being amorphous.

A typical surface 3D profile image of the deposited 100 nm film is illustrated in Figure 2. The average surface roughness of mono-component films from our data is shown in Figure 3. Among the three components of SiO_2, TiO_2, and Al_2O_3, the film roughness of SiO_2 displays the highest number 1.5 nm and the Al_2O_3 film exhibits the lowest one, ~0.62 nm. The estimated average granular size on the films is about 30 nm. The grain size of SiO_2 is also the largest, ~40 nm. However, TiO_2 has the minimum average grain size, ~20nm. Although detailed growth mechanism of the composite films can not be obtained through our results, we can see common features in the changing trend. TiO_2/Al_2O_3 film roughness values decrease as the Al_2O_3 composition ratios increase, as shown in Figure 4, and TiO_2/SiO_2 film roughness values increase as the SiO_2 composition ratios increase, as shown in Figure 5. The surface roughness value is 1nm that its scattering effect on the transmission measurement is regarded as negligible.

(II) Transmission spectra

For simplicity, the cutoff wavelength of our composite films is defined as the transmission drops below 20% which is roughly the turning point of the transmission drop-off. The cutoff wavelength of TiO_2 films shifts from 325 nm to 340 nm as the film thickness increases from 100 nm to 300 nm. There is no distinguishable thickness effect on the cutoff frequency of mono-component SiO_2 or Al_2O_3 films. When the film material TiO_2 is mixed either with SiO_2 or Al_2O_3, both composites shift the cutoff wavelength to 280 nm, as shown in Figure 6 and Figure 7. The composition effect on TiO_2/Al_2O_3 films exhibit a continuous change on the cutoff wavelength. Although the TiO_2/SiO_2 (10%) and TiO_2/SiO_2 (30%) films with 300nm thickness show the cut-off wavelength at 320nm and 330 nm, the cut-off wavelength of other compositions of TiO_2/SiO_2 films persists at 280 nm. There is some fundamental difference between these two mixtures. For TiO_2/SiO_2, the major component probably serves as the matrix and the optical property of the minor component is concealed. It is reported that the electronic structure of SiO_2-TiO_2 matrices varied with composition [6]. On the other hand, the TiO_2/Al_2O_3 composite exhibits the inter-medium optical characteristics of both compounds. It is also reported that Ti and Al species function synergistically in photo-induced direct methane coupling that the substitution between Ti and Al sites might occur [3]. Detailed structural and electronic studies are further required.

Summary

Optical properties of TiO_2/SiO_2 and TiO_2/Al_2O_3 composite films have been studied. The mixing type difference between two formulas of TiO_2/SiO_2 and TiO_2/Al_2O_3 is observed from the transmission spectra. The surface roughness characteristics are attributed to the nature of amorphous films.

References

(1) Dong-Hau Kuo and Cheng-Nan Shueh, *Thin Solid Films* **478**, p.109(2005)

(2) Song-Zhu Chu, Satoru Inoue, Kenji Wada, Di Li, and Jun Suzuki, *Langmuir* **21**, p.8035 (2005).

(3) Hisao Yoshida,Norimitsu Matsushita, Yuko Kato, and Tadashi Hattori, *J. Phys. Chem. B* **107**, p8355(2003).

(4) Wei Chen, Xiaoming Tao, Junying Zhang, Qi Fang and Jun Yang, *J. American Ceramic Society* **88**, p 2998 (2005)

(5) C. Verdozzi, P.A. Schultz, Ruqian Wu, A.H. Edwards, and Nicholas Kioussis, *Phys. Rev.* B **66**, p.125408(2002).

(6) iTomohiro Ishiwaki, Hiroyuki Inoue, and Akio Makishima, *J. Non-Crystalline solids* **244**, p.151(1999).

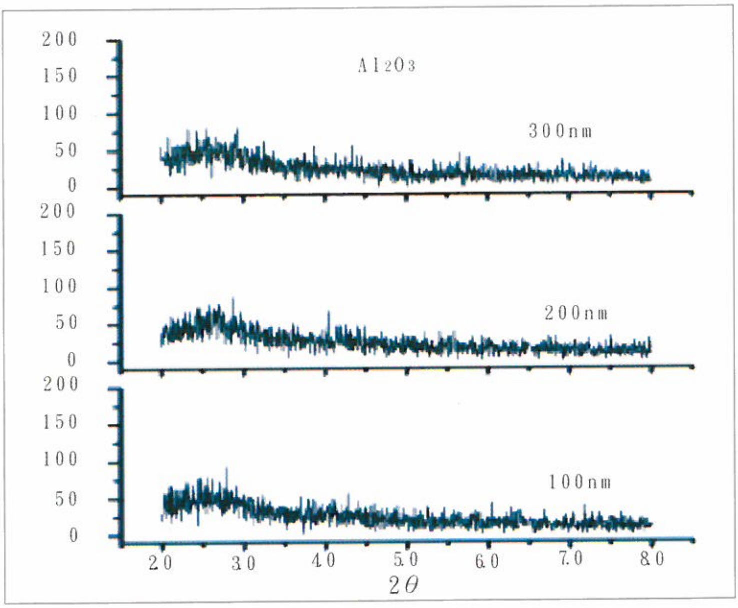

Figure 1 X-ray diffraction data of Al_2O_3 films

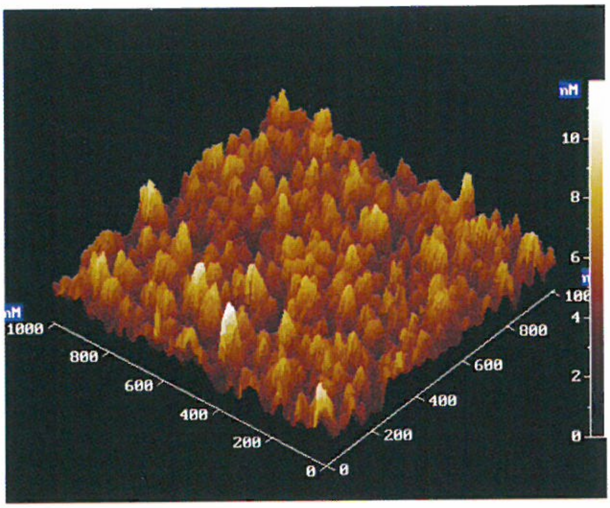

Figure 2 Tapping mode AFM image of Al_2O_3, film thickness 100 nm thickness, image size 1μm × 1μm.

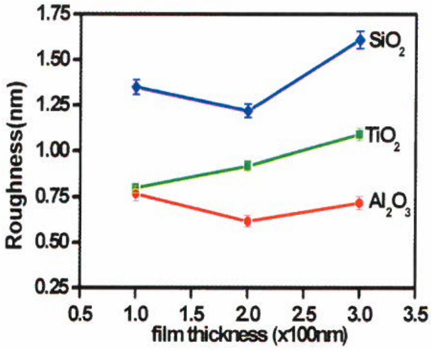

Figure 3 Average surface roughness of mono-component films with various thickness.

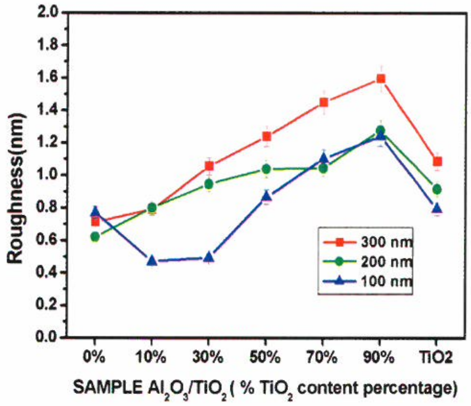

Figure 4 Average surface roughness of Al_2O_3/TiO_2 composite films with various thickness

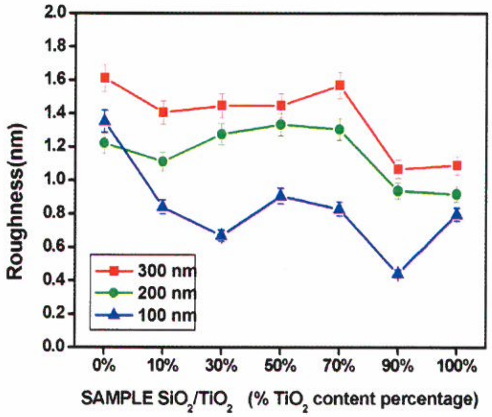

Figure 5 Average surface roughness of SiO_2/TiO_2 composite films with various thickness

電子槍蒸鍍製成的鈦鋁氧化物與鈦矽氧化物薄膜的表面型態與光學性質的研究

林更青　楊忠如　吳坤東
輔仁大學物理系
姚永德
中央研究院物理研究所

中文摘要

利用顯微術與透射光譜，來研究電子槍蒸鍍製成的鈦鋁氧化物與鈦矽氧化物薄膜的表面型態與光學性質。對兩類混成氧化物而言，隨著其成份比值的改變，其薄膜表面粗糙度的變化趨勢有明顯的不同。而薄膜的透射光譜截止波長值介於 200nm 到 400nm 間，薄膜厚度與混成氧化物成份比值對截止波長的影響，顯示兩類混成氧化物的混合結構有差異性質存在。

關鍵詞：混成氧化物，表面形貌，原子力顯微術，透射光譜

Studies on Multi-Carrier CDMA Systems with Space-Time Block Codes

Jung-Lang Yu and Chih-Chan Lin

Department of Electronic Engineering, Fu Jen Catholic University,
Taipei, Taiwan 242, R.O.C

ABSTRACT

In this paper, we study the blind channel estimation and multiuser detection for quasi-synchronous MC-CDMA MIMO system with space-time block codes (STBC). Considering the Alamouti's STBC scheme that involves two transmit antennas and multiple receive antennas, a subspace-based blind channel estimation for the STBC MC-CDMA system is proposed. Based on the first order perturbation theory, the mean-square error (MSE) of the channel estimation is derived. The computational cost is reduced to half via the weight analysis. Besides, both the forward backward averaging and the eigenspace techniques are applied to enhance the performance of multiuser detection. Finally, numerical simulations are given to evaluate and compare the proposed channel estimation and symbol detection techniques.

I. INTRODUCTION

The multi-carrier code-division multiple access (MC-CDMA) system combining the orthogonal frequency division multiplexing (OFDM) and CDMA, has been widely studied for future high-speed wireless communications. It is known that MC-CDMA provides bandwidth efficiency and interference suppression capability [1]. For a high data rate transmission system

---

*Corresponding author. Tel: +886-2-29052102 Fax: +886-2-29042638
E-mail: yujl@ee.fju.edu.tw

operating in frequency selective fading channel, the intersymbol interference (ISI) occurs and causes severe degradation in bit-error rate (BER) performance due to multipath propagation. To efficiently avoid the ISI effect, a cyclic prefix of length longer than the delay spread of channel impulse response is used in the OFDM system [2]. Besides, the inverse Fast Fourier transformation (IFFT) and Fast Fourier transformation (FFT) operations in the transmitter/receiver convert a frequency-selective fading channel into a number of narrowband flat-fading channels. Recently, the space-time processing technique which combines the multiple-input multiple-output (MIMO) system with coding scheme is proposed to mitigate the multipath fading effects. For example, Alamouti [3] proposed the space-time block code (STBC) scheme which equips two antennas with space-time coding at the transmitter and intelligent signal processing at the receiver; Kafle and Sesay [4] presented iterative semi-blind multiuser receivers for STBC MC-CDMA uplink system, and Jeong and Nakagawa [5] demonstrated the space-time coded MC-CDMA systems gain a significant profit of transmit diversity in multipath fading channel.

In this paper, we study the blind channel estimation and multiuser detection of STBC MC-CDMA MIMO systems. The subspace-based channel estimation has been successfully developed for different CDMA systems [6]. By singular value decomposition (SVD) on the data matrix, the noise subspace can be obtained. Then the channel impulse response is estimated by a quadratic optimization problem. We analyze the system performance by applying the first order perturbation theory to the SVD. After obtaining the channel impulse response, the multiuser detection is developed afterwards. The weight vectors of linearly constrained minimum variance (LCMV) filters for the consecutive symbols in one STBC block are first shown to be related each other. Thus the computational cost is reduced to half. Further, both the forward-backward averaging and the eigenspace techniques are utilized to improve the detection ability of the LCMV filter.

II. SIGNAL MODEL

Fig.1 shows an uplink quasi-synchronous space-time coded MC-CDMA MIMO system equipped with two transmit antennas and Q receive antennas. Without causing any power or bandwidth loss, we employ the Alamouti's space-time block coding (STBC) scheme. For each user k, two consecutive symbols are transmitted during two symbol intervals across transmit antennas. According to STBC scheme, we have $d^{(\mathrm{k})}(2n) = \mathrm{s}^{(\mathrm{k})}(2n)$, $d^{(\mathrm{k})}(2n+1) = -s^{(k)*}(2n+1)$, $\bar{d}^{(k)}(2n) = s^{(k)}(2n+1)$, $\bar{d}^{(k)}(2n+1) = s^{(k)*}(2n)$. In addition, periodic spreading codes $\{c^{(k)}, \bar{c}^{(k)}\}$ are used to spread the symbols $\{d^{(k)}(n), \bar{d}^{(k)}(n)\}$ in the transmit antennas 1 and 2, respectively. Then the transmitted signals of the k-th user are given by

$$x^{(k)}(n) = \frac{1}{N} d^{(k)}(n) \mathrm{F}^H c_1^{(k)}, \ \bar{x}^{(k)}(n) = \frac{1}{N} \bar{d}^{(k)}(n) \mathrm{F}^H c_2^{(k)} \tag{1}$$

where $c_1^{(k)} = [c_0^{(k)} \ldots c_{N-1}^{(k)}]^T$ and $c_2^{(k)} = [\bar{c}_0^{(k)} \ldots \bar{c}_{N-1}^{(k)}]^T$ are spreading codes, and denotes the DFT matrix. In order to combat the ISI and eliminate the asynchronism between different users and delay spread of channel, a sufficient cyclic prefix is appended upon each symbol. We further assume that the channels are linear time-invariant (LTI) where $h_{iq}^{(k)} = [h_{iq}^{(k)}(0) \ldots h_{iq}^{(k)}(M-1)]^T$, $i \in \{1, 2\}, q \in \{1, \ldots, Q\}$, is the channel impulse response from the i-th transmit antenna to the q-th receiver antenna for the k-th user. Then the received signal at the q-th receive antenna after discarding the corresponding cyclic prefix is given by

$$r_q(n) = \sum_{k=1}^{K} x^{(k)}(n) \otimes h_{1q}^{(k)} + \bar{x}^{(k)}(n) \otimes h_{2q}^{(k)} + \eta_q(n) \tag{2}$$

where $\eta_q(n)$ is the AWGN with zero mean and variance σ_n^2 and $\otimes$ is the circular convolution. After performing the DFT operation on $r_q(n)$, the frequency-domain received signal vector is obtained by

$$y_q(n) = \sum_{k=1}^{K} d^{(k)}(n) \, C_1^{(k)} g_{1q}^{(k)} + \bar{d}^{(k)}(n) \, C_2^{(k)} g_{2q}^{(k)} + \eta_q(n) \tag{3}$$

where , $C_i^{(k)} = diag(C_i^{(k)})$, $g_{iq}^{(k)} = \mathrm{F}_M h_{iq}^{(k)}$, for $i=1,2$, $\tilde{\eta}_q(n) = \mathrm{F} \eta_q(n)$ and F_M contains the first M columns of F. The signal model in one STBC block at the q-th receive antenna is given by

$$z_q(n) = \begin{bmatrix} y_q(2n) \\ y_q^*(2n+1) \end{bmatrix} = \sum_{K}^{k=1} s^{(k)}(2n) \, a_{1q}^{(k)} + s^{(k)}(2n+1) \, a_{2q}^{(k)} = v_q(n) \tag{4}$$

where $a_{1q}^{(k)} = \begin{bmatrix} C_1^{(k)} & g_{1q}^{(k)} \\ C_2^{(k)} & g_{2q}^{(k)*} \end{bmatrix}$, $a_{2q}^{(k)} = \begin{bmatrix} C_2^{(k)} & g_{2q}^{(k)} \\ -C_1^{(k)} & g_{1q}^{(k)*} \end{bmatrix}$ and $v_q(n) = \begin{bmatrix} \tilde{\eta}_q(2n) \\ \tilde{\eta}_q^*(2n+1) \end{bmatrix}$. By stacking all $z_q(n), q = 1 \ldots Q$, the received space-time codeword is expressed as

$$z(n) = [Z_1^T(n) \ldots Z_Q^T(n)]^T = \mathrm{As}(n) + v(n) \tag{5}$$

where $a_i^{(k)} = [a_{i1}^{(k)T} \ldots a_{iQ}^{(k)T}]^T$, i=1,2 , $v(n) = [v_i^T(n) \ldots v_Q^T(n)]$, $A = [a_1^{(1)} a_2^{(1)} \ldots a_1^{(k)} a_2^{(k)}]$ and $s(n) = [s^{(1)}(2n) s^{(1)}(2n+1) \ldots s^{(K)}(2n) s^{(K)}(2n+1)]^T$.

III. BLIND SUBSPACE CHANNEL ESTIMATION

In this section, we present the subspace-based blind channel estimation method for space-time coded MC-CDMA MIMO system. By stacking successive received space-time codewords, we construct a data matrix

$$Z = [z(n) \ldots z(n+J-1)] = AS + V \tag{6}$$

where $S = [s(n) \ldots s(n+J-1)]$ is the transmitted signal block matrix from all users. Considering the noise free case and applying the singular value decomposition (SVD) on the data matrix *Z*, we have

$$Z = [U_s \;\; U_n] \begin{bmatrix} A_s & 0 \\ 0 & 0 \end{bmatrix} [V_s \;\; V_n]^H \tag{7}$$

where the vectors in U_s associated with nonzero singular values in the diagonal matrix A_s span the signal subspace same as that spanned by the columns of A, and the vectors in U_n associated with zero singular values span the noise subspace. Since the signal subspace and noise subspace are orthogonal, the columns of A are orthogonal to noise subspace. With $A = [\ldots a_1^{(k)} a_2^{(k)} \ldots]$, we have that

$$U_n^H a_i^{(k)} = 0, \; i = 1, 2 \tag{8}$$

We further simplify $a_i^{(k)}$, $i = 1$, 2 by

$$a_1^{(k)}=\begin{bmatrix} C_1^{(k)} & g_{11}^{(k)} \\ C_2^{(k)} & g_{21}^{(k)*} \\ \vdots & \\ C_1^{(k)} & g_{1Q}^{(k)} \\ C_2^{(k)} & g_{2Q}^{(k)*} \end{bmatrix}=D_1^{(k)}g^{(k)},\ a_2^{(k)}=\begin{bmatrix} C_2^{(k)} & g_{21}^{(k)} \\ C_1^{(k)} & g_{11}^{(k)*} \\ \vdots & \\ C_2^{(k)} & g_{2Q}^{(k)} \\ C_1^{(k)} & g_{1Q}^{(k)*} \end{bmatrix}=D_2^{(k)}g^{(k)*} \tag{9}$$

where $D_i^{(k)}=I_Q\otimes D_i^{(k)}=0$, $i=1,2$, and

$$D_1^{(k)}=\begin{bmatrix} C_1^{(k)} & 0 \\ 0 & C_2^{(k)} \end{bmatrix},\ D_2^{(k)}=\begin{bmatrix} 0 & C_1^{(k)} \\ -C_1^{(k)} & 0 \end{bmatrix} \tag{10}$$

$$g^{(k)}=[g_{11}^{(k)T}\, g_{21}^{(k)H} \ldots g_{1Q}^{(k)T}\, g_{2Q}^{(k)H}]^T \tag{11}$$

Using $g_{iq}^{(k)}=F_M h_{iq}^{(k)}$, (11) becomes

$$g^{(k)}=(I_{2Q}\otimes F_M)\, h_{iq}^{(k)} \tag{12}$$

where $h^{(k)}=[h_{11}^{(k)T}\, h_{21}^{(k)H} \ldots h_{1Q}^{(k)T}\, h_{2Q}^{(k)H}]^T$. Substituting (10) and (12) into (8) yields

$$\begin{cases} U_n^H D_1^{(k)}(I_{2Q}\otimes F_M)h^{(k)}=0 \\ U_n^T D_2^{(k)*}(I_{2Q}\otimes F_M)h^{(k)}=0 \end{cases} \tag{13}$$

(13) is a linear system of $2(QN-K)$ equations in $2QM$ unknowns. It is overdetermined if $QN-K>QM$ and consequently has unique nontrivial solution. However, in the presence of noise, (13) will be not satisfied due to the perturbation of noise subspace. The estimation algorithm can be modified to cope with the presence of noise V in (6) by the following optimization problem,

$$\hat{h}^{(k)}=\arg\min_{\|h\|=1}\|Q_c^H h^{(k)}\|^2=\arg\min_{\|h\|=1} h^{(k)H}\ (Q_c Q_c^H)h^{(k)} \tag{14}$$

where $\begin{bmatrix} U_n^H D_1^{(k)}(I_{2Q}\otimes F_M) \\ U_n^T D_2^{(k)*}(I_{2Q}\otimes F_M) \end{bmatrix}$. Then the estimate of $h^{(k)}$ up to an unknown scalar is the normalized eigenvector corresponding to the smallest eigenvalue of $Q_c Q_c^H$. The inherent scalar ambiguity problem in blind channel estimation can be solved by using pilot sequences [7]. The MSE analysis of channel estimation is derived by the first order perturbation theory of subspace in [11], which is given by

$$E[\,\Delta h^{(k)^H}\,\Delta h^{(k)}\,]=\frac{\sigma_n^2}{J\sigma_k^2}tr\,(Q_c^{+H}\,Q_c^{+})=\frac{\sigma_n^2}{J\sigma_k^2}\,\|Q_c^{+}\|_F^2 \tag{15}$$

where $\sigma_k^2=[\,|\,s^{(k)}(n)\,|^2]$, "+" is the pseudo-inverse of a matrix.

IV. Multiuser detection

Once the estimation of $h^{(k)}$ is derived, we can construct $a_1^{(k)}$ and $a_2^{(k)}$ from (9) and (12). Then the transmitted symbols can be detected by the linearly constrained minimum variance (LCMV) filter [7]

$$w_k^{(k)}=\frac{1}{a_i^{(k)}R^{-1}a_i^{(k)}}R^{-1}a_i^{(k)}\,,\ i=1,2 \tag{16}$$

where $R=E[z(n)\,z^H(n)]$. The symbol detection is performed thereafter. For BPSK signal scheme, for example, the decisions are evaluated by

$$\hat{s}^{(k)}(2n)=sign[Re(W_1^{(k)^H}z(n))] \tag{17}$$

$$\hat{s}^{(k)}(2n+1)=sign[Re(W_2^{(k)^H}z(n))] \tag{18}$$

However, the weight vector of LCMV filter is sensitive to finite sample and signature vector errors. In the following, the efficient methods are proposed to reduce the complexity and enhance the system performance.

A. Weight analysis

The correlation matrix is obtained from (5)

$$R=\sum_{K}^{k=1}\sigma_k^2 a_1^{(k)} a_1^{(k)H}+\sigma_k^2 a_2^{(k)} a_2^{(k)H}+\sigma_n^2 I_{2NQ} \tag{19}$$

To proceed, we discuss the relation of $a_1^{(k)}$ and $a_2^{(k)}$. It is found from (10) that $D_1^{(k)}=M_{2N}^H D_2^{(k)}$, $D_2^{(k)}=-M_{2N}^H D_1^{(k)}$ and

$$D_1^{(k)}=M_{2NQ}^H D_2^{(k)},\ D_2^{(k)}=-M_{2NQ}^H D_1^{(k)} \tag{20}$$

where $M_{2N}=\begin{bmatrix}0 & I_N\\ -I_N & 0\end{bmatrix}$, $M_{2NQ}=I_Q\otimes M_{2N}$ and M_{2NQ} is a unitary matrix, i.e., $M_{2NQ}M_{2NQ}^H=M_{2NQ}M_{2NQ}=I_{2NQ}$. Substituting (20) into (9), we have

$$a_1^{(k)}=M_{2NQ}^H a_2^{(k)*},\ a_2^{(k)}=-M_{2NQ}^H a_1^{(k)*} \tag{21}$$

Using (21), we have from (19) that

$$R^*=M_{2NQ}^H R M_{2NQ} \tag{22}$$

where $-M_{2NQ}=M_{2NQ}^T=M_{2NQ}^H$ has been applied in (22). Substituting (21)-(22) into (16), we obtain

$$w_2^{(k)}=M_{2NQ}w_1^{(k)*} \tag{23}$$

The analysis result in (23) shows that weight vector $w_2^{(k)}$ can be computed directly from $w_1^{(k)}$. Therefore, the computational cost will be reduced to half.

B. FORWARD-BACKWARD AVERAGING TECHNIQUE

The weight vector $w_1^{(k)}$, which can be used to detect both the space-time coded symbols $s^{(k)}(2n)$ and $s^{(k)}(2n+1)$, is very sensitive to finite samples and signature vector errors. To reduce the finite sample effect, one can use the forward-backward averaging technique [9] to increase the effective samples. Practically, the ensemble correlation matrix R is not available and a sample correlation matrix $\hat{R}$ is used instead. If J samples are available, $\hat{R}$ is computed by

$$\hat{R} = \frac{1}{J}\sum_{n=1}^{J} z(n)z^{H}(n) \tag{24}$$

Further, we define the backward signal vector and the backward sample correlation matrix respectively by

$$z_b(n) = M_{2NQ}z^{*}(n) \tag{25}$$

$$\hat{R}_b = \frac{1}{J}\sum_{n=1}^{J} z_b(n)z_b^{H}(n) = M_{2NQ}\hat{R}^{*}M_{2NQ}^{H} \tag{26}$$

We call $z_b(n)$ as backward signal vector because the order of $z(n)$ is rearranged in (25). It is observed from (22) and (26) that $\hat{R}_b$ is equal to R when J approaches infinite. Then the forward-backward sample correlation matrix is defined by

$$\hat{R} = \frac{1}{2}(\hat{R} + \hat{R}_b) = \frac{1}{2J}\sum_{n=1}^{J}(z(n)z^{H}(n) + z_b(n)z_b^{H}(n)) \tag{27}$$

$\tilde{R}$ can be treated as a sample correlation matrix with $2J$ samples. $\hat{R}_b$ can be derived from $\hat{R}$ at the cost of permutations and complex conjugate operations only. Moreover, the computation of $\tilde{R}$ in (27) requires negligibly extra $4N^2Q^2$ additions over the computation of $\hat{R}$ which requires $4JN^2Q^2$ multiplications and $4(J-1)N^2Q^2$ additions. Consequently, the performance of the detectors in (17) and (18) will be improved by substituting (27) instead of (24) into (16) with a slight increase of computational load.

C. EIGENSPACE TECHNIQUE

We can also adopt the eigenspace-based filter to alleviate the performance degradation due to signature vector errors and/or finite sample effects. Ideally, the weight vectors of LCMV filter in (16) fall onto the signal subspace. Nevertheless, it will deviate from the signal subspace because of signature vector errors and/or finite sample effects. It is shown from [10] that the eigenspace-based receiver computes weight vectors by projecting the weight vectors of LCMV filter onto the signal subspace, which are given by

$$w_{2s}^{(k)} = \widehat{U}_s\,\widehat{U}_s^{H}\,\widehat{w}_1^{(k)}, \quad w_{2s}^{(k)} = \widehat{U}_s\,\widehat{U}_s^{H}\,\widehat{w}_2^{(k)} \tag{28}$$

where $\widehat{U}_s$ is the signal subspace corrupted by the white Gaussian noise, $\widehat{w}_i^{(k)}$, i =1,2 are the weight vectors of LCMV filter if signature vector errors and/or finite sample effects occur. One can see that $w_{1s}^{(k)}$ and $w_{2s}^{(k)}$ are closer to the ideal weight vectors in (16) than $\widehat{w}_i^{(k)}$, i =1,2. Therefore, the weight vectors of eigenspace filter will produce a lower BER than those of LCMV filter. It is noted that in practical situation, the signal subspace $\widetilde{U}_s$ computed from SVD of (6) is used instead of U_s. Further, the backward signal vectors in (25) can be appended into (6) to increase the number of samples. Therefore, the accuracy of the signal subspace is improved and the system performance is then enhanced.

V. COMPUTER SIMULATIONS

Consider a five-user space-time coded MC-CDMA MIMO systems with two transmit antennas and two receive antenna. The transmit symbol is adopted the BPSK modulation scheme, and unit-energy spreading codes of length N =32 is used. The channel impulse response is modeled by finite impulse response (FIR) with i.i.d. complex Gaussian of zero-mean and variance $1/M$. The curve for forward-backward samples indicates the estimation result by appending backward signal vector $z_b(n)$ of (25) into data matrix of (6). Fig.2 and Fig. 3 show the root-mean-square error (RMSE) versus the input signal-to-noise ratio (SNR) and the number of block, respectively. One can find that the analysis result and simulation result are matched very well. Besides, the RMSE of channel estimation is reduced due to the use of backward signal vectors. Fig.4 and Fig. 5 show the output SINR and the bit-error-rate (BER) versus input SNR, respectively. To verify the correctness of the weight analysis, the simulation results by using (23) are also presented. The performance of the optimum receiver is calculated by using the weight vectors in (16) where ensemble correlation matrix and true signature vectors are applied. It is shown that the output SINR of the filters with the forward-backward averaging technique and/or the eigenspace technique are closer to the optimum value than the LCMV filter. Besides, the simulation results by using (16) or (23) are matched very well. This validates the weight analysis even in the finite sample scenario. Fig.6 and Fig. 7 show the output SINR and the BER versus the data block, respectively. It is observed that those proposed methods converge faster to the optimum SINR and have lower BER than the LCMV filter. Finally, the effects of the number of receive antennas are discussed in Fig.8 and Fig. 9, providing multiple antennas are available at the receiver. It is observed that unlike the LCMV filter, those proposed filters gain the benefit of receiver diversity. We have shown in [10] that under a perturbed signature vector and/or finite sample scenario, the performance of LCMV filter will be degraded as the number of antennas increases. Since the signature vector $a_i^{(k)}$ is perturbed due to the estimation error in $h^{(k)}$ and R is corrupted by the finite sample effect, the performance of the Capon receiver might be degraded while increasing the number of receive antennas. On the other hand, the eigenspace technique, which is used to alleviate the effects of finite samples and signature vector errors, has a higher output SINR and lower BER.

VI. CONCLUSION

The MC-CDMA systems with Alamouti's space-time block codes are studied in this paper. The signal model for uplink quasi-synchronous ST-coded MC-CDMA system is first derived. A novel blind channel estimation is proposed and the MSE of channel estimation is analyzed. We further examine the enhancement methods for multiuser detection. Both the forward-backward averaging technique and eigenspace technique are used to improve the detection ability. The weighting analysis is also presented to save about half of the computational cost. Compute simulation demonstrate the correctness of the channel estimation and superiority of the multiuser detection. This work can be extended to the MC-CDMA systems with more than two transmit antennas. It is especially worthy to study whether the proposed results will be applicable to the STBC with four transmit antennas.

References

(1) S. Hara and R. Prasad, "Design and performance of multicarrier CDMA system in frequency-selective Rayleigh fading channels," *IEEE Trans. Veh. Techno.*, vol. 48, pp. 1584-1595, Sept. 1999.

(2) Z. Wang and G. B. Giannakis, "Wireless multicarrier communications: Where Fourier meets Shannon," *IEEE Signal Processing Mag.*, vol. 17, no. 3, pp. 29-48, May 2000.

(3) S. M. Alamouti, "A simple transmit diversity techniques for wireless communications," *IEEE J. Select. Areas Commun.*, vol. 16, pp.1451-1458, Oct. 1998.

(4) P.L. Kafle, and A.B. Sesay, "Iterative semi-blind multiuser Receivers for a Space-Time Block-Coded MC-CDMA Uplink System" *IEEE Trans. Veh. Techno*. Vol. 53 , pp.601 - 610, May. 2004

(5) I. Jeong and M. Nakagawa, "Performance of broadband MC-CDMA systems with transmit diversity," *IEICE Trans. Commun.*, vol. E85-B no. 10, pp 1937-1943, Oct. 2002

(6) E. Aktas and U. Mitra, "Complexity reduction in subspace-based blind channel identification for DS/CDMA systems," *IEEE Transaction on Communications*, Vol.-48, No.8, pp. 1392-1404, Aug. 2000.

(7) H. Li, X. Lu, and G. B. Giannakis, "Capon Multiuser Receiver for CDMA Systems With Space-Time Coding," *IEEE Transactions on Signal Processing*, vol. 50, No. 5, pp. 1193-1204, May 2002.

(8) Z. Xu, "On the second-order statistics of the weighted sample covariance matrix," *IEEE Transaction on Signal Processing*, Vol.-51, No.2, pp.527-534, Feb. 2003.

(9) H. L. Van Trees, *Optimum array processing, Part IV of detection, estimation, and modulation theory*, John Wiley & Sons, Inc., New Tork, 2002.

(10) J.L. Yu and C.C. Yeh, "Generalized eigenspace-based beamformers," *IEEE Transaction on Signal Processing*, Vol.SP-43, No.11, pp.2453-2461, Nov. 1995.

(11) Jung-Lang Yu, Chih-Chan Lin and Ming-Feng Lee, "MC-CDMA Multiple-Input Multiple-Output Systems with Space-Time Block Codes", *IEEE 2005 International Symposium on Microwave, Antenna Propagation and EMC Technologies for Wireless Communications*, Beijing, China, pp. 1487-1490, Aug. 2005.

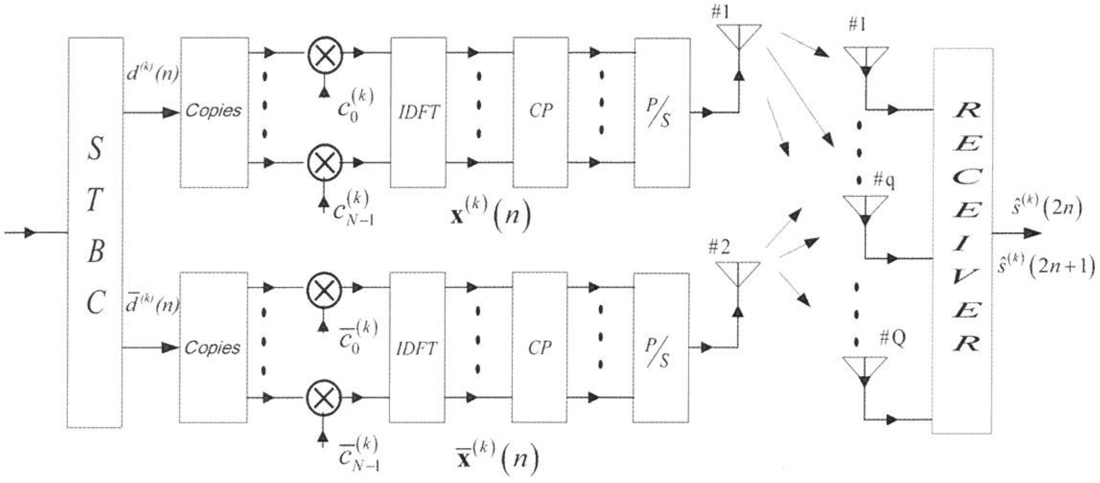

Fig.1. Space-Time Coded MC-CDMA MIMO system equipped with two transmits antennas and Q receiver. antennas.

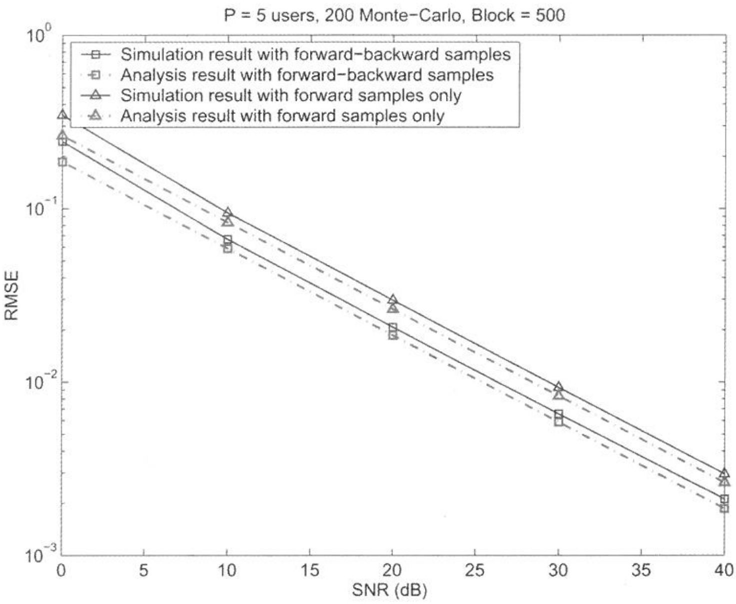

Fig.2. Performance of channel estimation versus input SNR when block size = 500 and Monte-Carlo trials = 200

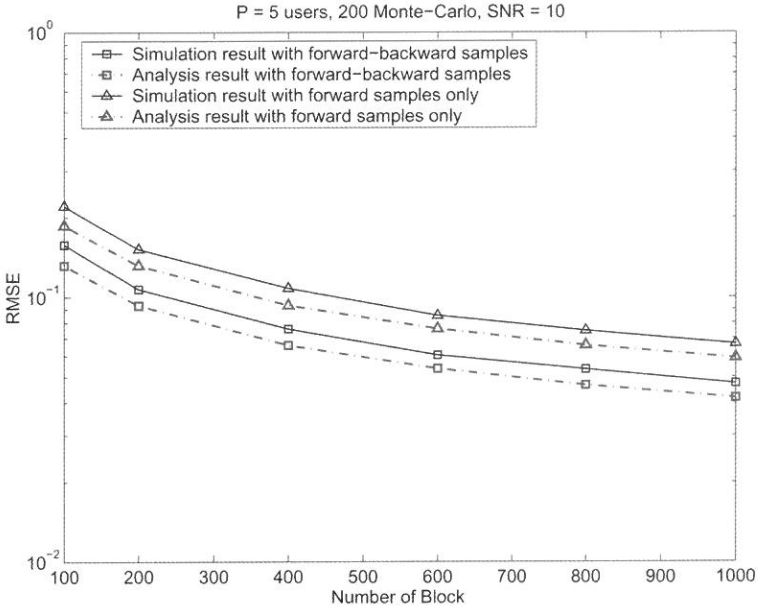

Fig.3. Performance of channel estimation versus number of block when input SNR = 10dB and Monte-Carlo trials = 200

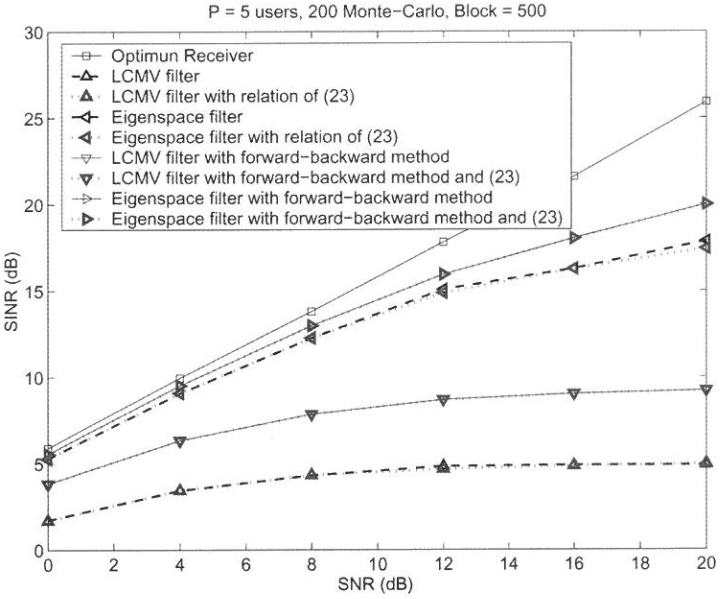

Fig.4. Output SINR versus input SNR for the compared methods.

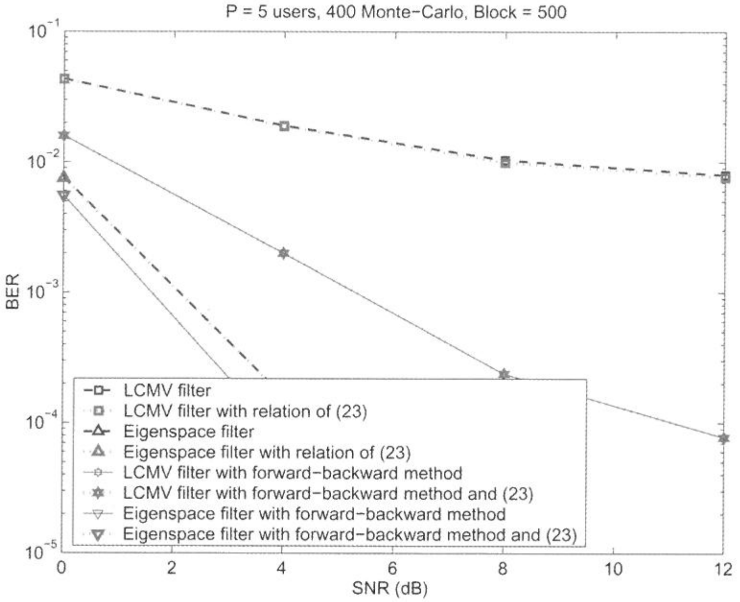

Fig.5. BER versus input SNR for the compared methods.

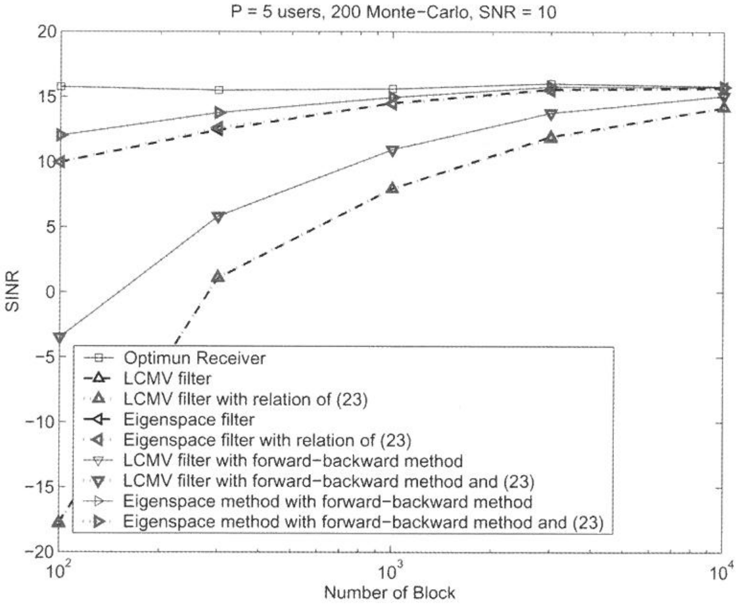

Fig.6. Output SINR versus the block number for the compared methods.

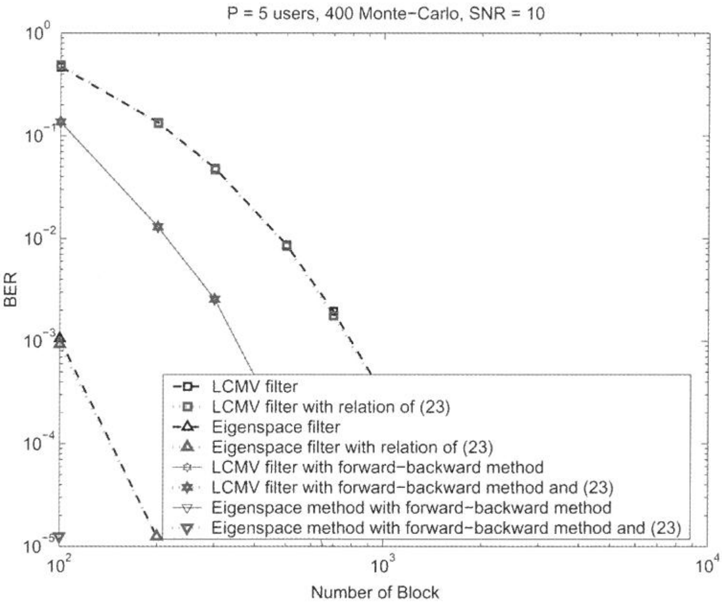

Fig.7. BER versus the block number for the compared methods.

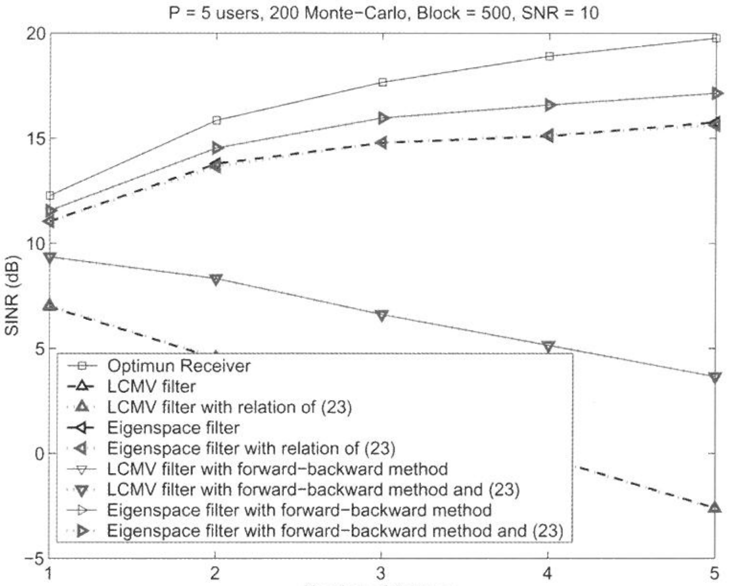

Fig.8. Output SINR versus the number of receive antennas for the compared methods.

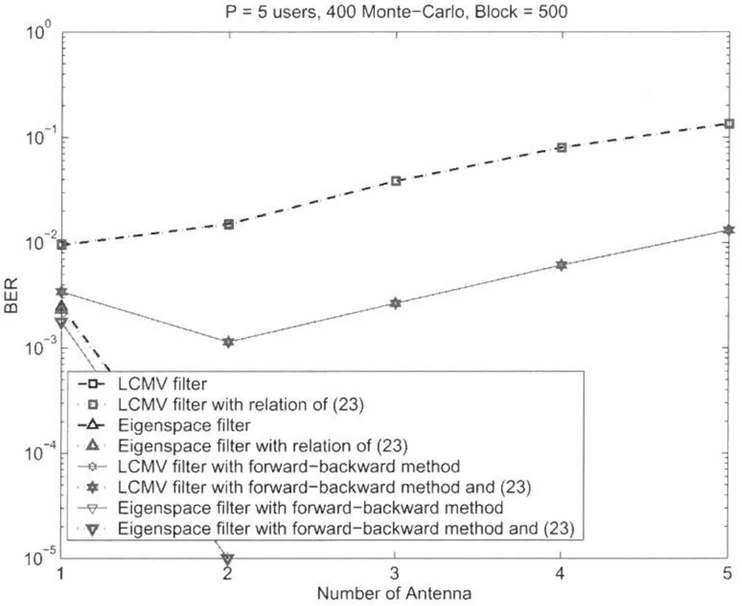

Fig.9. BER versus the number of receive antennas for the compared methods.

received October 28, 2005
revised November 24, 2005
accepted December 20, 2005

空時碼多載波分碼多工存取系統之研究

余金郎　林致群

輔仁大學電子工程學系

中文摘要

本論文中，我們將探討在準同步下之空時碼(STBC)多載波分碼多工存取(MC-CDMA)多輸入多輸出(MIMO)系統之盲目通道估測及多使用者偵測技術。我們採用 Alamouti 之兩傳多收的空時碼系統，提出一個基於子空間技術的盲目通道估計。利用第一階擾動理論，我們分析得到通道估計的均方錯誤(MSE)值。透過權重分析，計算的複雜度可以降低到一半。此外，我們應用前後向平均技術和特徵空間技術來提升多使用者偵測的性能。 最後，計算機模擬結果顯示我們提出的通道估計和訊符偵測技術的優異。

創新密鋪平面圖案系統之研究

呂克明

亞洲大學資訊工程學系
台中縣霧峰鄉柳豐路 500 號

摘　　要

先有發明後有創新。發明是新工具或新方法的發現，創新是新工具或新方法的應用。只要發明還沒有得到實際上的應用，那麼對經濟就不會發生任何貢獻。

密鋪平面圖案的發明，早在 1976 年，英國數學家羅傑．彭羅斯就向美國專利商標局申請。自從彭羅斯瓷磚系統專利開了先河以來，密鋪平面非週期性瓷磚系統在全世界澎湃地發展，到今天相繼有 217 位向美國專利局申請獲得專利，還有 162 個專利的申請在等待通過。這些專利圖案的應用，涵蓋很廣，舉凡先前舖地、牆面被覆、玩具和遊戲的應用，到影像處理、通訊技術、生物資訊、地理資訊、積體電路設計、數位相機等等不勝枚舉的應用。如此可見密鋪平面圖案的發明，不但有實際上的應用，而且有接連不斷的創新。

本研究將從密鋪平面的基礎開始，經過美國專利商標局的網站密鋪平面圖案的蒐尋與資料探勘。首先介紹多邊形密鋪平面，然後說明具有創新的週期性密鋪平面瓷磚系統內的拿破崙瓷磚系統，最後討論目前最熱門非週期性的彭羅斯瓷磚系統、僧帽系統與混雜式瓷磚系統。

關鍵詞：密鋪平面、正多邊形、半正多邊形、黃金分割、拿破崙瓷磚系統、彭羅斯瓷磚系統、僧帽系統、混雜式瓷磚系統

---

*Corresponding author. Tel: +886-4-23323456　ext.6100
E-mail: klu@asia.edu.tw

一、前　言

美籍奧地利經濟學家熊彼得[2]於 1934 年出版的《經濟發展理論》[3]書中認爲:先有發明後有創新。發明是新工具或新方法的發現，創新是新工具或新方法的應用。只要發明還沒有得到實際上的應用，那麼對經濟就不會發生任何貢獻。

密舖平面圖案的發明，早在 1976 年，英國數學家羅傑·彭羅斯[4]就向美國專利商標局[5]申請。自從彭羅斯瓷磚系統專利開了先河以來，密舖平面（plane tessellation）非週期性瓷磚系統（non-periodic tiling）在全世界澎湃地發展，到今天[6]相繼有 217 位向美國專利局申請獲得專利，還有 162 個專利的申請在等待通過。這些專利圖案的應用，涵蓋很廣，舉凡先前舖地、牆面被覆、玩具和遊戲的應用，到影像處理、通訊技術、生物資訊、地理資訊、積體電路設計、數位相機等等不勝枚舉的應用[7]。如此可見密舖平面圖案的發明，不但有實際上的應用，而且有接連不斷的創新。

（一）密舖平面

英文字「tessellation」這個字是從動詞「tessellate」而來的。查閱字典[8]可以知道「tessellate」的意思是用以形成或安排不規則或是馬賽克（mosaic）鑲嵌圖案中的小正方形。追溯它的來源是希臘字愛奧尼亞語（Ionic）的「tesseres」，即英文的數目字四。因此我們可以想像最初的地磚應該是正方形。

密舖平面（plane tessellation）的定義是利用一種或多種圖形，按規律不斷在平面上

---

[2] 約瑟夫˙ 熊彼得(Schumpeter J. A.)，何畏等譯，1990 年《經濟發展理論（The Theory of Economic Development）》，北京:商務印書館，頁 98。

[3] Schumpeter J. A, 1934, Theory of economic development: An inquiry into profits, capital, credit, interest and the business cycle. USA: Harvard University Press.

[4] 羅傑·彭羅斯(Roger Penrose, 1931-)，英國數學家。

[5] 美國專利商標局，網站是 http://www.uspto.gov/。

[6] 以密舖(tessellation)與圖案(patterns)在美國專利局網站 http://www.uspto.gov/做蒐尋，可以得到 217 個專利。其中，最新的專利是 6948661 號。它是由澳大利亞籍基亞西˙ 佛布魯克（Kia Silverbrook）和瓦姆斯雷˙ 羅伯特（Walmsley Simon Robert）以《物件表面之加碼資料結構系統（Data structure encoded on a surface of an object）》在 2005 年 9 月 27 日獲得。

[7] 就目前的 217 個專利，研究其應用所得的結果。

[8] Steven Schwartzman's The Words of Mathematics, 1994, The Mathematical Association of America.

拼砌，直至表面完全被覆蓋，不留任何空隙，也沒有任何重疊部分，稱爲「密鋪平面」。（Seymour and Britton, 1989; Britton and Britton, 1992）

（二）圖案與對稱

一個自然或是藝術圖案均有三個特性:一個單位、重複性與組織系統。系統是一種基礎組織的自然或文化的原則。分析對稱，可以讓我們了解圖案的組織，並且提供決定不變與修改的方法。

改變圖案可預期的對稱關係或是其他可預期與重複的圖案就可以將圖案轉換成偉大的藝術品。出人意外地，對稱性常常依賴非對稱性。非對稱性，是缺少對稱與對稱的基本特性。我們可以藉對稱分析的結果來辨識「基本區域（fundamental region）」，它是用來解釋重複性有可能形成圖案的最小單元。

（三）基本對稱

在地毯的世界裡，有平移（translation）、反射（reflection）、滑行反射（glide reflection）和旋轉（rotation）等四種基本對稱[9]。（如圖一）

平移-沿著直線做重複穩定的移動　反射-翻過直線做重複穩定的動作

滑行反射-沿著直線重複穩定的反射動作　旋轉-環著點重複穩定的翻轉動作

圖一　四種基本對稱

---

[9] Symmetry & Pattern: The Art of Oriental Carpets, Organized by The Textile Museum（2320 S Street NW, Washington, DC 20008）

（四）邊界圖案

在地毯的世界裡，有邊界圖案（border pattern）和畫面圖案（field pattern）兩大類。邊界圖案有平移（translation）、水平反射（horizontal reflection）、垂直反射（vertical reflection）、反射 + 反射（reflection + reflection）、滑行反射（glide reflection）、旋轉（rotation）和反射 + 滑行反射（reflection + glide reflection）等七種圖案。（如圖二）

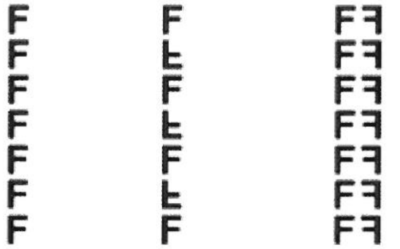

平移　水平反射　垂直反射

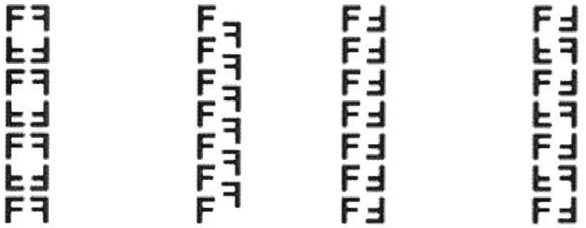

反射 + 反射　滑行反射　旋轉　反射 + 滑行反射

圖二　七種邊界圖案

（五）畫面圖案

畫面圖案（field pattern），有平移（translations）、反射（reflections）、反射 + 反

射（reflections + reflections）、滑行反射（glide reflections）、反射 + 滑行反射（reflections + glide reflections）、旋轉(2)（rotations (2)）、反射 + 旋轉(2)（reflections + rotations (2)）、旋轉(2)+ 滑行反射（rotations (2) + glide reflections）、旋轉 (2) + 反射 + 反射（rotations (2) + reflections + reflections）、旋轉 (4)（rotations (4)）、反射 + 旋轉 (4)（reflections + rotations (4)）、旋轉 (4) + 反射（rotations (4) + reflections）、旋轉 (3)（rotations (3)）、反射+旋轉(3)（reflections + rotations (3)）、旋轉 (3) + 反射（rotations (3) + reflections）、旋轉 (6)（rotations (6)）和反射 + 旋轉 (6)（reflections + rotations (6)）等十七種。其中括弧內的數字代表圖形小組的數目。（如圖三）但是嚴格地說，地毯的十七種畫面圖案，有反射 + 滑行反射、反射 + 旋轉 (4)、旋轉 (4) + 反射、旋轉 (3)、反射+旋轉(3)、旋轉 (3) + 反射、旋轉 (6)、反射 + 旋轉 (6)等八種是有空隙的，不能合乎密舖的定義，所以應該祇有九種密舖平面的圖案。


平移


反射

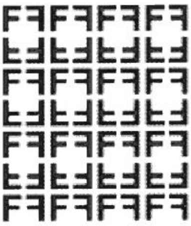
反射 + 反射


滑行反射

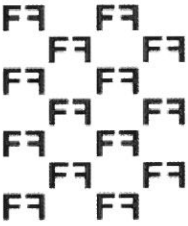
反射 + 滑行反射

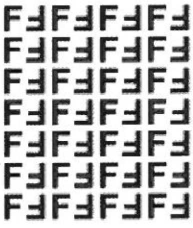
旋轉 **(2)**

反射 + 旋轉 (2) 旋轉 (2)+滑行反射 旋轉(2) + 反射 + 反射

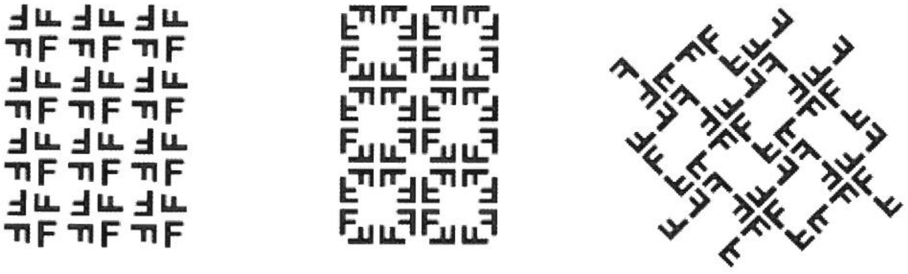

旋轉 (4) 反射 + 旋轉 (4) 旋轉 (4) + 反射

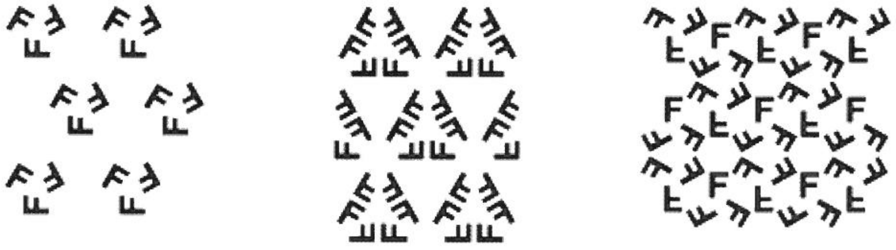

旋轉 (3) 反射+旋轉(3) 旋轉 (3) + 反射

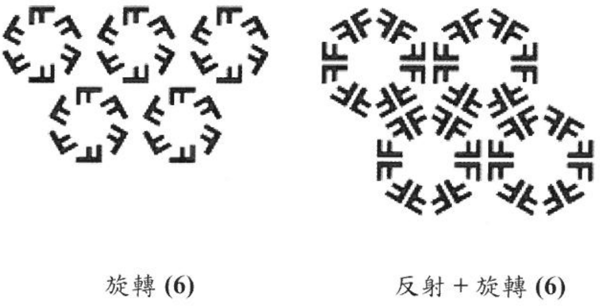

旋轉 (6) 反射 + 旋轉 (6)

圖三 十七種畫面圖案

二、多邊形密鋪平面

（一）對稱密鋪（regular tessellation）

在正多邊形中，只有正三角形、正方形和正六邊形（參考圖四）能夠密鋪平面[10]。因爲正三角形的每隻內角等於 60°，六個正三角形拼在一起時，在公共頂點上的六個角之和剛好等於 360°，所以重複鋪貼正三角形就能夠密鋪平面。同理，正方形及正六邊形的每隻內角分別等於 90°和 120°，所以四個正方形或三個正六邊形拼在一起時，在公共頂點的四角或三角之和也剛好等於 360°，所以重複鋪貼時也能密鋪平面。

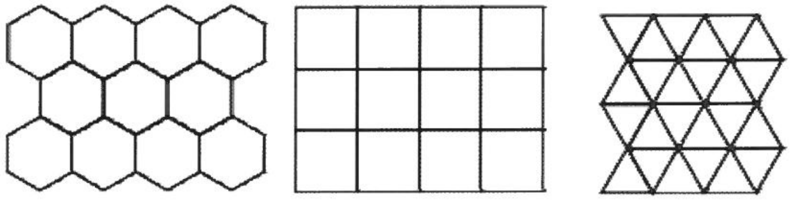

{6,3} {4,4} {3,6}

圖四　正三角形、正方形和正六邊形密鋪平面

其實，任意的三角形和任意的四邊形都可以密鋪平面。另外，我們知道正五邊形不可以密鋪平面，但原來有些非正五邊形是可以密鋪平面的，有些則不行。至於有多少種非正式五邊形可以密鋪平面，到現在仍然是一個未解之謎。

除了用正多邊形或非正多邊形來密鋪平面外，也可以用一些有趣的圖案來密鋪平面。箇中奧妙就是懂得應用旋轉（rotation），平移（translation）和反射（reflection）的原理。

（二）密鋪平面

密鋪平面是由兩個或較多的凸形正式多面形所組成。圖案是由圍繞多面形每個頂點的相同多面形稱半正式密鋪圖案或稱阿幾米德密鋪圖案（Archimedean tessellations）。

---

[10] Eric W. Weisstein. "Tessellation." From MathWorld--A Wolfram Web Resource. http://mathworld.wolfram.com/Tessellation.html

一共有八種這樣的密舖平面圖案。如圖五的阿幾米德密舖圖案（Ghyka 1977, pp. 76-78; Williams 1979, pp. 37-41; Steinhaus 1999, pp. 78-82; Wells 1991, pp. 226-227）

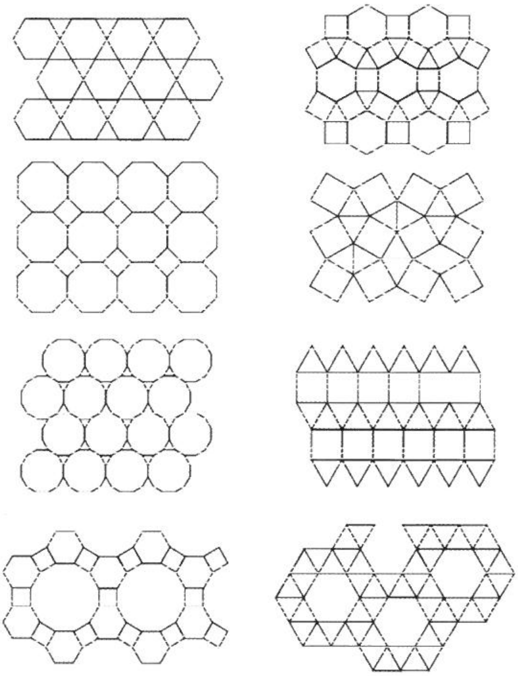

圖五　阿幾米德密舖圖案

三、週期性密舖平面瓷磚系統

週期性密舖平面的定義：在平面上，平移一小區塊的圖案而無反射和旋轉。[11]

（一）拿破崙定理與密舖平面

拿破崙密舖平面瓷磚系統是由拿破崙定理（Napoleon's Theorem）[12] 推演出來的密

---

[11] http://scientium.com/drmatrix/puzzles/progchal.htm/

[12] Napoleon's Theorem 在數學上是經常被一再討論的話題，這個定理最早且明確的定義是在 1825 年由一位盧瑟福(Dr. W. Rutherford)寫於 《The Ladies Diary 》 一書中, 但是盧瑟福可能不是第一個發現者, 因爲似乎沒有直接的證據說明盧瑟福和 Napoleon Bonaparte 有什麼關聯。

舖平面圖案，所建構成的瓷磚系統。傑姆羅伊(Jim Loy)[13] 於 2003 年爲拿破崙定理下了定義：在任意三角形的每一個邊畫一個等邊三角形。然後連接這三個等邊三角形的中心，形成另外一個等邊三角形。這個等邊三角形就是外拿破崙三角形（outer Napoleon triangle）。同時我們也可以證明內拿破崙三角形（inner Napoleon triangle）。請參考圖六的外拿破崙三角形與內拿破崙三角形。值得一提的是，外拿破崙三角形的面積減去內拿破崙三角形等於原來三角形的面積。

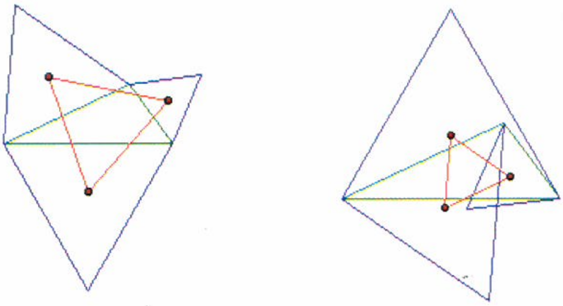

圖六　外拿破崙三角形與內拿破崙三角形

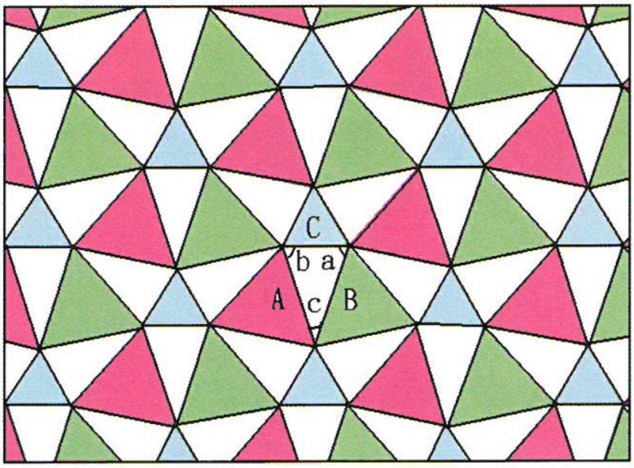

圖七　拿破崙密舖平面 [14]

---

[13] 傑姆羅伊(Jim Loy)的網站 http://www.jimloy.com/geometry/napoleon.htm

[14] http://www.mathpages.com/home/kmath270/kmath270.htm

拿破崙密鋪平面是由一個任意三角形和三個分別使用其中的一個邊做成的等邊三角形建構成的。請參考圖七拿破崙密鋪平面。我們可以發現，這個任意三角形（其三個邊分別是A、B、C，其對應的角分別是a、b、c）與其中的一個邊做成的等邊三角形連接在一起形成一個四邊形，因爲有三邊，所以會有三個四邊形的圖案。三個四邊形圖案組的四個邊和四個內角（其中有一個內角是 60°），分別是四邊形 AABC（60°、c+60°、a、b+60°）、四邊形 BBCA（60°、a+60°、b、c+60°）、四邊形 CCAB（60°、b+60°、c、a+60°）。這三組四邊形圖案組，可以創建一個新的「相等對角與對邊等長的六邊形」。這創新六邊形的六個邊與內角，分別是 ABCABC（a+60°、b+60°、c+60°、a+60°、b+60°、c+60°）。

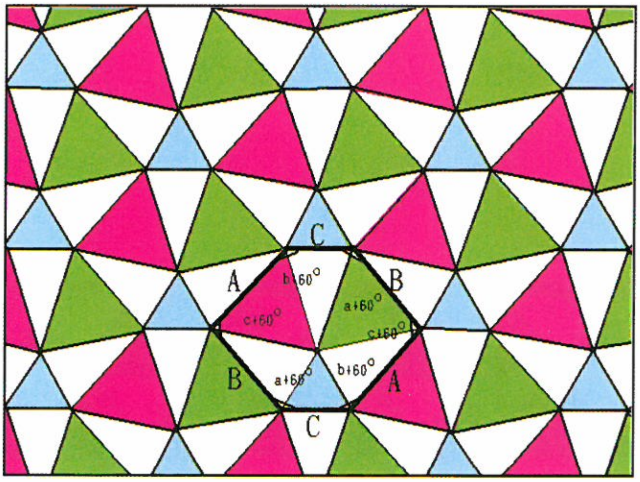

圖八 相等對角與對邊等長的六邊形

（二）「相等對角與對邊等長六邊形」是可以密鋪的

假如 a+60°、b+60°、c+60°均爲銳角，也就是 ABCABC 是爲凸狀六邊形。根據雷因哈特（K. Reinhardt）1918 年在法蘭克福大學獲得博士的論文發現，凸狀六邊形僅有三種可以是密鋪平面。三個凸狀六邊形其中的一個條件：相鄰三個角的和是 a+60°+b+60°+c+60°=360 和邊長 A 的對邊 D，邊長也是 A。因此我們可以證明一個「相等對角與對邊等長凸狀六邊形」是可以密鋪平面的。(Gardner 1988)

假如a+60°、b+60°、c+60°其中之一角爲鈍角，也就是ABCABC是爲凹狀六邊形，則不能使用雷因哈特定理證明。但是我們可以使用「對角線中點旋轉」的原理來證明。因爲「相等對角與對邊等長六邊形」的任何對角線所分割的兩個四邊形，即是沿著「對角線中點旋轉」的影子，所以它是密鋪平面的。總之，不論是凹狀或是凸狀，任何「相等對角與對邊等長的六邊形」是可以密鋪的。

（三）黃金分割與拿破崙密鋪平面瓷磚系統

黃金分割與密鋪平面圖案很有關係。當討論到等腰三角形，我們會談到由黃金分割[15]爲比例的建構成的兩個等腰三角形。假如我們將黃金分割的長段和短段分別稱 L 和 S。這樣的話，就形成了LLS和SSL兩個等腰三角形了。經過簡單的計算，我們可以得到：等腰三角形 LLS 的三邊邊長比例和內角分別是（1：1：0.618）、（72°、72°、36°）；而另外一個等腰三角形 SSL 的三邊邊長比例和內角分別是（1：1：1.618）、（36°、36°、108°）。[16]這兩個等腰三角形的夾角分別是 36°的 1 倍與 3 倍。

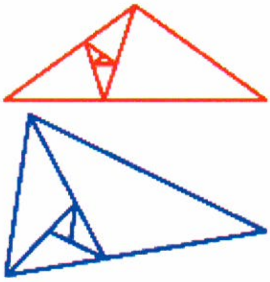

圖九　**SSL** 與 **LLS** 等腰三角形

同時，我們加入夾角分別是 36°的 2 倍（即 72°）與 4 倍（即 144°）的兩個等腰三角形，我們就有一整套夾角是 36°的 1、2、3、4 倍的四個等腰三角形。再經過簡單的計算，可以得到 2 倍與 4 倍夾角 36°的兩個等腰三角形的三邊邊長比例和內角分別是

---

[15] 在羅馬的奧古斯都時代，有個名爲維特魯維亞（Marcus Vitruvius Pollio）的名建築師制定了「黃金分割律」，指出：一個平面若能分爲和諧並且具有美感的幾塊面積，則其中最小塊與最大塊的比例應當等於最大塊與整個面積的比例。

[16] John Sharp, "Spirals and the Golden Section", Nexus Network Journal, vol. 4, no. 1 (Winter 2002), http://www.nexusjournal.com/Sharp_v4n1-intro.html

（1：1：0.851）、（54°、54°、72°）和（1：1：0.526）、（18°、18°、144°）。我們現在藉著這四個等腰三角形的其中之一與正三角形連接，建構成三組四邊形圖案組，然後建構一個「相等對角與對邊等長的六邊形」。對於另外三個等腰三角形，我們也可以如法炮製，最後建構成三個「相等對角與對邊等長的六邊形」：令 B=C，上述（一）的三個四邊形組，分別成爲筆尖（pen head）四邊形 AABB（60°、b+60°、a、b+60°）、左影（left shadow）四邊形 BBBA（60°、a+60°、b、b+60°）、右影（right shadow）四邊形BBAB（60°、b+60°、b、a+60°）。因此，夾角是36°的1、2、3、4倍的四個等腰三角形，會分別產生三個四邊形圖案組，分述如下。

1）夾角36°等腰三角形建構成的筆尖、左影、右影三個四邊形圖案組- a=36°，b=c=72°；筆尖四邊形邊長比例（0.618：0.618：1：1）[17] 和內角（60°、132°、36°、132°）、左影四邊形邊長比例（1：1：1：0.618）和內角（60°、96°、72°、132°）、右影四邊形邊長比例（1：1：0.618：1）和內角（60°、132°、72°、96°）。

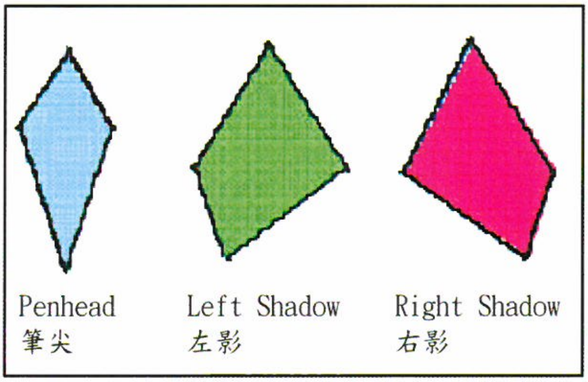

圖十　夾角**36°**等腰三角形建構成的筆尖、左影、右影三個四邊形圖案組

a）鼓形六邊形－當我們將以上三個四邊形圖案組的左影與右影分別與筆尖的同一邊的兩個邊結合，可以形成兩個「相等對角與對邊等長的六邊形」。我們稱它們爲鼓形（drum）。鼓形六邊形邊長比例（0.618：1：1：0.618：1：1）和內角（96°、132°、132°、96°、132°、132°）。

---

[17] 邊長=2x sin(18°)=0.618

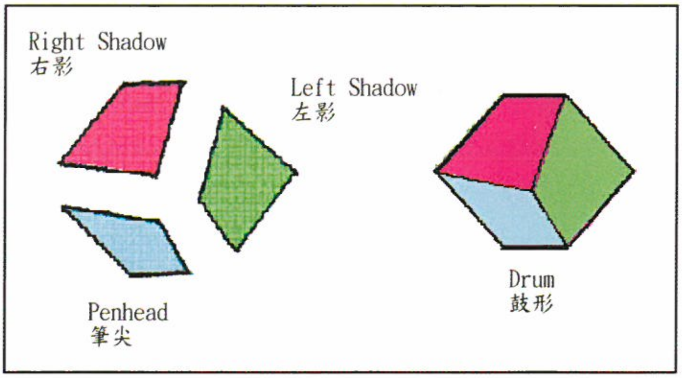

圖十一　夾角 **36°**等腰三角形的三個四邊形圖案組成的鼓形六邊形

b）鼓形六邊形密舖平面瓷磚－因為鼓形是一個「相等對角與對邊等長的六邊形」，根據第（三）節的推論，鼓形六邊形是可以密舖的。黃金分割比例與黃金分割角分別在鼓形六邊形的邊長與內角表現出來。首先是鼓形六邊形的邊長比例 0.618：1，它也可以改寫成 1：1.618。這是邊長為黃金分割比例的鼓形六邊形。我們稱它們為「黃金比例的鼓形六邊形」。至於鼓形六邊形的兩種內角 96°與 132°分別是 60°和 36°與 72°的和。

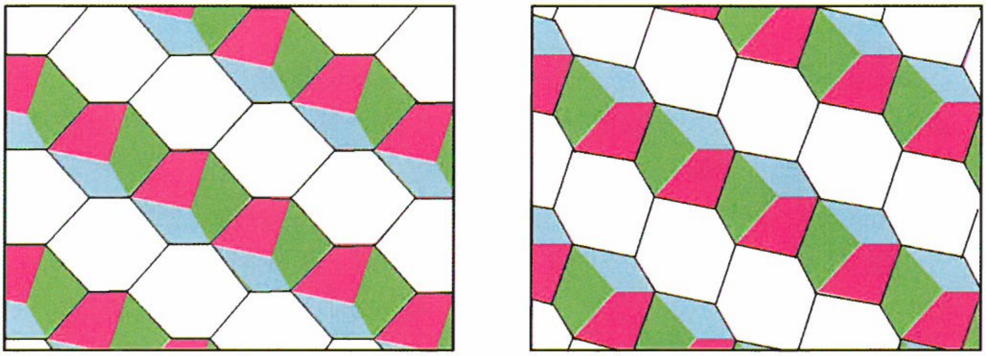

圖十二　夾角 **36°**等腰三角形建構成的鼓形與斜鼓形六邊形密舖平面

c）三葉形與雁形八邊形密舖平面瓷磚－假若我們以鼓形六邊形的筆尖為中心，左影

與右影「平移」與筆尖的對邊結合，可以形成兩個對稱的八邊形。我們分別稱它們爲三葉形（three leaves）與雁形（goose）。然後分別再次地將右影與左影「平移」與筆尖的對邊結合，均回歸到斜鼓形（skew drum）六邊形。我們稱這四次的「平移」所建構的關係圖爲「平移環（translation circle）」。

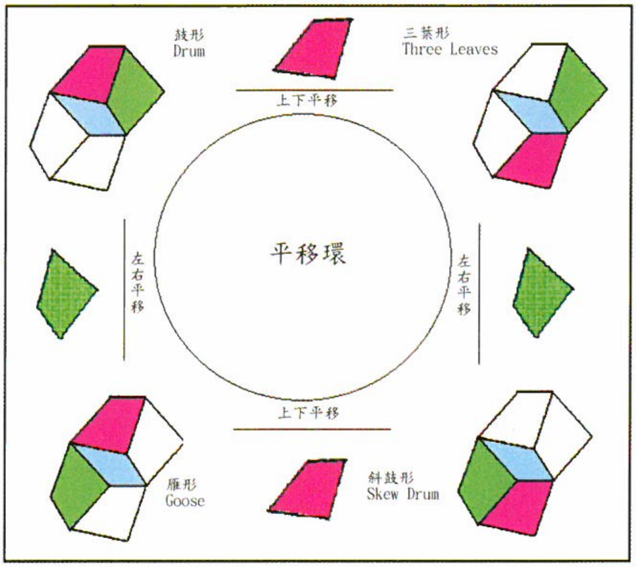

圖十三　夾角 **36°**等腰三角形建構成的平移環

d）三葉形與雁形八邊形密鋪平面瓷磚－有一個重要的觀念，這裡必須說明，因爲鼓形六邊形是密鋪平面，經過這個「平移」的動作，三葉形與雁形也是密鋪平面。三葉形八邊形密鋪平面瓷磚邊長比例（1：1：1：1：1：1：1：1）和內角（36°、264°、60°、96°、204°、96°、60°、264°）。雁形八邊形密鋪平面瓷磚邊長比例（0.618：1：0.618：1：0.618：1：0.618：1）和內角（60°、228°、72°、132°、156°、132°、72°、228°）。値得一提的是，三葉形八邊形與雁形八邊形的邊長與內角與黃金分割比例與黃金分割角有密切的關係。其中，等邊對稱的凹狀八邊形的三葉形的八個邊的邊長均等；其內角由黃金分割角帶頭，然後除了 60°，就是三種內角 264°、96°、204°，分別是 120°和 144°、60°和 36°、60°和 144°的和。像鼓形六邊形一樣，雁形八邊形的邊長是黃金分割比例 0.618：1，即 1：1.618，，我們亦稱呼它爲「黃金比例的雁形八邊形」；其內角由 60°帶頭，然後

除了黃金分割角 72°，就是三種內角 228°、132°、156°，分別是 120°和 36°+72°、60°和 72°、120°和 36°的和。

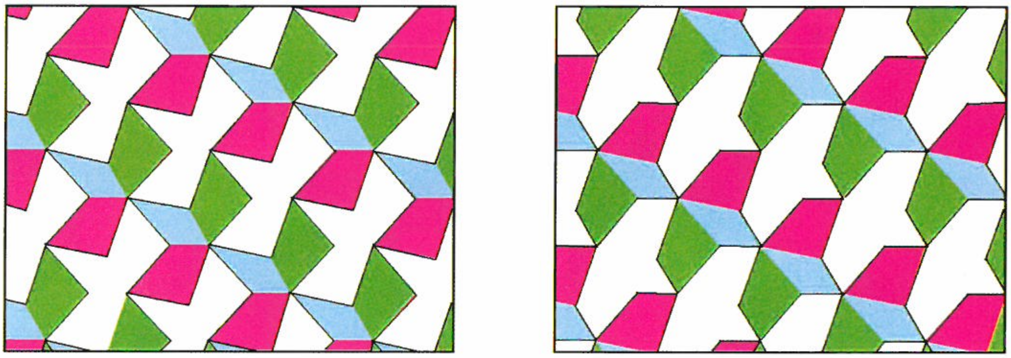

圖十四　夾角 **36°**等腰三角形建構成的三葉形與雁形八邊形密鋪平面

2）a=72°，b=c=54°；筆尖四邊形邊長比例（1.176：1.176：1：1）[18] 和內角（60°、114°、72°、114°）、左影四邊形邊長比例（1：1：1：1.176）和內角（60°、132°、54°、114°）、右影四邊形邊長比例（1：1：1.176：1）和內角（60°、114°、54°、132°）。夾角是兩倍黃金分割角的三個四邊形的邊長比例 1.176：1 和內角，在圖形分辨上會是一種尷尬的局面。首先是邊長比例 1.176：1，這個 1.176 和 1 的數值實在是太接近了。從筆尖四邊形的外形看起來簡直像個菱形。內角所含的黃金分割角 54°和 60°僅僅相差 6°，實在是太接近了，根本無法分辨。

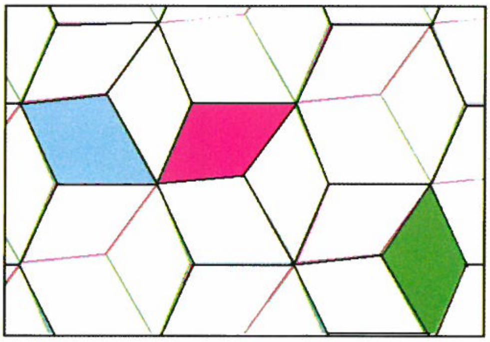

圖十五　夾角 **72°**等腰三角形建構成的筆尖、左影、右影三個四邊形圖案組

---

[18] 邊長=2x sin(36°)=1.176

a）鼓形六邊形密鋪平面瓷磚－當我們將以上三個四邊形圖案組的左影與右影分別與筆尖的同一邊的兩個邊結合，可以形成兩個「相等對角與對邊等長的六邊形」。鼓形六邊形密鋪平面瓷磚邊長比例（1.176：1：1：1.176：1：1）和內角（132°、114°、114°、132°、114°、114°）。

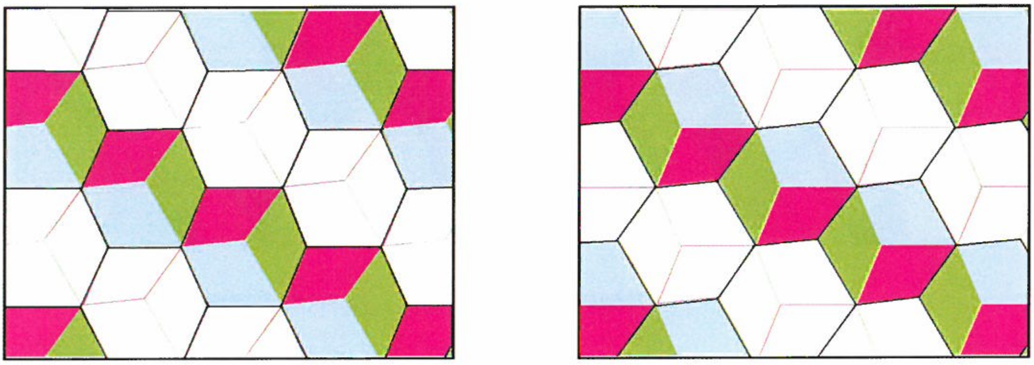

圖十六　夾角 **72°**等腰三角形建構成的鼓形與斜鼓形六邊形密鋪平面

b）三葉形與雁形八邊形密鋪平面瓷磚－假若我們以筆尖爲中心，左影與右影對稱地將長邊與筆尖的長邊結合，三個四邊形結合在一起，可以形成兩個「相等邊長對稱的八邊形」。三葉形八邊形密鋪平面瓷磚邊長比例（1：1：1：1：1：1：1：1）和內角（72°、228°、60°、132°、168°、132°、60°、228°）。雁形八邊形密鋪平面瓷磚邊長比例（1.176：1：1.176：1：1.176：1：1.176：1）和內角（60°、246°、54°、114°、192°、114°、54°、246°）。

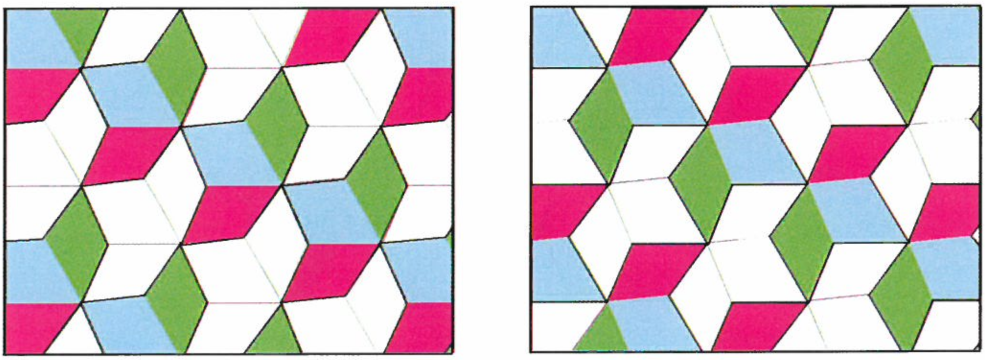

圖十七　夾角 **72°**等腰三角形建構成的三葉形與雁形八邊形密鋪平面

3）a=108°，b=c=36°；筆尖四邊形邊長比例（1.618：1.618：1：1）[19] 和內角（60°、96°、108°、96°）、左影四邊形邊長比例（1：1：1：1.618）和內角（60°、168°、36°、96°）、右影四邊形邊長比例（1：1：1.618：1）和內角（60°、96°、36°、168°）。六邊形密鋪平面瓷磚邊長比例（1.618：1：1：1.618：1：1）和內角（168°、96°、96°、168°、96°、96°）。

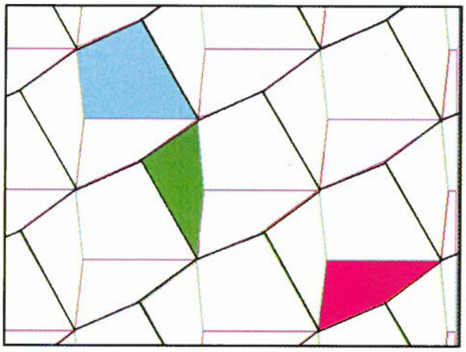

圖十八　夾角 **108°**等腰三角形建構成的筆尖、左影、右影三個四邊形圖案組

a）鼓形六邊形密鋪平面瓷磚－當我們將以上三個四邊形圖案組的左影與右影分別與筆尖的同一邊的兩個邊結合，可以形成兩個「相等對角與對邊等長的六邊形」。鼓形六邊形密鋪平面瓷磚邊長比例（1.618：1：1：1.618：1：1）和內角（168°、96°、96°、168°、96°、96°）。黃金分割比例與黃金分割角分別在鼓形六邊形的邊長與內角表現出來。首先是鼓形六邊形的邊長比例是 1：1.618。這是邊長爲黃金分割比例的鼓形六邊形。和夾角 36°等腰三角形建構成的鼓形六邊形一樣，我們亦稱呼它們爲「黃金比例的鼓形六邊形」。至於鼓形六邊形的內角 96°與 168°分別是 60°和 36°與 108°的和。

b）三葉形與雁形八邊形密鋪平面瓷磚－假若我們以筆尖爲中心，左影與右影對稱地將長邊與筆尖的長邊結合，三個四邊形結合在一起，可以形成兩個「相等邊長對稱的八邊形」。三葉形八邊形密鋪平面邊長比例（1：1：1：1：1：1：1：1）和內角（108°、192°、60°、168°、132°、168°、60°、192°）。雁形八邊形密鋪平

---

[19] 邊長=2x sin(54°)=1.618

面邊長比例（1.618：1：1.618：1：1.618：1：1.618：1）和內角（60°、264°、36°、96°、228°、96°、36°、264°）。黃金分割比例與黃金分割角分別在雁形八邊形的邊長與內角表現出來。首先是雁形八邊形的邊長比例是 1：1.618。這是邊長爲黃金分割比例的雁形八邊形。和鼓形六邊形一樣，我們亦稱呼它們爲「黃金比例的雁形八邊形」。至於雁形八邊形的內角 264°、96°與 228°分別是 120°和 144°、60°和 36°、120°和 108°的和。

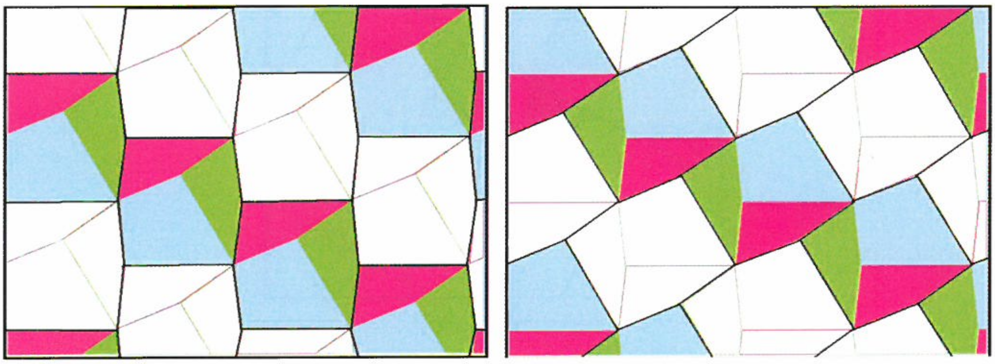

圖十九　夾角 **108°**等腰三角形建構成的鼓形與斜鼓形六邊形密舖平面

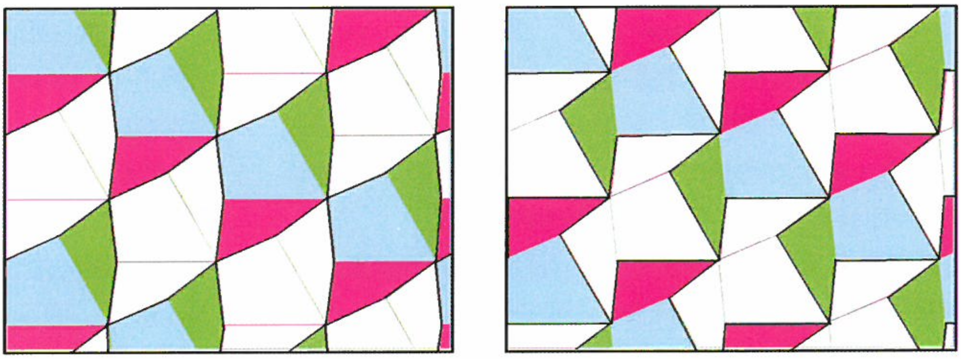

圖二十　夾角 **108°**等腰三角形建構成的三葉形與雁形八邊形密舖平面

4）a=144°，b=c=18°；筆尖四邊形邊長比例（1.902：1.902：1：1）[20] 和內角（60°、78°、144°、78°）、左影四邊形邊長比例（1：1：1：1.902）和內角（60°、204°、18°、78°）、右影四邊形邊長比例（1：1：1.902：1）和內角（60°、78°、18°、204°）。

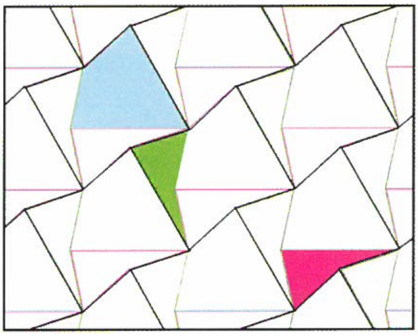

圖二十一　夾角 **144°**等腰三角形建構成的筆尖、左影、右影三個四邊形圖案組

a）鼓形六邊形密鋪平面瓷磚－當我們將以上三個四邊形圖案組的左影與右影分別與筆尖的同一邊的兩個邊結合，可以形成兩個「相等對角與對邊等長的六邊形」。鼓形六邊形密鋪平面瓷磚邊長比例（1.902：1：1：1.902：1：1）和內角（204°、78°、78°、204°、78°、78°）。由於有內角 204°超過 180°，因此稱呼它爲凹狀鼓形六邊形。

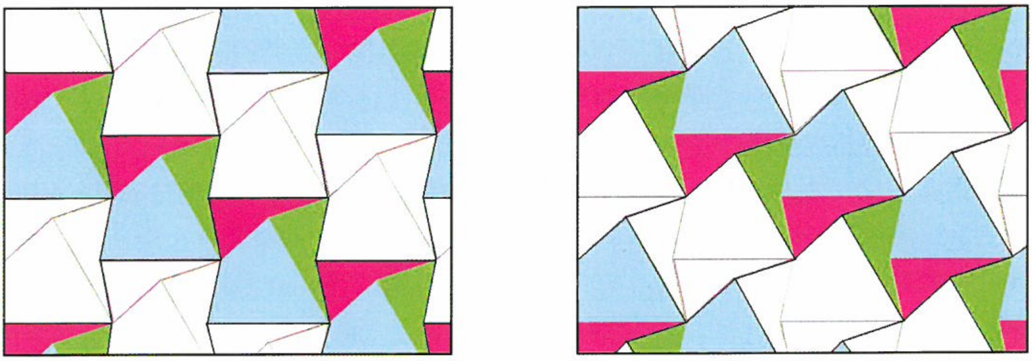

圖二十二　夾角 **144°**等腰三角形建構成的鼓形與斜鼓形六邊形

---

[20] 邊長=2x sin(72°)=1.902

b）三葉形與雁形八邊形密鋪平面瓷磚－假若我們以筆尖爲中心，左影與右影對稱地將長邊與筆尖的長邊結合，三個四邊形結合在一起，可以形成兩個「相等邊長對稱的八邊形」。三葉形八邊形 密鋪平面瓷磚邊長比例（1：1：1：1：1：1：1：1）和內角（144°、156°、60°、204°、96°、204°、60°、156°）。雁形八邊形密鋪平面瓷磚邊長比例（1.902：1：1.902：1：1.902：1：1.902：1）和內角（60°、282°、18°、78°、264°、78°、18°、282°）。

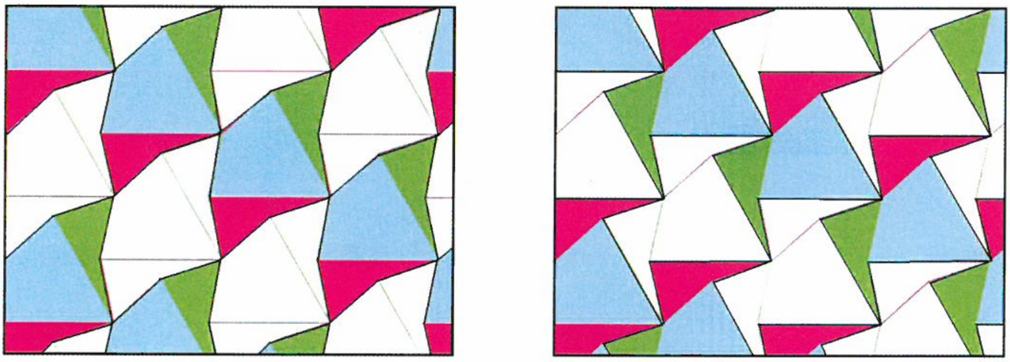

圖二十三　夾角 **144°**等腰三角形建構成的三葉形與雁形八邊形密鋪平面

（四）拿破崙密鋪平面瓷磚系統

經過以上的論述，我們可以知道依據拿破崙定理所做成的三組四邊形、六邊鼓形與八邊三葉形和雁形對稱圖形，是可以組成密鋪瓷磚圖案。我們假設任何等腰三角形夾角α，兩個等腰角β，底邊與腰身的邊長比例爲λ。可以計算出它們邊長與夾角，請參照表一。當然，假若夾角是與黃金分割有關的 36°、72°、108°、144°等四個角的等腰三角形的邊長與夾角，也可以參照表一。值得一提的是，當等腰三角形夾角α等於 60°的時候，三組四邊形全都成爲相同的筆尖圖形，六邊鼓形成爲正六邊形，八邊三葉形與雁形成爲一個相同的凹狀等邊八邊形。當等腰三角形夾角α大於 60°的時候，四邊形左影與右影的名稱則需要相互對調才能「名符其實」。同時八邊三葉形與雁形的名稱也需要相互對調。左影與右影、三葉形與雁形相互對調的現象，我們稱之爲「互調現象（mutual transposition）」。四邊形的左影與右影和八邊形的三葉形與雁形分別互稱爲「對偶圖案（dual pattern）」。

表一　夾角**α**等腰三角形建置成的六邊與八邊對稱拿破崙密鋪瓷磚圖形

夾角	筆尖 (pen head)	左影 (left shadow)	右影 (right shadow)	鼓形 (drum)	三葉形 (three leaves)	雁形 (goose)
α°	λ：λ：1：1 60°、β+60°、α、β+60°	1：1：1：λ 60°、α+60°、β、β+60°	1：1：λ：1 60°、β+60°、β、α+60°	λ：1：1：λ：1：1 α+60°、β+60°、β+60°、α+60°、β+60°、β+60°	1：1：1：1：1：1：1：1 α°、2β+120°、60°、α+60°、2β+60°、α+60°、60°、2β+120°	λ：1：λ：1：λ：1：λ：1 60°、α+β+120°、β°、β+60°、α+120°、β+60°、β°、α+β+120°
36°	0.618：0.618：1：1 60°、132°、36°、132°	1：1：1：0.618 60°、96°、72°、132°	1：1：0.618：1 60°、132°、72°、96°	0.618：1：1：0.618：1：1 96°、132°、132°、96°、132°、132°	1：1：1：1：1：1：1：1 36°、264°、60°、96°、204°、96°、60°、264°	0.618：1：0.618：1：0.618：1：0.618：1 60°、228°、72°、132°、156°、132°、72°、228°
72°	1.176：1.176：1：1 60°、114°、72°、114°	1：1：1：1.176 60°、132°、54°、114°	1：1：1.176：1 60°、114°、54°、132°	1.176：1：1：1.176：1：1 132°、114°、114°、132°、114°、114°	1：1：1：1：1：1：1：1 72°、228°、60°、132°、168°、132°、60°、228°	1.176：1：1.176：1：1.176：1：1.176：1 60°、246°、54°、114°、192°、114°、54°、246°
108°	1.618：1.618：1：1 60°、96°、108°、96°	1：1：1：1.618 60°、168°、36°、96°	1：1：1.618：1 60°、96°、36°、168°	1.618：1：1：1.618：1：1 168°、96°、96°、168°、96°、96°	1：1：1：1：1：1：1：1 108°、192°、60°、168°、132°、168°、60°、192°	1.618：1：1.618：1：1.618：1：1.618：1 60°、264°、36°、96°、228°、96°、36°、264°
144°	1.902：1.902：1：1 60°、78°、144°、78°	1：1：1：1.902 60°、204°、18°、78°	1：1：1.902：1 60°、78°、18°、204°	1.902：1：1：1.902：1：1 204°、78°、78°、204°、78°、78°	1：1：1：1：1：1：1：1 144°、156°、60°、204°、96°、204°、60°、156°	1.902：1：1.902：1：1.902：1：1.902：1 60°、282°、18°、78°、264°、78°、18°、282°
附註	β=（180°-α）/2 λ=2sin（α/2）					

四、非週期性密舖平面瓷磚系統

非週期性密舖平面的定義，是無法使用平移一小區塊的圖案週期地密舖平面。

（一）單一菱形的拼花地磚

菱形與三角形的關係。菱形是兩個等腰三角形所架構起來的。當這個等腰三角形的第三邊與第一、二邊相等時，就變成正三角形的特例。將兩個正三角形疊在一起就成了一個夾角 60°的菱形。請參考圖二十四的 60°的菱形環繞一個頂點的六個菱形的單一菱形拼花地磚。

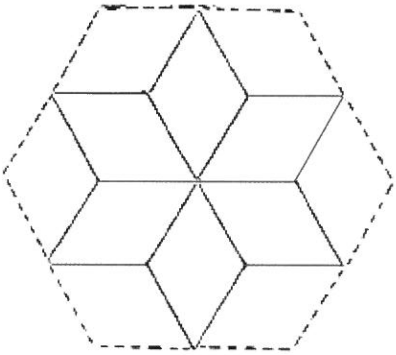

圖二十四　單一菱形的拼花地磚

（二）彭羅斯瓷磚系統

在等腰三角形當中，就數夾角是 72°的菱形與 36°的菱形兩個情況比較有名。彭羅斯瓷磚系統（Penrose tiling system），就是以這兩種菱形瓷磚爲基礎，透過一些複雜的組合填滿整個空間。這兩種菱形瓷磚，其中一個是胖的（fat）菱形，而另外一個是瘦的（thin）菱形。英國劍橋大學的數學物理學家，亦爲皇家學會的院士羅傑・彭羅斯[21]於 1976 年 6 月 24 日向美國專利局登記的第一個專利，美國專利 4133152 號。

---

[21] 余創豪，《彭羅斯對基督徒的啓迪 Y=a+bx+e log(odd)=P/(1-P)》，2005.8.29

值得一提的是，彭羅斯對數學、天文物理學、心理學、電腦學、哲學都有極大貢獻。在 1965 年至 1970 年期間，曾經與英國天文物理學家霍金斯[22]合作研究，証實了大爆炸奇異點的存在。1988 年二人分享了一個馳名國際的學術榮譽：胡夫獎[23]，1994 年他更被英國王室封爲「武士」[24]。對這個問題，寫了一本出乎他自己意料之外暢銷的書《皇帝新腦》[25]。每個彭羅斯瓷磚系統是一個較小的角是 72°的胖菱形或是一個較小的角是 36°的瘦菱形所組成的。請參閱圖二十五[26]。我們可以證明胖菱形與瘦菱形的面積比是黃金分割的比率[27]。二十五圖是使用史蒂夫・柯林斯（Stephen Collins）的鮑伯（Bob）程式所繪出的。

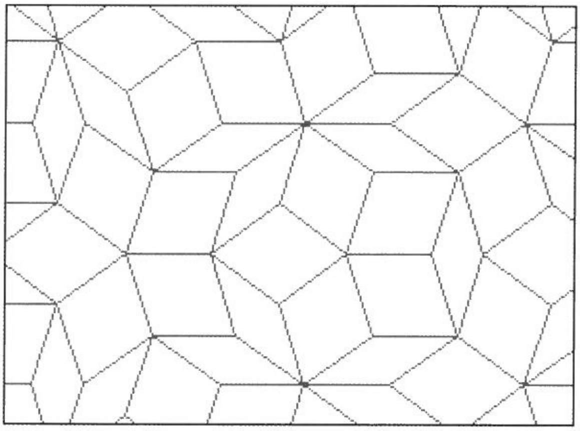

圖二十五　彭羅斯瓷磚系統

馬丁・肯柏[28]有一篇有關科學與文化的文章刊登在2005年7月5日《自然雜誌》題目是《瓷磚的技巧》[29]。主題是西澳大利亞大學伯斯分校分子與化學大樓的前廳的地板瓷磚[30]，就是使用當地出產的胖菱形與瘦菱形瓷磚所組成的一個非週期性彭羅斯瓷磚系統。

---

[22] Stephen William Hawking 出生於 1942 年 1 月 8 日英國牛津。

[23] 胡夫獎，Wolf Prize，是一個國際上有影響力的科學獎之一，由沃爾夫和其家族在 1976 年 1 月 1 日捐出 1000 萬美元成立。獎項旨在：「促進科學和藝術的發展以造福人類。」每年頒獎給化學、醫學、物理學、數學、農業和藝術方面有傑出成就者。

[24] 羅傑˙ 彭羅斯，因此被稱爲「瓷磚武士」（A Knight on the tiles）。

[25] 羅傑˙ 彭羅斯(Roger Penrose)著，《皇帝新腦》，台北：藝文印書館，1993；Roger Penrose 英文原著是《The Emperor's New Mind: Concerning Computers, Minds, and the Laws of Physics》, Oxford University Press, 1989.

[26] Tony Phillips, 《Penrose tiling Down Under》, Math in Media, August issue of year 2005, Stony Brook University, email tony at math.sunysb.edu.

[27] 黃金分割（Golden Section）的比率，是方程式X2-X-1=0的正値根，即（1+sqrt5）/2=1.61803 39887 49894 84820(又稱 Phi Number)。

這個並不是第一個發表的彭羅斯瓷磚系統。先前發表的有 1979 年在邁阿密大學學士大樓[31]的磨石子大廳地板、有 1993 年在卡爾頓學院[32]車輪圖案瓷磚系統、有 1997-98 年在樹城州立大學[33]計算機科學系費德曼副教授[34]浴室的瓷磚系統、還有 2003 年在北卡州梅瑞迪斯學院[35]科學與數學大樓的磨石子大廳地板。

伯斯分校的彭羅斯瓷磚系統與先前的彭羅斯瓷磚系統不同，主要在於使用兩個菱形圖案，而不是先前的風箏形（kite）與鏢形（dart）圖案，請參見圖二十六。這兩種不同的彭羅斯瓷磚系統，雖然數學的性質相同，但是在視覺的效果上確實不同。肯柏描述兩個菱形圖案的不同感受。

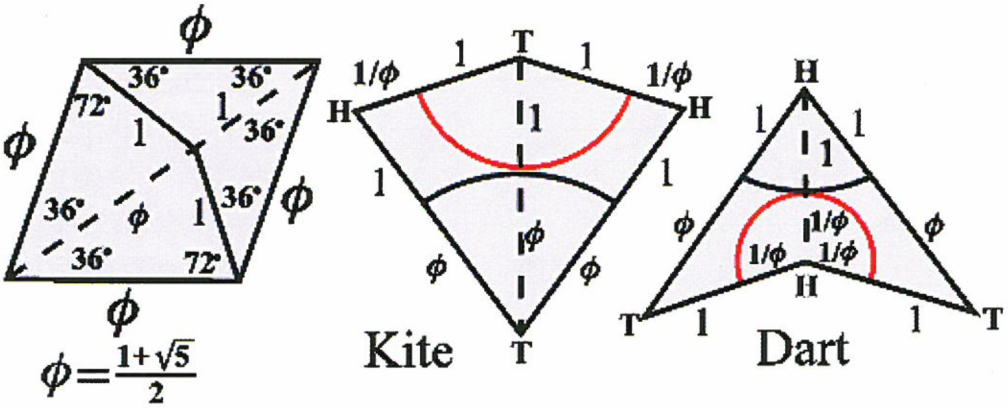

圖二十六　風箏形與鏢形圖案

---

[28] 馬丁・肯柏（Martin Kemp），英國牛津大學的教授，著有《萊奧納多˙達˙芬奇：人和自然的傑出作品》一書。（Kemp, 1981）

[29] Science in culture: A trick of the tiles. Summary: Penrose tiling is realized on a huge scale in Perth to give a perceptual feast for the eyes. (Kemp, 2005)

[30] Molecular and Chemical Sciences Building at the University of Western Australia in Perth.

[31] Bachelor Hall Miami University Oxford, OH 45056

[32] Carleton College One North College St. Northfield, MN 55057

[33] Boise State University, 1910 University Drive Boise, Idaho 83725-1145 USA

[34] Alex Feldman, Associate Professor, College of Engineering.

[35] Meredith College, Raleigh 27607-5298

（三）僧帽瓷磚系統（The Mitre System）[36]

現代鏡子迷宮大師阿德里安·費希爾（Adrian Fisher）和愛華德・泰勒・培格（Edward Taylor Pegg）以角錐（pyramid）、魚鰭（fin）、僧帽（mitre）等三種核心圖案組爲基礎，與軟木塞（cork）、扇形（fan）、鐘形（bell）與正方形等四種支援圖案組，透過一些複雜的組合填滿整個空間，建構成僧帽瓷磚系統（The Mitre System）。其中角錐圖案的邊長比值與內角分別爲（0.518：1：1：1）和（90°、60°、75°、135°）；魚鰭圖案的邊長比值與內角分別爲（1：1：1.366：0.355）和（90°、60°、120°、90°）；僧帽圖案的邊長比值與內角分別爲（1：0.518：1：0.518：1）和（60°、135°、105°、105°、135°）。請參考圖二十七的僧帽瓷磚系統。

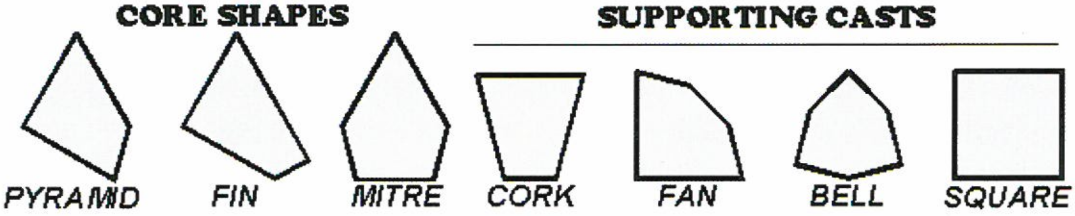

圖二十七　僧帽瓷磚系統的核心圖案組與支援圖案組[37]

（四）混雜式瓷磚（Chaos Tiles）系統[38]

阿德里安·費希爾和愛華德・泰勒・培格，以 18 邊形爲主，塡加上混雜式瓷磚組，建構成非週期性混雜式瓷磚系統。同時也可以配合 3、6、9 與 18 對稱軸線而建構成週期性密舖平面。混雜式瓷磚包括五邊形混雜式鸚鵡和混雜式房屋兩種圖案。它們的邊長比例和內角分別是（1：1：1：1：1）、（40°、200°、60°、100°、140°）和（1：1：

---

[36] Adrian Fisher 和 Edward Taylor Pegg, Jr. 於 2001 年 10 月 30 日共同獲得以《密舖平面組（Tessellation Sets）》爲題的 6309716 號專利。

[37] Adrian Fisher , Edward Taylor Pegg, Jr.和 Miroslav Vicher,《僧帽瓷磚系統（The Mitre System）》文章中提到《僧帽瓷磚核心圖案與支援圖案》，由阿德里安·費希爾（Adrian Fisher）和愛華德˙泰勒˙培格（Edward Taylor Pegg）正在向美國專利商標局申請中。

[38] 同註腳 37。

1：1：1）、（80°、160°、60°、100°、140°）。和僧帽瓷磚系統一樣，阿德里安·費希爾等，將應用的項目增加到公共水平舖地、室內水平舖地、公共垂直牆面被覆、室內垂直牆面被覆、拼花壁毯、印刷圖案、遊戲拼圖、平板遊戲、電腦遊戲、迷宮設計等等。

五、結果與討論

愛華德・泰勒・培格認爲彭羅斯瓷磚系統太過於簡單，而他的混雜式瓷磚系統複雜當中帶著規律性，看起來很是美麗，但是在邊緣切割時，和彭羅斯瓷磚系統一樣，都是地磚工人的夢魘。

和阿德里安·費希爾討論過後，針對密鋪平面圖案，培格訂定了九項《裝飾地磚規則（Rules of Decorative Bricks）》[39]。其內容如下：1）沒有一條直線橫過密鋪平面；2）能夠密舖成方形或是長方形；3）沒有銳角－有銳角的地磚太容易破碎；4）在模組平舖時，能夠規劃出最少的切割；5）遇到螺紋和其他的曲線的場合，儘可能使用不同顏色的地磚；6）瓷磚系統的圖案，能夠和其他瓷磚系統模組的介面配合性；7）較少的瓷磚系統圖案組件；8）可以同時建構週期性或是非週期性的圖案設計；9）圖案組件尺寸大小的一致性，例如十二邊形和三角形的圖案組件，對於承重地板來說是不可以的。

首先，我們對創新的「拿破崙密舖平面瓷磚系統」，依照九項《裝飾地磚規則》逐項分別討論。首先，筆尖、左影、右影三個四邊形組合成的鼓形六邊形和三葉形與雁形八邊形，分別與同樣的圖案，是相互交錯建構成的密舖平面。雖然是週期性的圖案，但是不會有一條直線橫過密舖平面的情況發生。其次，此系統的每個圖形的對邊都是平行的，很容易建構成方形或是長方形。其三，此系統每個四邊形組內均含有銳角，但是組合成鼓形六邊形和三葉形與雁形八邊形，其中鼓形六邊形的六個內角均大於 60°，成爲銳角的機會並不大，就算有也是接近於直角。三葉形與雁形八邊形的形狀優美，但是均有銳角，工人在貼磚的時候，要特別小心。第四項和第五項要求最少的切割和不同顏色的地磚這兩項，應該很容易完成。其六，此系統的筆尖、左影、右影三個四邊形組，均含有 60°角，和「僧帽瓷磚系統」內的核心圖案的角錐含有 60°角一樣，配合度高。其七，此系統僅有筆尖、左影、右影三個四邊形圖案組，比較「僧帽瓷磚系統」和「混雜式瓷磚」算是簡單的。其八，因爲此系統是週期性密舖平面，可能在地磚的顏色上做調

---

[39] 同註腳 38。

整，使得週期性密鋪平面看起來像是非週期性。最後，此系統的圖案組件邊長比例小於 2，尺寸大小一致，也是值得肯定的。至於「僧帽瓷磚系統」和「混雜式瓷磚」的討論，可見培格的論述，在此就不加以贅述。[40]

所謂的「亂中有序志在人心」，可專利的密鋪平面圖案的未來，無論是週期性或是非週期性的發展都是無可限量。本研究僅是拋磚引玉，希望有更多密鋪平面圖案的研究，在專利的驅動下，蓬勃發展。

六、誌謝與未來研究工作

首先，要感謝亞洲大學資訊與設計系主任陳榮銘副教授爲本文所作的潤飾與建議，同時還有亞洲大學資訊工程系林新力教授在英文摘要與翻譯，亞洲大學資訊工程系的白嘉祥、王子文和李嘉軒同學用心設計的 Java 程式與小畫家的圖案設計。本研究所描述的「密鋪平面系統」，已經於 2006 年 1 月 16 日向經濟部智慧財產局提出專利發明申請，案號第 095101616 號。未來的工作將繼續在黃金分割與其他可專利的密鋪平面圖案的方向發展。

七、參考文獻

(1) Britton, J. and Britton, W. Teaching Tessellating Art: Activities and Transparency Masters, Dale Seymour Publications, 1992

(2) Gardner, M. "Tilings with Convex Polygons." Ch. 13 in Time Travel and Other Mathematical Bewilderments. New York: W. H. Freeman, pp. 162-176, 1988.

(3) Ghyka, M., The Geometry of Art and Life. New York: Dover, 1977

(4) Kemp, Martin, Leonardo da Vinci: The Marvellous Works of Nature and Man, Dent,

(5) London, 1981

(6) Kemp, Martin, Science in culture: A trick of the tiles, Nature 436, 332-332 (21 Jul 2005)

(7) Kraitchik, M, "Mosaics.", §8.2 in Mathematical Recreations, New York: W. W. Norton, pp. 199-207, 1942

---

[40] 同註腳 38。

(8) Schott K (1981) Industrial Innovation in the United Kingdom, Canada and the United States, (British North American Committee: London)

(9) Seymour, Dale and Britton, Jill, Introduction to Tessellations, Palo Alto, CA: Dale Seymour Publications, 1989

(10) Sprecher, T. B. (1963)., A proposal for identifying the meaning of creativity,. In C. W. Taylor & F. Barron (Eds.), Scientific creativity: Its recognition and development. (pp. 77-88). New York: John Wiley & Sons

(11) Steinhaus, H. Mathematical Snapshots, 3rd ed. New York: Dover, pp. 75-76 and 78-82, 1999

(12) Wells, D., The Penguin Dictionary of Curious and Interesting Geometry, London: Penguin, pp. 121, 213, and 226-227, 1991

(13) Williams, R. The Geometrical Foundation of Natural Structure: A Source Book of Design. New York: Dover, pp. 35-43, 1979

received October 26, 2005
revised November 28, 2005
accepted December 21, 2005

A Study of Innovative Plane Tessellation Patterns Systems

Keh-Ming Lu
Department of computer science of information engineering
Asia University
Lioufong Rd500, Wufong Township, Taichung Conuty 413, Taiwan, R.O.C.

Abstract

Invention always comes first and innovation follows afterward. An invention is a discovery: an innovation is then the applications of invention to a product or service that is new to the market or simply new to the adopter (see Schott; 1981). If applications have not yet utilized, a great invention will have no contribution to our economy.

US Patent & Trademark Office (USPTO) awarded the first invention of plane tessellation to English mathematician Roger Penrose in 1976. Since then, the plane tessellation tiling systems have been mushrooming around the world. As today, there are 217 patents already awarded by USPTO and 162 applications are waiting for approval. The applications of these patents cover broadly from paving, wall-covering, toys, and games, to image processing, communication technologies, bioinformatics, geographical information systems, integrated circuit design, digital camera applications, etc. We may foresee the future of plane tessellation invention not only continuously show tangible applications but also render endless innovations.

This study starts with description of the basics of plane tessellation system and a web-based search and mining tasks through USPTO database. At first we introduced the regular polygons, then described our innovative periodical plane tessellation including Napoleon's tessellation tiling system, and lastly reviewed recent topics of Penrose tiling, Mitre, and Chaos tiles systems.

Key Words:plane tessellation, regular polygon, semi-regular polygon, golden section, Napoleon's tessellation tiling system, Penrose tiling system, Mitre system, Chaos tiles system